THE LINEAR TAPERED SLOTLINE ANTENNA AS A HOLOGRAPHIC ANTENNA FEED

BY
SHERYL THINGVOLD

A Thesis
Submitted to the Faculty of Graduate Studies
In Partial Fulfillment of the Requirements
for the Degree of

MASTER OF SCIENCE

Department of Electrical and Computer Engineering
University of Manitoba
Winnipeg, Manitoba, Canada

THE UNIVERSITY OF MANITOBA

FACULTY OF GRADUATE STUDIES

*****

COPYRIGHT PERMISSION PAGE

THE LINEAR TAPERED SLOTLINE ANTENNA AS A HOLOGRAPHIC ANTENNA FEED

BY

SHERYL THINGVOLD

A Thesis/Practicum submitted to the Faculty of Graduate Studies of The University

of Manitoba in partial fulfillment of the requirements of the degree

of

Master of Science

Abstract

The holographic antenna has been validated as a high gain planar antenna in the Ka-band frequency range. It may potentially replace existing technologies such as reflectors and phased array antennas where a high gain low profile antenna is required. However, current feed devices for this antenna, including horns and open waveguides, are bulky, which detracts from the attractive silhouette of the hologram.

The linear tapered slotline antenna is proposed as an alternative to these feed devices. This antenna may be etched onto the same substrate as the holographic antenna providing a single unit compact antenna. To facilitate the design process, the holographic antenna's efficiency was formulated to determine the holographic antenna dimensions and feed patterns that generate optimal performance. By quantifying the various losses incurred in the system, a direct correlation between antenna parameters and antenna performance was provided. As such, a systematic approach was taken to optimize the performance of the holographic antenna by using the linear tapered slotline antenna to generate the desired feed patterns.

Table of Contents

ABSTRACT		ii
TABLE OF CONTENTS		iii
LIST OF FIGURES		vi
LIST OF TABLES		xii
Chapter 1	**INTRODUCTION**	1
1.1	Overview	1
1.2	Motivation	3
1.3	Scope	4
Chapter 2	**THE HOLOGRAPHIC ANTENNA**	6
2.1	Introduction	6
2.2	Theory	7
2.3	Samples	10
2.4	Holographic Antenna Efficiency	14
2.5	Holographic Antenna Far Field Calculation	15
2.6	Conclusion	21
Chapter 3	**THE TAPERED SLOTLINE ANTENNA**	23
3,1	Introduction	23
3.2	General Theory of a Tapered Slotline Antenna	24

3.3	Tapered Slotline Antenna Feed	34
	3.3.1 Slotline	34
	3.3.2 Microstrip Line	36
	3.3.3 Microstrip/Slotline Transition	38
3.4	Far Field Radiation Pattern of the Linear Tapered Slotline Antenna	41
3.5	Design Samples	49
3.6	Conclusion	55
Chapter 4	**HOLOGRAPHIC ANTENNA EFFICIENCY**	**58**
4.1	Introduction	58
4.2	Antenna Efficiency	59
4.3	Efficiency Derivation	63
	4.3.1 Problem Formulation	63
	4.3.2 Spillover Efficiency	68
	4.3.3 Taper Efficiency	69
	4.3.4 Termination Efficiency	73
4.4	Generation of Design Curves	78
4.5	Efficiency Validation	84
	4.5.1 Open Waveguide Feed	84
	4.5.2 Printed Dipole Antenna Feed	87
4.6	Conclusion	90
Chapter 5	**HOLOGRAPHIC ANTENNA FEED DESIGN**	**92**
5.1	Introduction	92
5.2	Holographic Antenna LTSA Feed Design	93
	5.2.1 Initial Feed Design	93
	5.2.1 High Efficiency Feed Design	101
5.3	Conclusion	110

Chapter 6	**CONCLUSION**	**111**
6.1	Conclusions	111
6.2	Future Research	113
Appendix A	**ALTERNATIVE FORM OF THE RECIPROCITY THEOREM**	**116**
Appendix B	**TERMINATION EFFICIENCY DETAILS**	**119**
REFERENCES		**125**

List of Figures

Figure 2.1: Hologram Formation 8

Figure 2.2: Single Layer Holographic Antenna 12

Figure 2.3: Radiation Pattern of the Holographic Antenna with an Open Waveguide Feed 13
a) H - Plane, Copolarization b) H - Plane, Crosspolarization

Figure 2.4: Holographic Antenna Far Field Calculation Coordinate System 16

Figure 2.5: Holographic Antenna Calculated Far Field Radiation Pattern, 20
H - Plane, Copolarization

Figure 3.1: Tapered Slot Antenna Variations 25
a) Non-Linear Taper b) Constant Width Taper c) Linear Taper

Figure 3.2: Tapered Slot Antenna Radiation Patterns 27
a) E - Plane, Copolarization b) H - Plane, Copolarization

Figure 3.3: Surface Wave 28

Figure 3.4: $k_o d$ vs βd Diagram Depicting Slow Wave Travel 31

Figure 3.5: Linear Tapered Slotline Antenna Dimensions 32

Figure 3.6: Slotline 34
a) Geometry b) Fields

Figure 3.7: Microstrip Line 37
a) Geometry b) Fields

Figure 3.8: Microstrip/Slotline Transition 39
a) Geometry b) Equivalent Circuit

Figure 3.9: Slotline vs Microstrip Line Impedance 40

Figure 3.10: LTSA Far Field Calculation Geometry 42

Figure 3.11: LTSA Aperture Plane Field Geometry 45

Figure 3.12: LTSA Calculated Far Field Radiation Pattern, 48
E - Plane, Copolarization

Figure 3.13: Linear Tapered Slotline Antenna 49

Figure 3.14: Measured and Simulated Results of an LTSA 52
with a 6^{o} Taper Angle
a) E - Plane, Copolarization b) H - Plane, Copolarization

Figure 3.15: Measured and Simulated Return Loss Results of an LTSA 53
with a 6^{o} Taper Angle

Figure 3.16: Measured and Simulated Results of an LTSA with a 15^{o} Taper Angle
a) E - Plane, Copolarization b) H - Plane, Copolarization 54

Figure 3.17: Measured and Simulated Return Loss Results of an LTSA with a 15^{o} Taper Angle 55

Figure 4.1: Holographic Antenna with Feed 60

Figure 4.2: Configuration of a Holographic Antenna Occupying a Cone 64

Figure 4.3: Normalized Feed Gain Patterns for Efficiency Derivation 67

Figure 4.4: Copolar and Crosspolar Electric Field Components of Feed Pattern 71

Figure 4.5: Sectoral Shaped Holographic Antenna Area 73

Figure 4.6: Holographic Antenna Geometry for Termination Efficiency Calculation 75

Figure 4.7: Efficiencies for a *10 cm* by *10 cm* Diamond Shaped Holographic Antenna 79/80
a) Spillover Efficiency b) Taper Efficiency c) Termination Efficiency

Figure 4.8: Termination Efficiency for a *20 cm* by *20 cm* Diamond Shaped HolographicAntenna 82

Figure 4.9: Termination Efficiency for a *10* by *10 cm* Hologram vs Radiation Loss 82

Figure 4.10: Total Efficiency for the Holographic Antenna 83
a) *10 cm* by *10 cm* Hologram b) *20 cm* by *20 cm* Hologram

Figure 4.11: Radiation Pattern of an Open Waveguide, 85
E - Plane, Copolarization

Figure 4.12: Total Efficiency for an $n = 3$ Feed Pattern 86

Figure 4.13: Radiation Pattern of the Holographic Antenna with a Printed Dipole Feed, 88
H - Plane, Copolarization

Figure 4.14: Radiation Pattern of the Printed Dipole Antenna, 88
E - Plane, Copolarization

Figure 4.15: Total Efficiency for an $n = 2$ Feed Pattern 89

Figure 5.1: Normalized Simulated Near Field Radiation Pattern of a 95
$2\gamma = 13.6^{o}$ LTSA
a) E - Plane, Copolarization b) H - Plane, Copolarization

Figure 5.2: Phase Distribution @ *1 cm* from the 96
$2\gamma = 13.6^{o}$ LTSA Phase Center

Figure 5.3: Photograph of the Holographic Antenna with an LTSA Feed 97

Figure 5.4: Measured Holographic Antenna Results 98
with a $2\gamma = 13.6^{o}$ LTSA Feed,
a) Return Loss b) Far Field Radiation Pattern: H - Plane Copolarization

Figure 5.5: Radiation Pattern of a $2\gamma = 13.6^{o}$ LTSA with an $n = 1.5$ Feed Pattern, E - Plane, Copolarization 99

Figure 5.6: Total Efficiency of an $n = 1.5$ Feed Pattern 100

Figure 5.7: Radiation Pattern of a Holographic Antenna with Copper Strips Reducing Spillover Loss 101

Figure 5.8: Total Efficiency of an $n = 5$ Feed Pattern 102

Figure 5.9: Simulated Far Field Results of a $2\gamma = 32^{o}$ LTSA a) E - Plane, Copolarization with $n = 5$ Feed Pattern b) Phase Distribution 104

Figure 5.10: Measured Holographic Antenna Results with a $2\gamma = 16^{o}$ LTSA Feed a) Return Loss b) Far Field Radiation Pattern: H - Plane, Copolarization 105

Figure 5.11: Radiation Pattern of a $2\gamma = 13.6^{o}$ LTSA with $n = 5$ Feed Pattern, H - Plane, Copolarization 106

Figure 5.12: Simulated and Measured Gain of a $2\gamma = 13.6^{o}$ LTSA, E - Plane, Copolarization 107

Figure 5.13: Measurements of an LTSA with and without Taper Extensions, 108

E - Plane, Copolarization

Figure 5.14: Measurements of the LTSA with and without Substrate Extensions, E - Plane, Copolarization 109

Figure B.1: Holographic Antenna Conducting Strips 119

List of Tables

Table 3.1:	Dimensions of the LTSAs at *30 GHz,* $2\gamma = 6^o$ and $2\gamma = 15^o$	50
Table 3.2:	Dimensions of the Microstrip - Slotline Transition at *30 GHz*	50
Table 3.3:	Measurement Results of the $2\gamma = 6^o$ and $2\gamma = 15^o$ LTSA Antennas	51
Table 4.1:	Efficiency Validation Results	90
Table 5.1:	Dimensions of the $2\gamma = 13.6^o$ LTSA at *30 GHz,*	93
Table 5.2:	Dimensions of the $2\gamma = 16^o$ LTSA at *30 GHz,*	103
Table 5.3:	Efficiency Results of Holograms with an LTSA Feed	109

Chapter 1: Introduction

1.1 Overview

An antenna serves to collect or radiate electromagnetic waves, thus functioning as a transitioning device which converts guided waves to free-space wave propagation. Gain is a significant antenna parameter which defines the antenna's ability to focus its energy in a particular direction. Generally, antenna gain requirements depend directly on the intended application. High gain antennas are vital in detection systems which deal with a very low signal level, such as in remote sensing or radio astronomy. Various communication systems including satellite or point to point networks also require high gain antennas to overcome prohibitive high path loss occasioned by large distances. Another key antenna parameter is the operational frequency; future communication systems are progressing towards the higher frequency bands due to voluminous traffic considerations in the lower frequency regions. In addition, planar antennas are coveted to fulfill functional purposes such as aerodynamic installation or simply to conform to aesthetic objectives. Consequently, antenna engineers are faced with the challenge of designing high gain planar antennas.

Presently, reflectors, lenses, and microstrip phased array antennas are generally employed

where high gain antennas in the Ka frequency band (*26GHz - 40GHz*) are required. These systems contain limitations. The reflector and lens antennas, though very efficient, are hindered by their cumbersome size, and these designs cannot meet low profile requirements. Phased array antennas are attractive due to their low profile silhouette and beam steering abilities. However, at high operating frequencies, particularly in the millimeter wave range and beyond, losses in the feed network become very detrimental. Phased array antennas are also very complex and can be costly to fabricate. The holographic antenna has been proposed as an alternative to these technologies, where a low profile high gain antenna in the Ka - band frequency range is required.

A holographic antenna employs the principles of holography, which have been extended from their traditional usage in the optical frequency range, to the problem of antenna sythesis. Optical holography deals with the storage and retrieval of an image, although the fundamentals may be applied to any range of the frequency spectrum where monochromatic sources are available [1]. The use of holography concepts in side - looking radar in the 1950's stimulated interest in the possible merits of holography elsewhere in the field of electrical engineering [2]. Several researchers recognized the potential of holography as applied to antenna design, although, not much progress has been made in this field, resulting in only a few scattered publications since 1970 [3,4,5].

This prior research has explored various types of holographic antennas culminating in the dipole volume type holographic antenna designed by K. Levis in 1999 [6]. This antenna

models the interference pattern between the desired radiation pattern and the feed pattern. As such, holographic antennas may be easily conceptualized simply by viewing this pattern. The composite antenna then constitutes the hologram and an illuminating device. This antenna has been validated as a high gain antenna, adduced by its low profile and lightweight attributes with potentially no upper operational frequency limit owing to its origin in optical theory.

More research must now be accomplished to contribute to the advancement of this versatile antenna.

1.2 Motivation

The development of holographic antennas has not yet reached maturity. Holographic antennas possess versatility enabling it to accommodate various functions such as multi focal points for multi-beam applications from a shared aperture. They may provide compactness, enabling flush mounting, hence meeting various physical constraints.

Prior research in this area of holographic antenna study has demonstrated their potential as high gain antennas complemented by their low profile silhouette. However, previous designs utilize a waveguide or horn as a feed which detracts from the planar nature of the holographic antenna. Therefrom, the linear tapered slotline antenna has been proposed as

an alternate feed method which would maintain the planar silhouette of the holographic antenna.

In addition, due to the early stages of this development, guidelines do not exist to determine the most efficient feed option for the holographic antenna. A formulation is needed to ascertain the feed which would generate optimal holographic antenna efficiency. As such, parameters such as holographic antenna size, and feed pattern generation should be considered.

Finally, this formulation could be used to assess the most efficient feed pattern option and the linear tapered slotline antenna can be designed to generate the necessary curve. This feed may then be etched onto the same substrate as the holographic antenna providing a single unit integrated antenna.

1.3 Scope

The second chapter details the background of holographic antennas with a specific focus on the hologram used in this thesis. Some theoretical concepts are discussed including a derivation of the far field pattern of holographic antennas.

Chapter 3 introduces the tapered slot antenna and outlines its potential as a holographic antenna feed. Design guidelines are discussed and finally two prototypes were built to

assess the linear tapered slotline antenna's feasibility as a holographic antenna illuminating device.

Chapter 4 discusses the efficiency of the holographic antenna, and itemizes the influential parameters. A formulation was then derived to determine their impact on overall holographic antenna efficiency dependent on feed selection and holographic antenna size. A graphical depiction of this formulation was generated to serve as a design aid in future holographic antenna research.

Finally, in Chapter 5, the formulation derived in Chapter 4 was utilized to design a more efficient holographic antenna. This involved designing a linear tapered slotline antenna to generate the feed patterns needed for more effective hologram radiation.

This is followed by a concluding chapter which summarizes the work conducted in this thesis, the overall results, findings, and future work.

Chapter 2: The Holographic Antenna

2.1 Introduction

Current trends in wireless technology are towards high gain antennas that can operate in the Ka - band frequency range and beyond, due to the cluttering of the spectrum at lower frequencies. High gain antennas are required for many applications including radar, satellite, and terrestrial wireless communications. In some applications, low-profile and light weight designs are also preferable for aerodynamic and aesthetic installation, in addition to the high gain requirement.

Presently, parabolic, lens, and phased array antennas are employed to satisfy these criteria, however, both systems contain limitations. Parabolic and lens antennas are hindered by their cumbersome size, and phased array antennas suffer from poor efficiency due to their lossy feed networks. The holographic antenna is proposed as an alternative to these technologies. It may provide high gain in the Ka - band frequency range, complemented by its desirable low-profile and lightweight configuration.

In this chapter, general concepts of holographic principles are reviewed with emphasis on their application to antenna designs.

2.2 Theory

Traditionally, holograms are recognized as image forming devices in the optical frequency range. The interference pattern of light that has been reflected from an object and a reference wave is recorded to produce the hologram. When this recording is illuminated by the reference wave, an image of the initial object is generated. This holographic theory may be applied to any range of the frequency spectrum, where monochromatic sources are available [3]. Generally speaking, the hologram becomes a recording of the interaction between a reference wave and an object wave, as shown in Figure 2.1. When this hologram is illuminated by either one of these waves, the other is generated [7].

Mathematically, the object wave, U_o, and the reference wave, U_r, sum to form a complex amplitude transmittance, t, as demonstrated by Saleh et al. in [7]. This is shown in equation (2.1).

$$t \propto |U_o + U_r|^2 = |U_r|^2 + |U_o|^2 + U_r^* U_o + U_r U_o^* \tag{2.1}$$

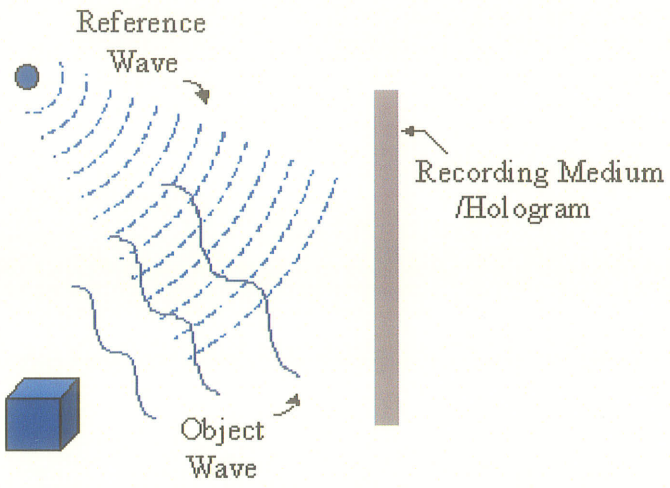

Figure 2.1: Hologram Formation [7]

The terms $|U_r|^2$ and $|U_o|^2$ are denoted as the wave intensities, and can be written as I_r and I_o, respectively. Thus, through algebraic manipulation, equation (2.1) can be written as,

$$t \propto I_r + I_o + 2\sqrt{(I_r I_o)}\cos(\arg(U_r) - \arg(U_o)) \tag{2.2}$$

When this transmittance is illuminated by the reference wave, the object wave is reconstructed, as demonstrated in equation (2.3).

$$U = tU_r \propto U_r I_r + U_r I_o + I_r U_o + U_r^2 U_o^* \tag{2.3}$$

The object wave is contained in the third term on the right hand side, multiplied by the intensity of the reference wave, which can be separated from the other terms using various techniques.

The principles of holography have many different applications ranging from the optical to microwave frequency spectrum. Microwave holography has been implemented in coherent, or, side-looking radar, and radio communications. It has also been used as a technique to improve the performance of large reflector and beam waveguides by optimizing crucial parameters [8,9]. Holography may also aid in compact range measurements where a planar hologram serves as a plane wave generating device [10].

Of particular interest is the application of holography to antenna synthesis. As a hologram is designed by approximating the interference pattern between two waves of interest, in holographic antenna design these are the waves emanating from the feed and the desired radiation pattern. This hologram, in addition to the source providing the illuminating wave, constitute the antenna. As such, many different potential holographic antennas exist, where radiation patterns and feed selection may be chosen depending on the desired application.

Most of the study in this area was confined to the 1970's where various methods of constructing holographic antennas were considered with successful results [3,4,5]. K. Levis has followed up on this research in her 1999 master's thesis titled "Ka-Band Holographic Antennas" [6].

The following section provides an overview of existing holographic antennas with emphasis on the single layer hologram design as it is the focus of this work.

2.3 Samples

As a holographic antenna models the interference pattern between two waves of interest, the central problem lies in physically reproducing this pattern. Checcacci has introduced three potential methods of holographic antenna construction [3,4]. The two waves of interest were a spherical wave (feed pattern) and a wave radiating from a parabolic antenna (desired far field pattern), and the resulting interference pattern resembles a sinusoidal wave with varying periods and intensities.

Firstly, a phase hologram was proposed which consists of a paraffin plate molded to emulate the interference pattern [3]. This type of holographic antenna is called a phase hologram and is also known as a lens antenna. Next, a zone plate was constructed by approximating the wave generated by the interference pattern with either metallic strips or dielectric strips with an area proportional to the area of the fringe width of the curve. This type of hologram reserves the periodicity and fringe widths of the interference pattern. Lastly, a hologram was constructed which profiles only the periodicity of the pattern by placing dielectric or metallic rods at the pattern's nulls. Although these methods provide only a crude approximation of the interference pattern, when illuminated by a spherical wave, all successfully regenerated the parabolic antenna wave as desired.

Iizuka et al. has followed up on this investigation by introducing a type of zone plate hologram which models the interference pattern between a planar and spherical wave at *12 GHz* [5]. The hologram resembles a series of concentric metallic rings etched on a dielectric substrate which approximates the minima of the interference pattern between the two aforementioned waves. When illuminated by a spherical wave, this hologram generates a planar wave which radiates in broadside direction from both sides of the antenna. Iizuka et al. then proposed a volume type hologram which suppresses the beam radiating from the backside of the hologram and redirects it upwards where it adds in phase with the existing beam. This volume antenna consists of two holographic antennas which are stacked and spaced a quarter of a wavelength apart, resulting in a unidirectional beam radiating in a broadside direction from the antenna and an increase in gain of *7 dBi*.

K. Levis has pursued this area of research by constructing a holographic antenna based on Iizuka's design at a frequency of *30 GHz* [6]. This holographic antenna models the destructive interference pattern, at a frequency of *30 GHz*, between a spherical and a planar wave. A matlab program was generated to view this pattern, which resembles a series of concentric rings [11]. The nulls in this pattern were approximated by periodic copper strips etched onto a dielectric substrate which will maintain the sought amplitude of zero as the tangential electric field component existing on a metallic surface is zero. A diamond shaped antenna was chosen to favor horizontal polarization, and the width of the conducting strips was kept as minimal as realizable. An image of the design is shown below in Figure 2.2.

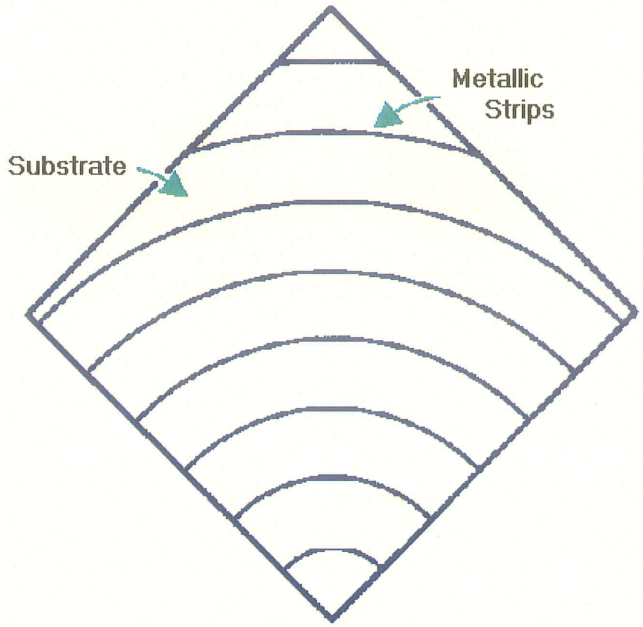

Figure 2.2: Single Layer Holographic Antenna [6]

The hologram is illuminated by a spherical wave feed located at the focal point of the copper rings. Both a horn antenna and an open waveguide were tested as feed options. They were located, with manual alignment of their phase centers, at the apex of the antenna. The resulting measured radiation pattern of the holographic antenna with the open waveguide as a feed is shown in Figure 2.3 accompanied by an image displaying the location of the radiating beams. This pattern demonstrates a maximum gain of *16.15 dBi* at *30 GHz*.

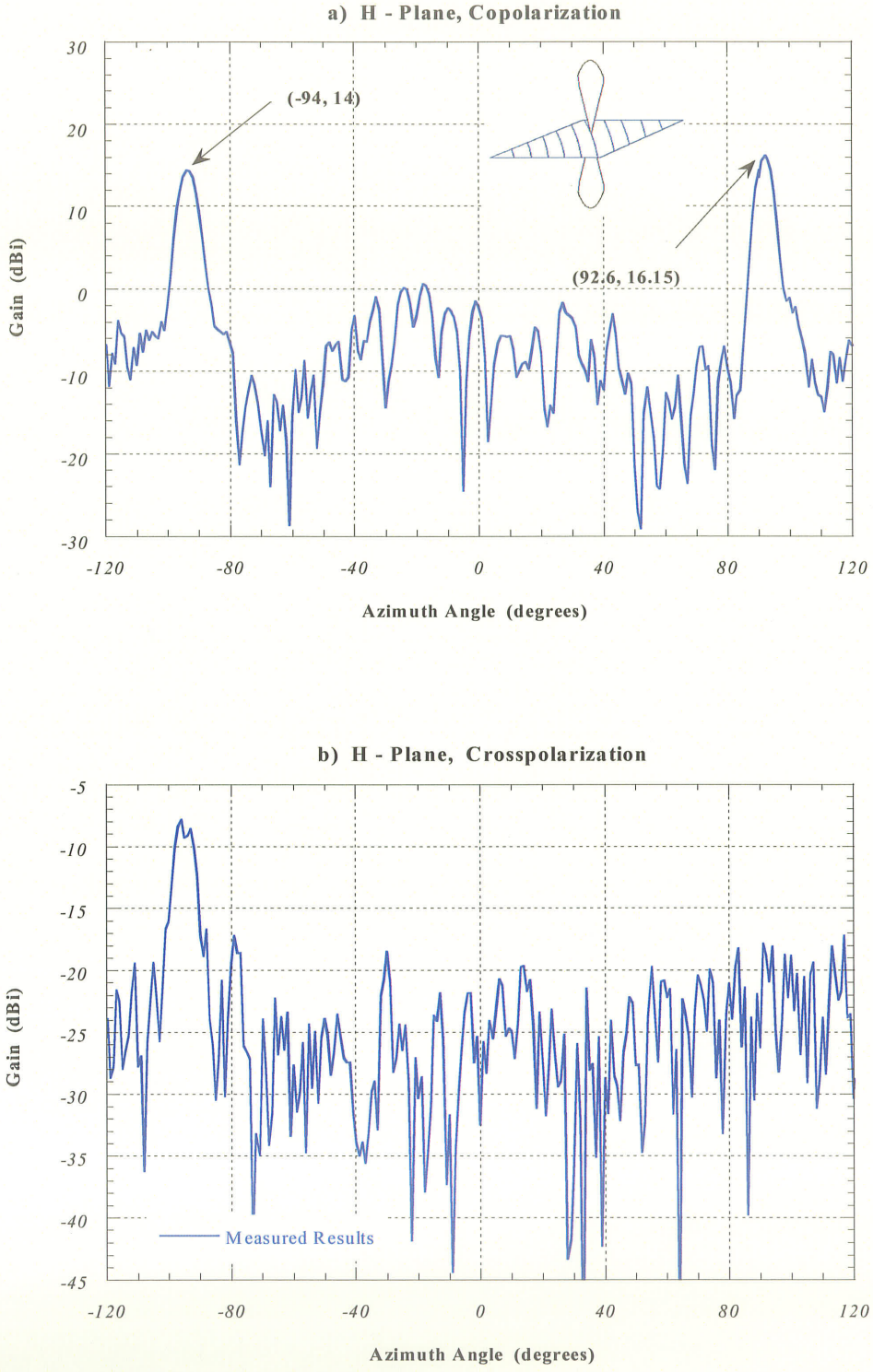

Figure 2.3: Radiation Pattern of the Holographic Antenna with an Open Waveguide Feed [6]
a) H - Plane, Copolarization b) H - Plane, Crosspolarization

A volume type hologram was then generated based on this design where two holographic antennas were stacked and offset at a quarter wavelength spacing. The design successfully redirected the bottom lobe at $\theta = -90^{o}$ towards the front lobe at $\theta = 90^{o}$, generating an increase in gain of *6 dBi*. Following this a dipole hologram was designed which approximates the circular conducting strips by an array of horizontally polarized dipoles. As such, only the horizontal components of the feed wave are scattered, enabling reduction of the cross-polarization levels while maintaining the gain of the single layer continuous strip holographic antenna. The cross polarization level reduction of *30 dBi* at broadside has been achieved by this design.

2.4 Holographic Antenna Efficiency

The single layer holographic antenna designed by K. Levis does not quite meet high gain antenna requirements. This may be due to the poor efficiency of this structure of only *6.25%*. This efficiency has been improved through variations of the original design such as the volume - type hologram and dipole holograms.

To further improve the efficiency of this antenna, thereby increasing the overall gain of the structure, parameters such as hologram shape and size should also be considered, perhaps combined into an array formation to ensure complete radiation of the feed power.

In addition, feed selection is crucial as the feed should illuminate the hologram uniformly while focusing the energy into the hologram. This feed should be aligned properly with

the hologram so as to illuminate it with a spherical wave while introducing minimal phase error into the system.

A thorough holographic antenna efficiency discussion and formulation will be given in Chapter 4.

2.5 Holographic Antenna Far Field Calculation

The treatment of a holographic antenna as an array of conducting arcs has been applied by K. Levis for the far field calculation [6]. However, this approach is solely applicable to holograms constructed from conducting strips. For general cases, the aperture field integration method is preferable.

The far field expression for the holographic antenna can be calculated using Lorentz Reciprocity Theorem, shown below in equation (2.4). This theorem states that two sources, $\bar{J}_1, \bar{M}_1$ and $\bar{J}_2, \bar{M}_2$, radiate at the same frequency to produce fields, $\bar{E}_1, \bar{H}_1$ and $\bar{E}_2, \bar{H}_2$ [12]. The holographic antenna represents one of these sources, $\bar{J}_1$, and $\bar{J}_2$ represents a delta test source which is located in the far field of the holographic antenna. The geometry for the calculation is shown in Figure 2.4.

$$-\nabla \cdot (\bar{E}_1 \times \overline{H_2} - \bar{E}_2 \times \bar{H}_1) = \bar{E}_1 \cdot \bar{J}_2 + \bar{H}_2 \cdot \bar{M}_1 - \bar{E}_2 \cdot \bar{J}_1 - \bar{H}_1 \cdot \bar{M}_2 \qquad (2.4)$$

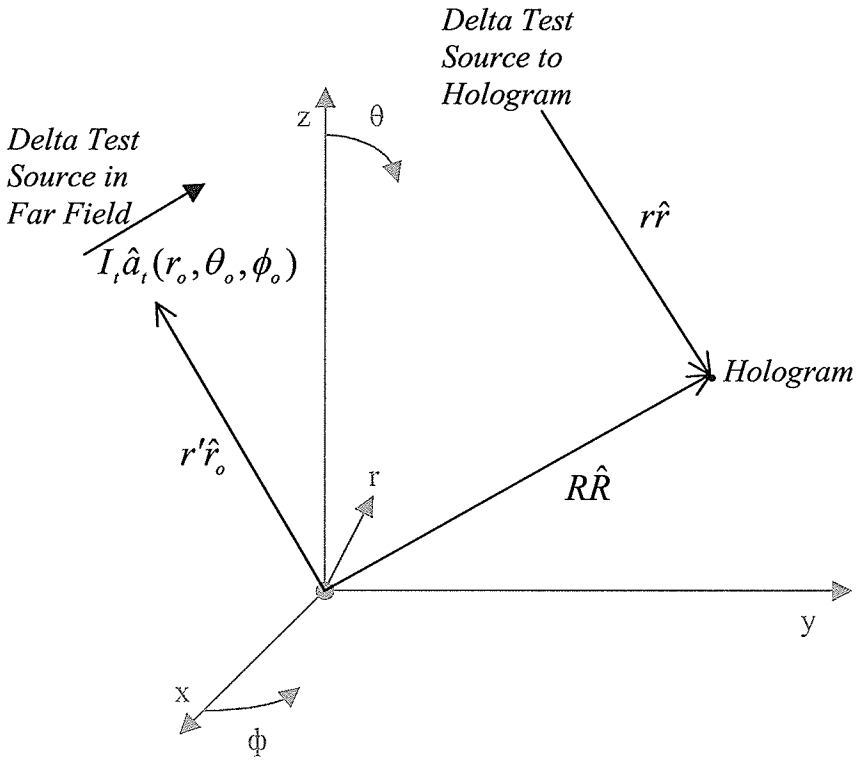

Figure 2.4: Holographic Antenna Far Field Calculation Coordinate System

The observation point is situated in the far field of the hologram, at the location of the delta test source.

The divergence theorem, shown in equation (2.5), is now applied to equation (2.4),

$$\int_v (\nabla \cdot \bar{A}) dv = \oint_s \bar{A} \cdot ds \qquad (2.5)$$

Therefore,

$$-\oint_S (\bar{E}_1 \times \bar{H}_2 - \bar{E}_2 \times H_1) \cdot \hat{n} ds = \int_V (\bar{E}_1 \cdot \bar{J}_2 + \bar{H}_2 \cdot \bar{M}_1 - \bar{E}_2 \cdot \bar{J}_1 - \bar{H}_1 \cdot \bar{M}_2) dv \quad (2.6)$$

Since the holographic antenna is of finite extent, the surface integral vanishes over a spherical surface or radius $r \to \infty$. In addition, there are no magnetic current sources for this problem, therefore, $\bar{M}_1$ and $\bar{M}_2$ are set to zero. Making these substitutions, equation (2.6) may be written as:

$$0 = \int_V (\bar{E}_1 \cdot \bar{J}_2 - \bar{E}_2 \cdot \bar{J}_1) dv \quad (2.7)$$

or,

$$\int_V \bar{E}_1 \cdot \bar{J}_2 dv = \int_V \bar{E}_2 \cdot \bar{J}_1 dv \quad (2.8)$$

where $\bar{J}_1$ is the equivalent current on the holographic antenna.

As a delta source is used as the test source, it is modeled by equation (2.9) in spherical coordinates. The denominator serves to maintain the test source's amplitude of unity when it is integrated. The vector $\hat{a}_t$ represents the orientation of the test source.

$$\bar{J}_2(r') = \frac{\delta(r' - r_o)\delta(\theta' - \theta_o)\delta(\phi' - \phi_o)}{r'^2 \sin\theta'} \hat{a}_t \quad (2.9)$$

This may be substituted into equation (2.8) as follows,

$$\int_v \bar{E}_1 \cdot \frac{\delta(r'-r_o)\delta(\theta'-\theta_o)\delta(\phi'-\phi_o)}{r'^2\sin\theta'}\hat{a}_t r'^2 \sin\theta' dr' d\theta' d\phi' = \int_s \bar{E}_2 \cdot \bar{J}_1 ds \qquad (2.10)$$

In equation (2.10), the volume integral is reduced to a surface integral for a planar holographic antenna.

This expression is evaluated at the point of interest, (r_o, θ_o, ϕ_o),

$$\int_v \overline{E_1} \cdot \frac{\delta(r'-r_o)\delta(\theta'-\theta_o)\delta(\phi'-\phi_o)}{r'^2\sin\theta'}\hat{a}_t r'^2 \sin\theta' dr' d\theta' d\phi = \overline{E_1} \cdot \hat{a}_t = \int_s \bar{E}_2 \cdot \bar{J}_1 ds \qquad (2.11)$$

The expression for the far field of a delta test source, oriented in the $\hat{a}_t$ direction, as derived in [13] is,

$$\bar{E}_2(x,y,z) = \frac{-j\omega\mu}{4\pi}\frac{e^{-jkr_o}}{r_o} e^{jk[x\sin\theta_o\cos\phi_o + y\sin\theta_o\sin\phi_o + z\cos\theta_o]}[\hat{a}_t - (\hat{a}_t \cdot \hat{r}_o)\hat{r}_o] \qquad (2.12)$$

This may introduced into equation (2.11) to yield the general expression for the far field of a holographic antenna. The orientation of $\hat{a}_t$ may then be chosen to view the desired polarization component.

$$\overline{E_1} \cdot \hat{a}_t = \int_s \frac{j\omega\mu}{4\pi} \frac{e^{-jkr_o}}{r_o} e^{jk[x\sin\theta_o\cos\phi_{oo} + y\sin\theta_o\sin\phi_o + z\cos\theta_o]} [\hat{a}_t - (\hat{a}_t \cdot \hat{r}_o)\hat{r}_o] \cdot \bar{J}_1 ds \quad (2.13)$$

The holographic antenna, constructed from conducting strips', current density, $\bar{J}_1$, can be written as a summation of the currents existing of the individual arcs as,

$$\bar{J}_1(r, \phi) = \sum_{i=1}^{N} \frac{\delta(R - R_i)}{R} (\cos(\phi - \pi/2))^{n/2} \hat{a}_\phi \quad (2.14)$$

where N is the total number of conducting strips and $(\cos(\phi - \pi/2))^{n/2}$ is the field pattern existing on the holographic antenna and will be discussed further in Chapter 4.

This may now be substituted into equation (2.13) for the far field,

$$\bar{E}_1 \cdot \hat{a}_t = \sum_{i=1}^{N} \int_{R_o}^{R_L} \int_{\pi/4}^{3\pi/4} \frac{j\omega\mu}{4\pi} \frac{e^{-jkr_o}}{r_o} e^{jk[x\sin\theta_o\cos\phi_o + y\sin\theta_o\sin\phi_o + z\cos\theta_o]} \frac{\delta(R - R_i)}{R}$$

$$\ldots (\cos(\phi - \pi/2))^{n/2} [\hat{a}_t - (\hat{a}_t \cdot \hat{r}_o)\hat{r}_o] \cdot \hat{a}_\phi R d\phi dR \quad (2.15)$$

Choosing $\hat{a}_t = \hat{a}_{\phi_o}$ would enable determining the hologram's far field H - plane copolarization pattern. Consequently,

$$\overline{E_1} \cdot \hat{a}_{\phi_o} = \sum_{i=1}^{N} \int_{\pi/4}^{3\pi/4} \frac{j\omega\mu}{4\pi} \frac{e^{-jkr_o}}{r_o} e^{jkR_i[\sin\theta\sin\theta_o\cos\phi\cos\phi_o + \sin\theta\sin\theta_o\sin\phi\sin\phi_o + \cos\theta\cos\theta_o]} \cdots$$

$$(\cos(\phi - \pi/2))^{n/2} \cos(\phi_o - \phi) d\phi \qquad (2.16)$$

where x, y and z have been converted into their spherical coordinate equivalents and $\hat{a}_{\phi_o} \cdot \hat{a}_{\phi} = \cos(\phi_o - \phi)$.

This normalized radiation pattern is depicted in Figure 2.5, demonstrating the desired beam peaks at 0^o and 180^o, and sidelobe levels of less than *-20 dBi*.

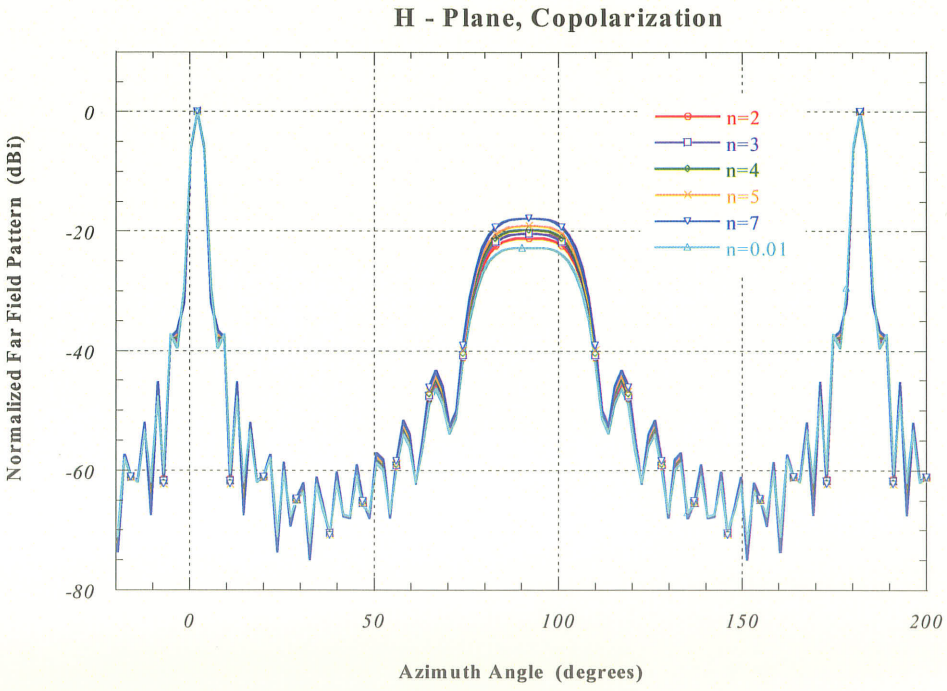

Figure 2.5: Holographic Antenna Calculated Far Field Radiation Pattern

2.6 Conclusion

Traditional optical holographic theory has been applied to the microwave frequency region for use in multiple applications. Among these applications, the principles have been successfully applied to the problem of antenna synthesis. Various designs have demonstrated the potential of the holographic antenna to generate any desired radiation pattern by constructing a crude model of the interference pattern between the radiation and feed patterns. Thus, antenna design may be conceptualized by simply viewing this interference pattern.

In the Ka - band frequency range, the holographic antenna has been validated as a viable high gain antenna. It is, however, hindered by previous non-planar feed choices. These waveguides and horn feeds require manual alignment with the holographic antenna. This is cumbersome to the user and can introduce significant efficiency degradation due to misalignment into the system.

An attractive feature of the holographic antenna is its planar profile, however current feed methods detract from this attribute. Horn antennas and waveguides are bulky and do not allow for applications where flush mounting is desired.

The linear tapered slot antenna is proposed as a feed alternative. This antenna can generate the required spherical illumination wave while maintaining the low profile characteris-

tics of the hologram. It may also be etched onto the same substrate as the holographic antenna resulting in a single unit antenna and eliminating alignment issues.

The single layer diamond shaped holographic antenna is chosen as the focus of this work, once the new feed method has been designed, it can be applied to other holographic antennas designs such as the volume type hologram, and dipole hologram.

Chapter 3: The Tapered Slotline Antenna

3.1 Introduction

The holographic antenna is formed by modeling the interference pattern of two waves. In this application, the two waves chosen were a spherical wave and a planar wave which interfere to produce a fringe pattern of concentric rings. This pattern is modeled by a set of periodic metallic strips etched in copper on a dielectric substrate. When this interference pattern is illuminated by a spherical wave, a planar wave is generated in a broadside direction. Therefore, a holographic antenna feed is required to launch this spherical wave into the antenna.

Prior feed methods have included open waveguides and horn antennas which successfully generate the required spherical illumination wave. However, they are both bulky which detracts from the planar nature of the holographic antenna. In addition, these feeds require manual alignment with the holographic antenna which is cumbersome to the designer. This alignment is prone to error and can introduce loss into the system.

The linear tapered slot antenna (LTSA) has been proposed as an alternative to existing feed devices. The LTSA can generate the required spherical wave while maintaining the

low profile characteristics of the holographic antenna. This antenna may also be etched onto the same substrate as the hologram, providing a single unit antenna and eliminating any alignment issues.

This chapter provides an overview of tapered slot antennas, design considerations, and its potential as a holographic antenna feed.

3.2 General Theory of a Tapered Slotline Antenna

The tapered slotline antenna, TSA, consists of a slotline which is flared to promote radiation at one end. This tapered slot is cut into a thin film of metal, and backed, either with or without, a dielectric substrate. The taper functions to transform the guided wave from the slotline to a radiating plane wave. Many different variations of the taper profile exist, and they are shown in Figure 3.1. These different tapers may be classified as non-linear taper, linear taper, or constant width taper. Figure 3.1 a) displays a popular form of the TSA which is called the classical vivaldi antenna. It is discerned by its exponential taper design, which was developed by Gibson in 1979 [14].

The tapered slot antenna may be employed when a flush-mounted, or low silhouette design is required. The low profile TSA design lends itself well to full integration with MICs and other circuitry, or use in array applications [15,16].

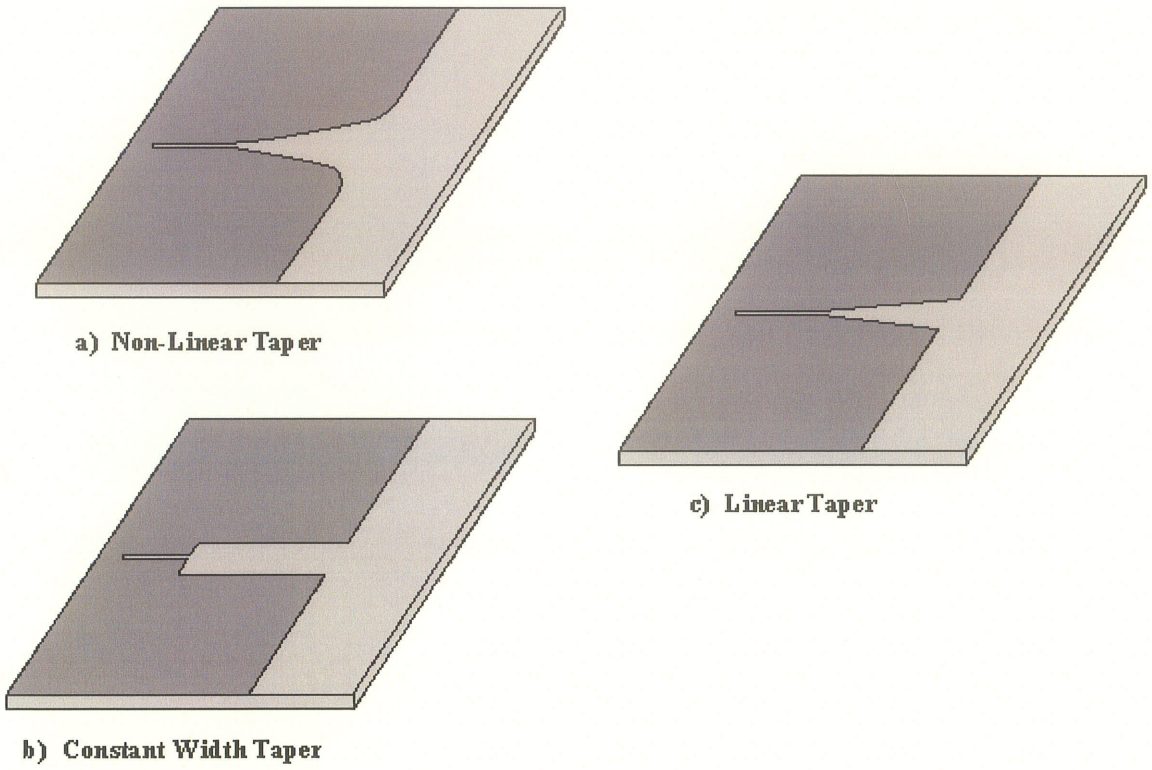

Figure 3.1: Tapered Slot Antenna Variations
a) Non-Linear Taper b) Constant Width Taper c) Linear Taper

Single element TSAs may be employed as feeds for reflector antennas or use in receiver/ transmitter devices. When combined into an array, TSAs have applications ranging from imaging, and satellite communications to spatial power combining [17]. The TSA has higher gain when compared to the planar microstrip antenna; single element gain can be achieved between *12* and *20 dBi* with sidelobe levels of approximately *12 dBi*, and good cross-polarization characteristics [18]. The operational bandwidth of a tapered slot antenna is also higher than that of a microstrip antenna due to its travelling wave nature. TSAs are advantageous at higher frequencies as the geometry of resonant microstrip antennas becomes minute and the ensuing fabrication is costly, due to their tight tolerance

requirement [19]. At high frequencies, resonant microstrip antennas also suffer from poor efficiency due to conduction losses. Tapered slot antennas are desirable at higher frequencies as they retain lower losses, however, are hindered by their larger size [19].

Tapered slot antennas radiate in the end-fire direction with symmetrical beams in the E and H planes over the significant portion of the main lobe [15]. Figure 3.2 displays typical E and H plane patterns of the TSA. The radiated electric field is linearly polarized and parallel to the plane of the TSA. The magnetic field is perpendicular to this electric field.

The tapered slot antennas possess a broadband characteristic, exhibiting multi-octave bandwidth capabilities, with constant gain over the bandwidth: it has been demonstrated in [14] that a TSA can maintain the *10 dBi* gain over a frequency bandwidth from *2 GHz* through *40 GHz*. This broadband performance has been attributed to the fact that different portions of the taper radiate at different frequencies [20]. The lower frequency limit is imposed by the narrow end of the slotline while the higher end of the frequency band is determined by the width of the tapered slot [21]. In practice, however, the feed process will limit the achievable operational bandwidth [22]. Difficulty arises when trying to match the high impedance slotline to the feed network. Impedance mismatch can occur leading to standing waves in the feed [21]. These feed methods include transmission lines, microstrip lines, waveguides, and the probe feed, which all serve to excite a wave in the narrow end of the slotline of the TSA.

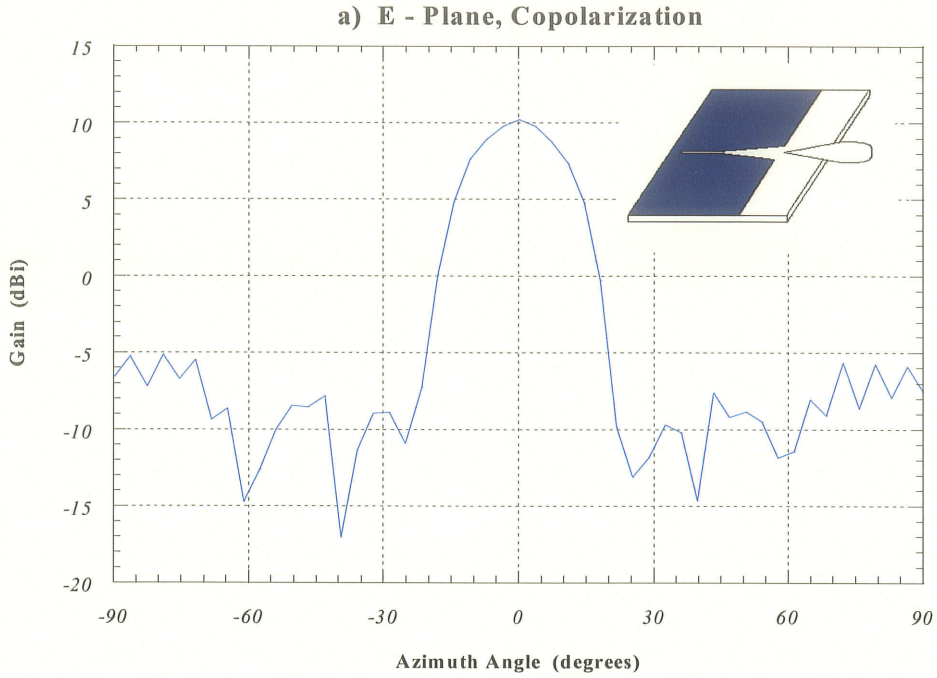

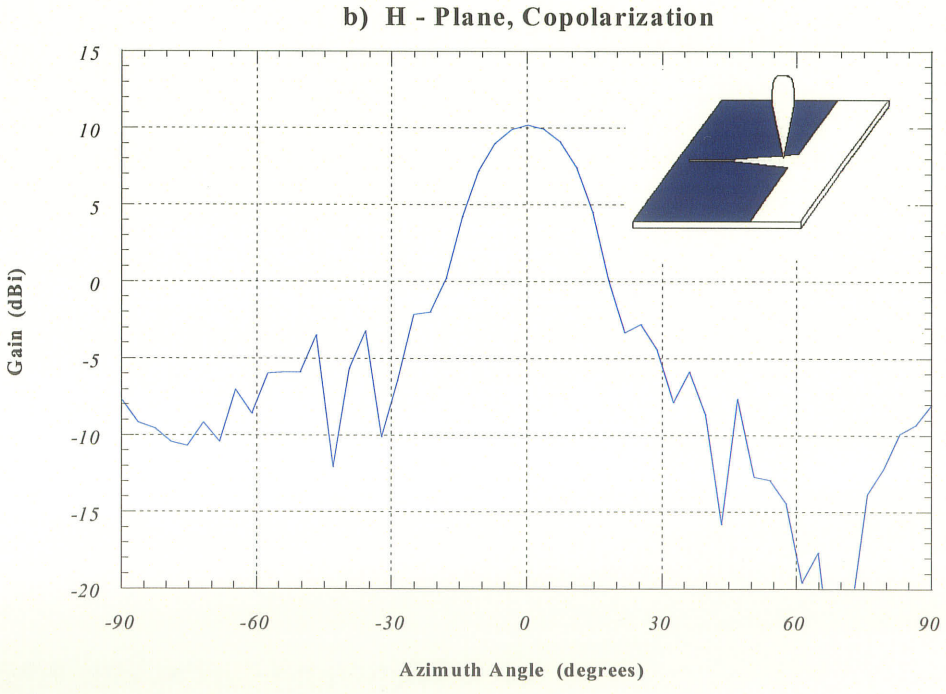

Figure 3.2: Tapered Slot Antenna Radiation Patterns
a) E - Plane, Copolarization b) H - Plane, Copolarization

The tapered slot antenna is classified as a traveling wave antenna [23], specifically, this antenna belongs to the surface wave variety [15]. Surface wave antennas typically radiate in an end-fire direction. These surface waves propagate along the guiding structure and attenuate exponentially away from the interface, radiating when they reach the edge of the structure, or at the discontinuities. Figure 3.3 displays the wave's exponential decay while propagating along the medium in the positive z direction.

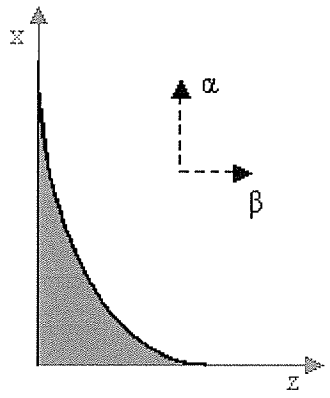

Figure 3.3: Surface Wave

Mathematically, a TE field may be expressed as shown in equation (3.1), for a planar guide infinite in the y dimension, assuming a lossless guiding structure.

$$E_y(x,z) = E_{y_o} e^{-\alpha_x x - j\beta_z z} = E_{y_o} e^{-\bar{\gamma}\cdot\bar{r}} \tag{3.1}$$

The attenuation constant, α_x, signifies the exponential decay along the x axis. The phase constant, β_z, indicates propagation along the z axis. These two components are combined to express the propagation constant, $\bar{\gamma}$.

$$\bar{\gamma} = \gamma_x \hat{a}_x + \gamma_z \hat{a}_z = \alpha_x \hat{a}_x + j\beta_z \hat{a}_z \tag{3.2}$$

The field in equation (3.1) is a solution of the source free wave equation for the electric field, presented in equation (3.3),

$$\nabla^2 E_y + k_o^2 E_y = 0 \tag{3.3}$$

where k_o is the free-space wavenumber,

$$k_o = \omega\sqrt{\mu\varepsilon} = \omega/c \tag{3.4}$$

A two-dimensional wave equation, $E_y = E_{y_o} e^{-jk_x x - jk_z z}$, requires that,

$$k_x^2 + k_z^2 = k_o^2 \tag{3.5}$$

where, for a surface wave propagating along the z axis,

$$jk_x = \gamma_x = \alpha_x \tag{3.6a}$$

and,

$$jk_z = j\beta_z \tag{3.6b}$$

The propagation constant from equation (3.2) may be used to determine the phase velocity, v_p, of the surface wave, where,

$$v_p = \omega/\beta_z \tag{3.7}$$

and,

$$k_x^2 = -\alpha_x^2 \qquad k_z^2 = \beta_z^2 \tag{3.8}$$

Therefore,

$$\beta_z = \sqrt{k_o^2 + \alpha_x^2} > k_o \tag{3.9}$$

and,

$$v_p = \omega/\beta_z = k_o c/\beta_z \tag{3.10}$$

As $\beta_z > k_o$, the phase velocity, v_p, of the TSA is therefore slower than the speed of light. The structure propagating this slow wave is known as a slow-wave structure. Figure 3.4 displays a graph of $k_o d$ versus βd [21].

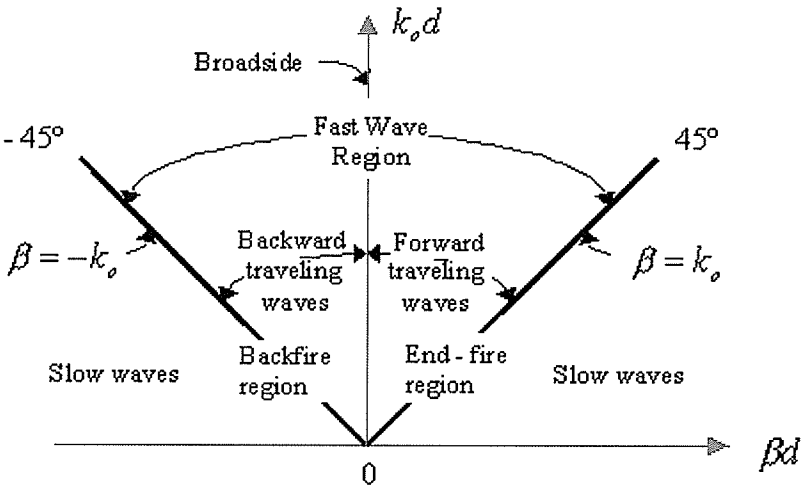

Figure 3.4: $k_o d$ vs βd Diagram Depicting Slow Wave Travel [21]

The TSA antenna lies in furthermost right quadrant of this diagram, depicting forward traveling slow waves which radiate at the termination of the guiding structure in the end-fire direction.

Most of the research performed in this area has been based on empirical studies. Equations have been developed to provide guidelines for the dimensions of the TSA [24]. For a linear tapered slotline antenna the recommended lengths and widths are shown in equation (3.11) through (3.13). A diagram defining these dimensions is illustrated in Figure 3.5.

$$W = L\tan(\gamma) \tag{3.11}$$

$$\frac{D}{W} = 3.3 \tag{3.12}$$

$$D \geq 2.75\lambda_o \tag{3.13}$$

The gain of a TSA improves with the lengthening of the antenna, L, for a given aperture angle, γ [14]. If the length of the antenna is less than λ_o, the antenna will radiate through resonance rather than as a traveling wave antenna [21]. The total width of the antenna, $2D$, should be large enough to mitigate scattering from the edges which causes rippling in the radiation patterns [21].

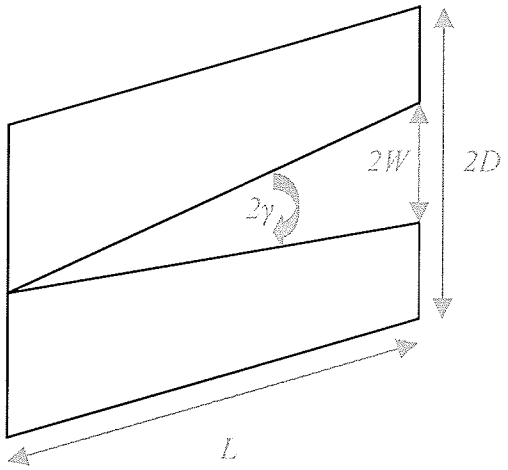

Figure 3.5: Linear Tapered Slotline Antenna Dimensions

Equations have also been derived to determine choice of substrate thickness, t, and dielectric constant, ε_r [15]. These parameters control the rate at which electromagnetic radia-

tion occurs. An equation relating the thickness and permittivity of the substrate is provided in equation (3.14) [17].

$$t_{eff} = t(\sqrt{\varepsilon_r} - 1) \tag{3.14}$$

This effective thickness, t_{eff}, should lie in the range shown in equation (3.15) [17].

$$0.005\lambda_o \leq t_{eff} \leq 0.03\lambda_o \tag{3.15}$$

where λ_o is the free space wavelength.

For an effective thickness above the upper range, undesired substrate modes can develop, which significantly degrade the radiating beam. For values below the lower range, there is a decrease in antenna directivity, coupled with high cross-polarization patterns and less symmetrical beam patterns [23]. Use of an air dielectric results in larger beamwidth patterns [17].

At high frequencies, thin substrates are required to remain within the suggested thickness range recommended in equation (3.15). This results in an impractical fragile antenna. Porous substrates may be used which effectively reduce the effective thickness of the substrate and have demonstrated good radiation performance [25,26].

3.3 Tapered Slot Antenna Feed

3.3.1 Slotline

The tapered slot antenna is composed of a flared slotline which radiates in an endfire direction. A feed is required to excite a wave in the narrow end of the tapered slot or slotline which propagates along the structure. This slotline is composed of a narrow gap in a conductive coating and backed by a dielectric substrate, as shown in Figure 3.6 a).

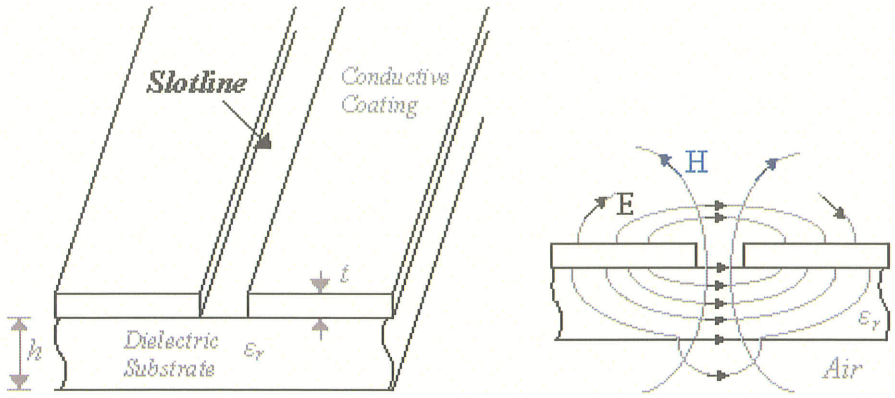

Figure 3.6: Slotline [27]
a) Geometry b) Fields

An applied voltage difference across the conducting edges bordering the slot will excite an electric field that lies in the plane of the slot. The surface current density is greatest at these edges and gradually recedes away from the slot. A depiction of the proximate electric and magnetic field distributions in the slotline is shown in Figure 3.6 b). The mode of propagation is non-TEM, and most resembles the transverse electric mode [28].

The dielectric constant, ε_r, of the substrate will determine how closely bound these fields are to the slotline. A high permittivity value will yield tightly bound fields encouraging transmission along the slotline as opposed to radiation. Since the fields exist simultaneously in the substrate and surrounding free space, an equation has been derived to calculate the effective dielectric constant, ε_{reff}. An approximate value is given in equation (3.16).

$$\varepsilon_{reff} = \frac{\varepsilon_r + 1}{2} \tag{3.16}$$

A high permittivity substrate will beget small wavelengths when compared to those of free-space. An approximate slotline wavelength can be calculated by equation (3.17),

$$\lambda_s = \lambda_o \sqrt{\frac{2}{\varepsilon_r + 1}} \tag{3.17}$$

where λ_o is the free space wavelength.

These slotlines possess no cutoff frequencies and may therefore be employed at any frequency. The slotline impedance, Z_o, varies with frequency and is dependent on the slotline width and choice of substrate. Graphs relating the slotline's wavelength, λ_s,

impedance, Z_o, and geometry are readily available for popular permittivity values for design purposes [27].

3.3.2 Microstrip Line

A microstrip line strategically placed on the backside of the slotline structure can be used to couple energy into the slotline. Other possible feed mechanisms for the slotline are coaxial cables, waveguides, or striplines. The microstrip line is chosen due to its low profile design, which fulfills the requirements of the primary structure, and integrability with other circuitry. Disadvantages to this setup include radiation from the microstrip line, higher conduction loss, and the narrow band characteristic of a microstrip to slotline coupling circuit.

A microstrip line consists of a conducting strip situated above a grounded dielectric substrate, as displayed in Figure 3.7a). The conducting layers form a transmission line where the wave may propagate. The accompanying field distribution is shown in Figure 3.7 b).

This open structure contains a dielectric - air interface which creates fringing fields that prevent the structure from supporting a purely TEM propagation mode, although it is nearly TEM in nature [27]. The electromagnetic fields exist in both the substrate and surrounding air which is accounted for by calculating an effective dielectric constant, ε_{reff}.

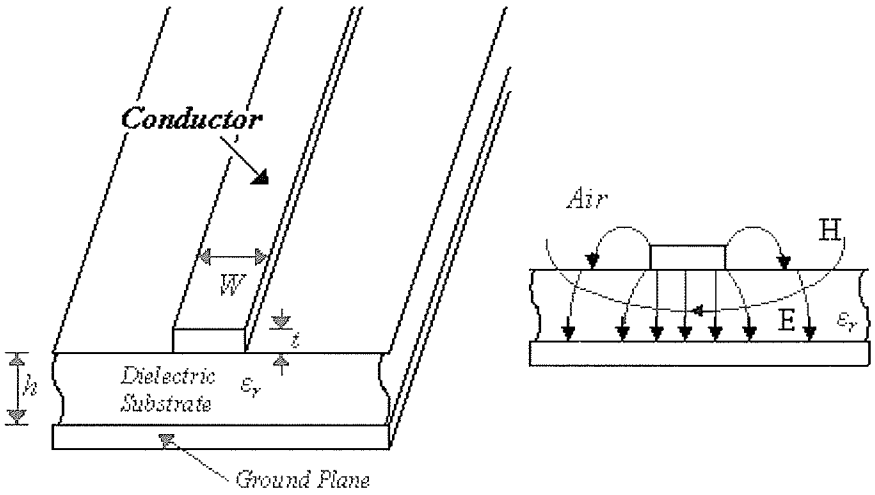

Figure 3.7: Microstrip Line [27]
a) Geometry b) Fields

This is shown below in equation (3.18) [27],

$$\varepsilon_{reff} = \frac{\varepsilon_r + 1}{2} + \frac{\varepsilon_r - 1}{2}\left(1 + \frac{10h}{w}\right)^{-0.555} \tag{3.18}$$

where h is the substrate height, and w is the line width.

This value may be used to calculate the wavelength in the guiding structure, λ_m, with respect to the free space wavelength, as shown in equation (3.19).

$$\lambda_m = \frac{\lambda_o}{\sqrt{\varepsilon_{reff}}} \tag{3.19}$$

The characteristic impedance of the slotline, Z_{om}, is dependent on the substrate's permittivity, ε_r, and height, h, and the microstrip line's width, w. For a microstrip line with a ratio of $w/h < 2$, the equation shown in (3.20) can be used to calculate the microstrip line's characteristic impedance [27].

$$Z_{om} = \frac{377}{2\pi\left(\frac{\varepsilon_r + 1}{2}\right)^{1/2}}\left[\ln\left(\frac{8h}{w}\right) + \frac{1}{8}\left(\frac{w}{2h}\right)^2 - \frac{1}{2}\frac{\varepsilon_r - 1}{\varepsilon_r + 1}\left\{\ln\frac{\pi}{2} + \frac{1}{\varepsilon_r}\ln\frac{4}{\pi}\right\}\right] \qquad (3.20)$$

3.3.3 Microstrip/Slotline Transition

This microstrip line is now placed on the backside of the dielectric substrate to function as a feed which couples energy into the slotline, as illustrated in Figure 3.8 a). To generate coupling the microstrip line crosses the slotline on the underside at a right angle. The portion of the slotline structure which overlays the microstrip line will serve as its ground plane. The microstrip line is extended a distance of $\lambda_m/4$ past the transition region and terminated in an open circuit; the slotline is also extended $\lambda_s/4$ and terminated in a short circuit. This creates the equivalent circuit shown in Figure 3.8 b) which promotes coupling between the two lines.

In this circuit, the microstrip line will see the total impedance as a series connection of the load impedance due to the slotline and the $\lambda_m/4$ open circuit stub. Consequently, the total impedance is simply the load impedance due to the slotline. At the transition, the

slotline impedance is a parallel connection of the $\lambda_s/4$ short circuit stub and the impedance of the slotline termination in a TSA. Consequently, the impedance of the slotline termination in a tapered slot antenna is the load seen by the microstrip line after a proper transformation.

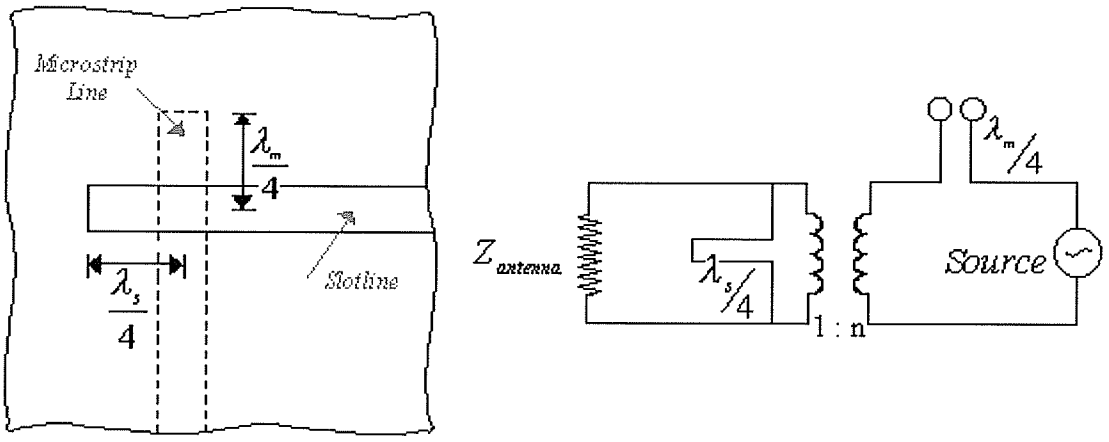

a) Geometry **b) Equivalent Circuit**

Figure 3.8: Microstrip/Slotline Transition
a) Geometry [29] b) Equivalent Circuit

Hence, the impedance of the microstrip line must be matched to the transformed impedance of the slotline to promote maximum coupling. This is a difficult task given the high impedance characteristics of the slotline. Y. H. Choung and W. C. Wong have established a set of equations to facilitate the design of the slotline and microstrip feed [29]. They are shown below in equation (3.21) through (3.25). In these equations, $Z_{om,\,os}$, represent the microstrip line's and slotline's characteristic impedances, respectively, $\lambda_{o,\,s}$ represent the

free space wavelength, and the slotline's wavelength, and h denotes the substrate's thickness. The variable n functions as a turns ratio between the two elements.

$$Z_{om} = n^2 Z_{os} \tag{3.21}$$

$$n = \cos\left(\frac{2\pi hu}{\lambda_o}\right) - \cot(q'_o)\sin\left(\frac{2\pi hu}{\lambda_o}\right) \tag{3.22}$$

$$q'_o = \frac{2\pi hu}{\lambda_o} + \left(\tan\left(\frac{u}{v}\right)\right)^{-1} \tag{3.23}$$

$$u = \sqrt{\varepsilon_r - (\lambda_o/\lambda_s)^2} \tag{3.23}$$

$$v = \sqrt{(\lambda_o/\lambda_s)^2 - 1} \tag{3.25}$$

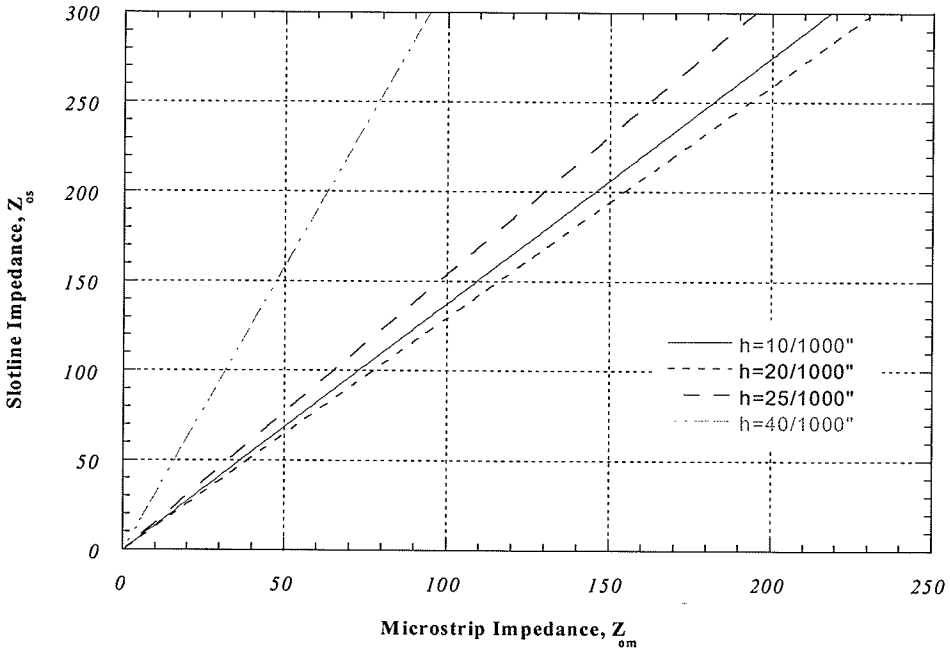

Figure 3.9: Slotline vs Microstrip Line Impedance

Figure 3.9 displays the linear relationship that is found between the characteristic impedance of the slotline and the microstrip line for various substrate heights, given $\lambda_o = 1cm$, $\lambda_s = 0.7cm$, and $\varepsilon_r = 3.38$.

3.4 Far Field Radiation Pattern of the Linear Tapered Slotline Antenna

The derivation of the far field LTSA pattern is accomplished by a first order approximation, using the fourier transform of the aperture field, *F(x)*, as shown in equation (3.26) [12].

$$E = \int F(x)\frac{e^{-jkR}}{R} \tag{3.26}$$

The LTSA is positioned along the *z* axes as shown in Figure 3.10. The length of the aperture is *W*, centered around the origin. *R* is taken as the reference point for the calculation and is the distance from the origin to the far field, $R \to \infty$. R' represents the distance from the antenna aperture to the far field.

For this antenna, the expression for the electric far field is shown in equation (3.27), where *C* is a constant and *F(x)* represents the aperture plane field.

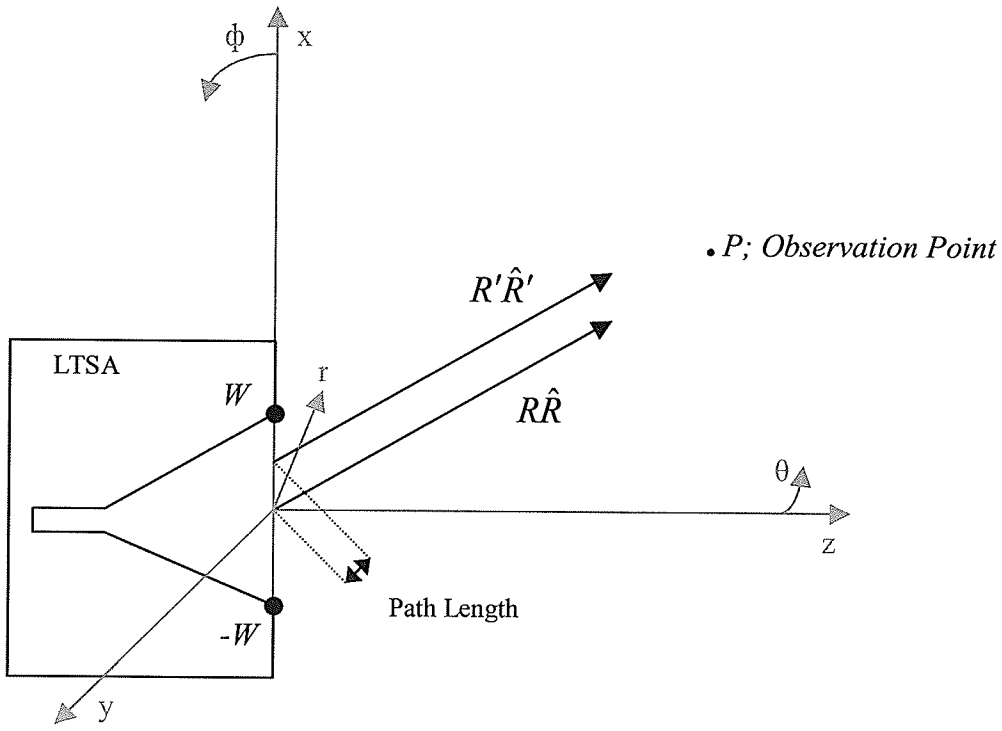

Figure 3.10: LTSA Far Field Calculation Geometry

$$E = C \int_{-W}^{W} F(x) \frac{e^{-jkR'}}{R'} dx \tag{3.27}$$

In the far field, the magnitudes of R' and R are approximately equal, and their accompanying unit vectors, $\hat{R}'$ and $\hat{R}$, are pointing in the same direction. However, the existing phase difference cannot be neglected. It can be accounted for as follows,

$$x\hat{x} + R'\hat{R}' = R\hat{R} \tag{3.28}$$

$$\therefore \qquad x(\hat{x}\cdot\hat{R}) + R'(\hat{R}\cdot\hat{R}) = R(\hat{R}\cdot\hat{R}) \tag{3.29}$$

By applying the dot product,

$$\hat{x}\cdot\hat{R} = \sin\theta \qquad and \qquad \hat{R}\cdot\hat{R} = 1 \tag{3.30}$$

Therefore,

$$R' = R - x\sin\theta \tag{3.31}$$

This expression for R', is substituted into equation (3.27),

$$E = C\int_{-W}^{W} F(x)\frac{e^{-jk(R-x\sin\theta)}}{(R-x\sin\theta)}dx \tag{3.32}$$

As $R \to \infty$, the expression $x\sin\theta$ becomes insignificant in the denominator and can be omitted from the equation. In order to further simplify the expression, it is noted that the exponential term $\frac{e^{-jkR}}{R}$ is a constant which can be absorbed by the existing constant, C.

$$E = C\int_{-W}^{W} F(x)e^{jkx\sin\theta}dx \tag{3.33}$$

The integral is now divided into two portions, where $x' = -x$, representing the portion of the antenna lying along the negative x axes.

$$E = C\left[\int_{-W}^{0} F(x')e^{jkx'\sin\theta}dx + \int_{0}^{W} F(x)e^{jkx\sin\theta}dx\right] \tag{3.34}$$

or,

$$E = C\left[-\int_{W}^{0} F(x')e^{-jkx\sin\theta}dx + \int_{0}^{W} F(x)e^{jkx\sin\theta}dx\right] \tag{3.35}$$

And by switching the limits of the first term, and enforcing the symmetry where $F(-x) = F(x)$, the equation takes the form,

$$E = C\left[\int_{0}^{W} F(x)e^{-jkx\sin\theta}dx + \int_{0}^{W} F(x)e^{jkx\sin\theta}dx\right] \tag{3.36}$$

The two integrals can be combined using Euler's identity, and the factor of *2* can be absorbed by the constant, *C*,

$$E = C\int_{0}^{W} F(x)\cos(kx\sin\theta)dx \tag{3.37}$$

Now that an expression for the far field has been derived, the aperture plane field, $F(x)$, must be found. Figure 3.11 depicts the geometry used for this derivation, where the dashed line represents the spherical wave front generated by the tapered slot antenna.

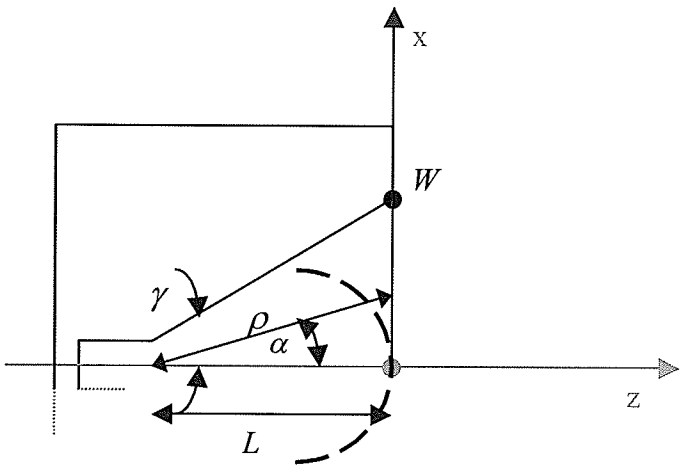

Figure 3.11: LTSA Aperture Plane Field Geometry

This expression is composed of both phase and amplitude components as shown in equation (3.38), where $\Psi(x)$ represents the phase distribution and *f(x)* represents the amplitude.

$$F(x) = f(x)e^{-jk\Psi(x)} \tag{3.38}$$

The phase component, $\Psi(x)$, must account for the phase lag at the edges, $\pm W$, of the structure due to the nature of the spherical wave front. The distance between the wavefront and the x axis is denoted as $\rho - L$. Consequently, $\Psi(x)$ can be expressed as,

$$\Psi(x) = \rho(x) - L \tag{3.39}$$

The distance ρ can be denoted in terms of α by equation (3.40).

$$\rho(x) = L / \cos(\alpha(x)) \tag{3.40}$$

Substituting this into equation (3.37), the phase component of the aperture plane field becomes,

$$\Psi(x) = \frac{L}{\cos(\alpha(x))} - L = L\left(\frac{1}{\cos(\alpha(x))} - 1\right) \tag{3.41}$$

The accompanying amplitude expression has been derived by Janaswamy et al, as shown in equation (3.41), where γ represents the taper angle [24].

$$f(x) = \frac{\cos(\alpha(x))}{\sqrt{\tan\left(\frac{\gamma}{2}\right)^2 - \tan\left(\frac{\alpha(x)}{2}\right)^2}} \qquad |\alpha| \le \gamma \tag{3.42}$$

Combining both the amplitude and phase, the final expression for the aperture field is,

$$F(x) = \frac{\cos(\alpha(x))}{\sqrt{\tan\left(\frac{\gamma}{2}\right)^2 - \tan\left(\frac{\alpha(x)}{2}\right)^2}} e^{-jkL\left(\frac{1}{\cos\alpha(x)} - 1\right)} \qquad |\alpha| \le \gamma \qquad (3.43)$$

This can now be introduced into the far field equation, (3.37), as shown below.

$$E = C\int_0^W \frac{\cos(\alpha(x))}{\sqrt{\tan\left(\frac{\gamma}{2}\right)^2 - \tan\left(\frac{\alpha(x)}{2}\right)^2}} e^{-jkL\left(\frac{1}{\cos\alpha(x)} - 1\right)} \cos(kx\sin\theta)dx \qquad |\alpha| \le \gamma$$

(3.44)

The distance x can be expressed as:

$$x = L\tan(\alpha(x)) \qquad (3.45)$$

And, by taking the derivative of x,

$$dx = L(\sec\alpha(x))^2 d\alpha(x) = \frac{L}{(\cos(\alpha(x)))^2} d\alpha(x) \qquad (3.46)$$

Substituting these values for x into equation (3.44) yields the final expression for the linear tapered slot antenna's electric far field,

$$E = C\int_0^{\gamma} \frac{\cos(\alpha(x))}{\sqrt{\tan\left(\frac{\gamma}{2}\right)^2 - \tan\left(\frac{\alpha(x)}{2}\right)^2}} \frac{\cos(kL\tan(\alpha(x))\sin(\theta))}{(\cos(\alpha(x)))^2} e^{-jkL\left(\frac{1}{\cos\alpha(x)} - 1\right)} d\alpha(x)$$

given, $|\alpha| \leq \gamma$ (3.47)

A matlab program was written to generate a plot of this electric field, the normalized far fields are shown below in Figure 3.12, for different taper angles and assuming $kL = 5\pi$.

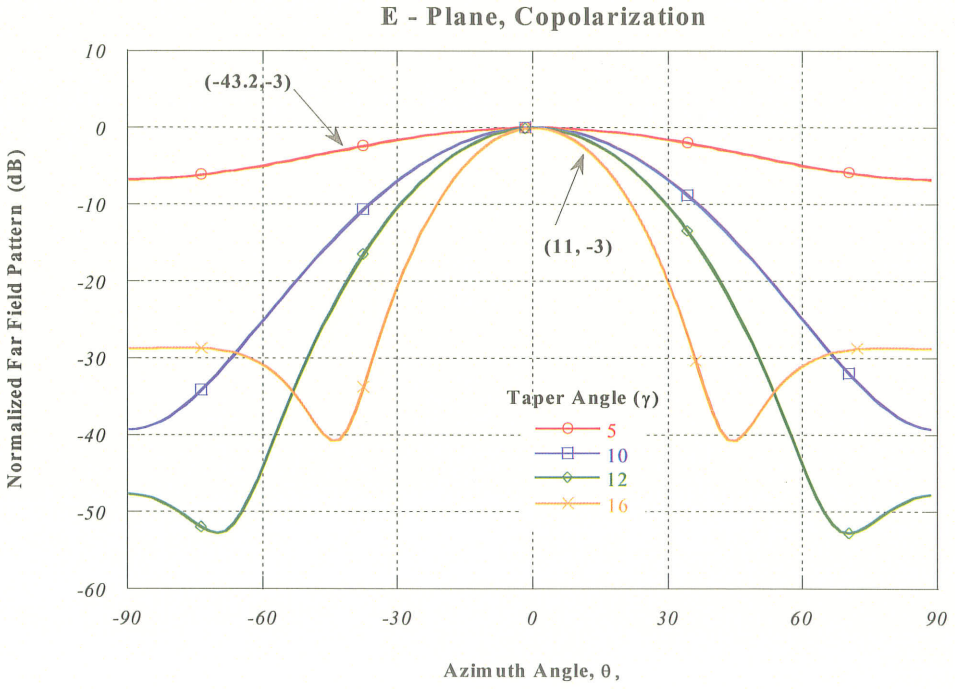

Figure 3.12: Linear Tapered Slotline Antenna Calculated Far Field Pattern

This graph demonstrates the *3 dB* beamwidth of the pattern decreasing as the tapered angle of the slot becomes larger. This beamwidth decreases from 86.4^o given a $\gamma = 5^o$ tapering angle to 22^o for the $\gamma = 16^o$.

3.5 Design Samples

Two linear tapered slotline antennas were designed, as shown in Figure 3.13, with a microstrip feed. The dimensions were calculated from LTSA design equations provided by Janaswamy. They are shown previously in equation (3.10) through (3.12).

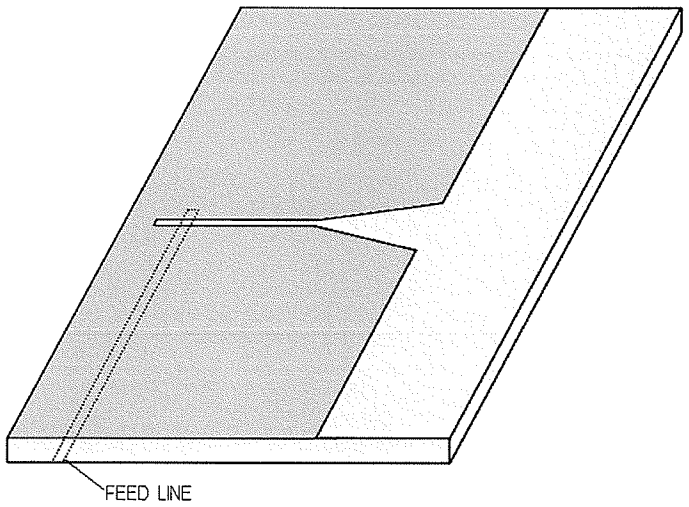

Figure 3.13: Linear Tapered Slotline Antenna

The substrate and operating frequency were chosen to accommodate the holographic antenna. This entailed an operating frequency of *30 GHz*, with an accompanying wavelength of $\lambda_o = 1\ cm$, and a Duroid 4003 substrate. Arbitrary aperture angles of 6^o and 15^o were chosen for the initial models. A table displaying both structures final dimensions is shown in Table 3.1.

Table 3.1: Dimensions of LTSAs at *30 GHz*, $2\gamma = 6^o$ and $2\gamma = 15^o$

Substrate: Duroid 4003	$\varepsilon_r = 3.38$	$t = 20mils$	$\sigma = 0.001$
Aperture Angle: $2\gamma = 6^o$	$2W = 0.52cm$	$2D = 6.096cm$	$L = 5cm$
Aperture Angle: $2\gamma = 15^o$	$2W = 1.466cm$	$2D = 6.096cm$	$L = 5cm$

The microstrip line - slotline transition was designed at a frequency of 30 GHz, on a Duroid 4003 substrate. For this frequency, a K-connector, with a characteristic impedance of 50Ω, is used to deliver power to the microstrip line. Therefore, for matching purposes, a microstrip line was designed with a characteristic impedance of 50Ω. The corresponding dimensions were calculated using the software Linecalc [30]. Following this, a short program was written in Mathematica to calculate the appropriate slotline impedance and width using the equations provided in (3.21) through (3.25) [31]. The slotline was terminated in an open rather than a short circuit, therefore, the stub length was adjusted to $\lambda_s/2$ to maintain the open circuit at the transition. These values were then adjusted slightly during the simulation process to achieve better matching characteristics. The dimensions of the microstrip - slotline transition are shown in Table 3.2.

Table 3.2: Dimensions of the Microstrip - Slotline Transition at *30GHz*

Substrate	$h = 20$ *mils*	$\varepsilon_r = 3.38$	$\varepsilon_{reff} = 2.672$	*metal thickness* $= .038$ *cm*
Microstrip Line	$Z_{om} = 50\Omega$	$w = 0.124$ *cm*	$\lambda_m = .61$ *cm*	$\lambda_m/4 = .15$ *cm*
Slotline	$Z_{os} = 118\Omega$	$w = .110$ *cm*	$\lambda_s = .7$ *cm*	$\lambda_s/2 = .35$ *cm*

These antennas were simulated using Ansoft HFSS and prototypes were built to confirm the accuracy of the simulated results [32]. The far field radiation patterns and return loss graphs, including both simulated and measured results, are shown in Figure 3.14 through 3.17, accompanied by Table 3.3 displaying the results.

The measured results are in good agreement with the simulated results displaying high sidelobes and significant pattern rippling. As expected, the *3 dB* beamwidth narrows from 30^o to 24^o as the taper angle increases from 6^o to 15^o. The return loss indicates better matching than that predicted by the simulated results.

Table 3.3: Measurement Results of LTSA Antennas

TSA Angle	Gain	3 dB Beamwidth	Return Loss	Bandwidth (GHz)
$2\gamma = 6^o$	6 dBi	30^o	-11.5 dB @ 29 GHz	28.5-29.5
$2\gamma = 15^o$	8 dBi	24^o	-12 dB @ 30 GHz	29.3-30.6

It should be noted that the Duroid 4003 substrate utilized does not fall within the substrate recommendation mentioned earlier in equation (3.13). Given a permittivity of $\varepsilon_r = 3.38$,

$$t_{eff} = 20mils(\sqrt{3.38} - 1) = 0.04\lambda_o \qquad (3.50)$$

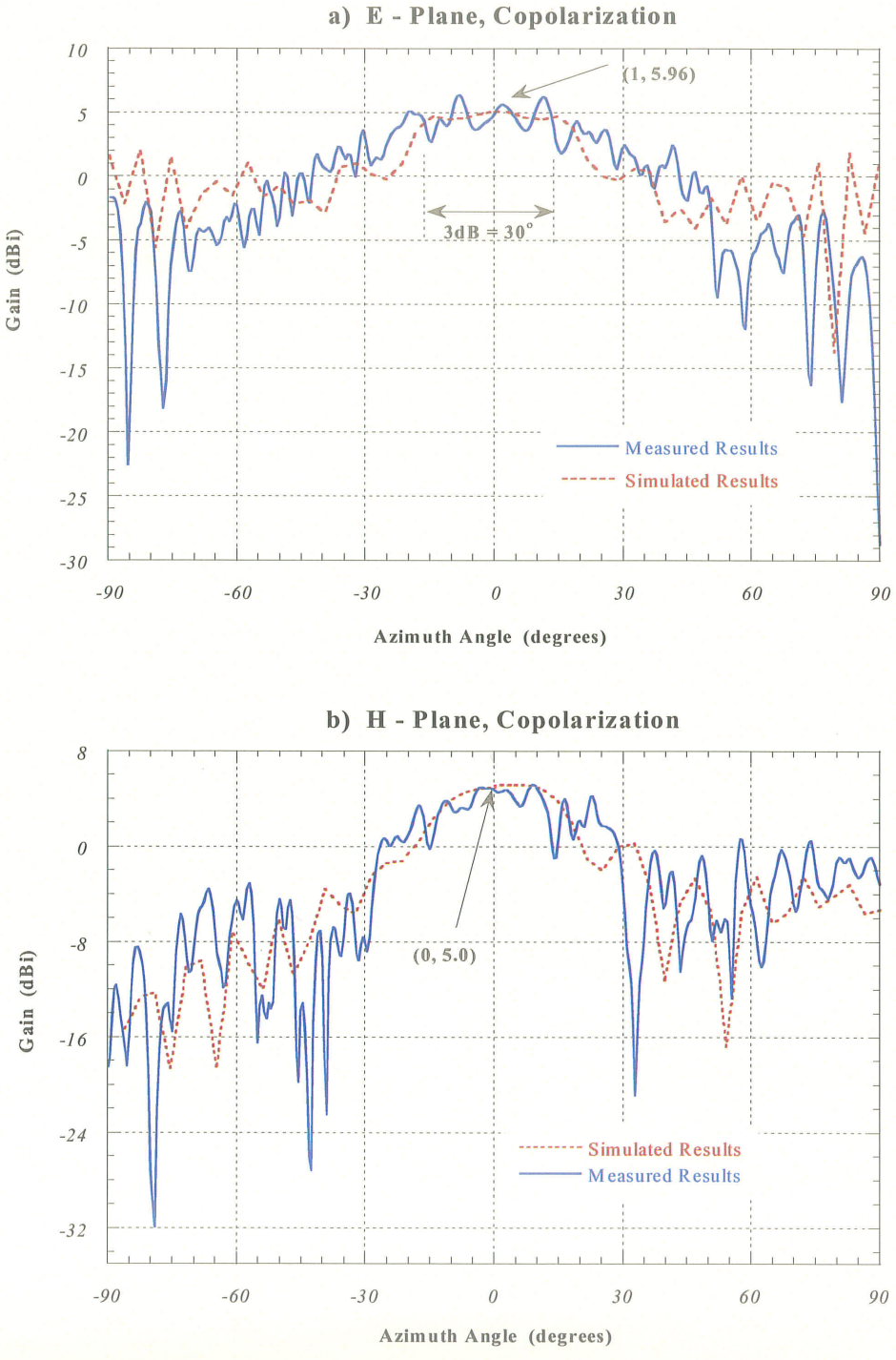

Figure 3.14: Measured and Simulated Results of an LTSA with a 6^0 Taper Angle a) E - Copolarization b) H - Copolarization

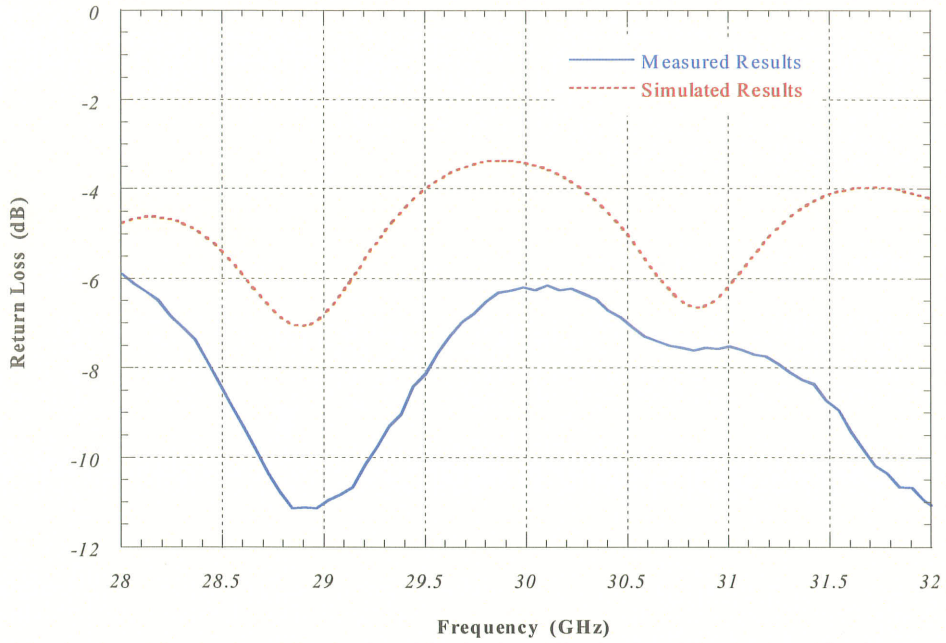

Figure 3.15: Measured and Simulated Return Loss Results of an LTSA with a 6^0 Taper Angle

This value is outside the recommend upper limit of $0.03\lambda_o$. This leads to degradation in the radiating beam and unwanted substrate modes which may cause the high sidelobes and pattern rippling. In addition, radiation from the microstrip feedline and scattering from the antenna's edges can contribute to these higher sidelobes and pattern interference.

Furthermore, a microstrip line and slotline were built on the Duroid 4003 substrate to assess the losses incurred in these lines at *30 GHz*. Measurements indicate a loss of 0.2992 *dB/cm* exist in the microstrip line, and 0.592 *dB/cm* of loss in the slotline. For the relevant structures, this amounts to *0.93 dB* of loss in the microstrip line and *1.18 dB* of

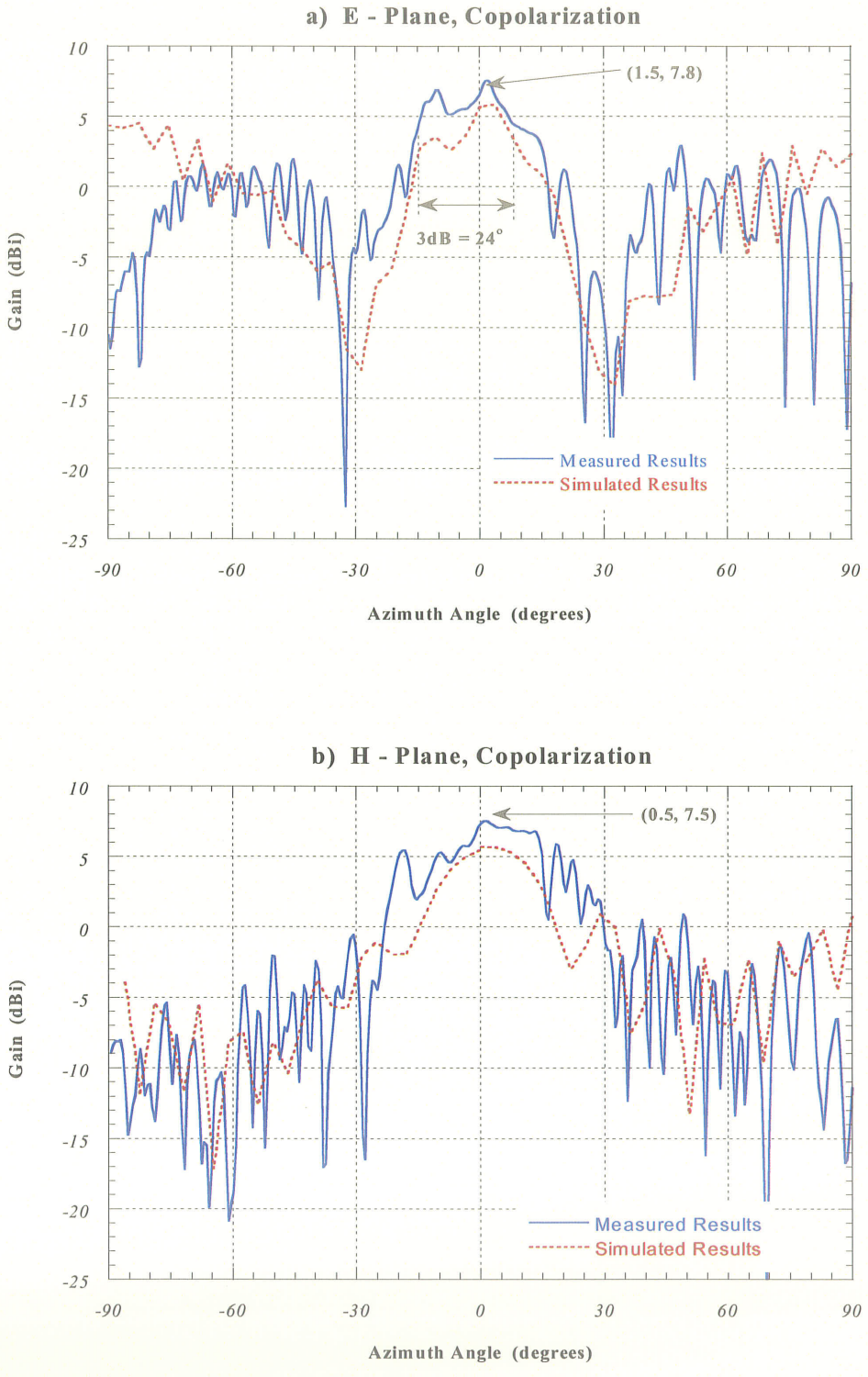

Figure 3.16: Measured and Simulated Results of an LTSA with a 15° Taper Angle a) E - Copolarization b) H - Copolarization

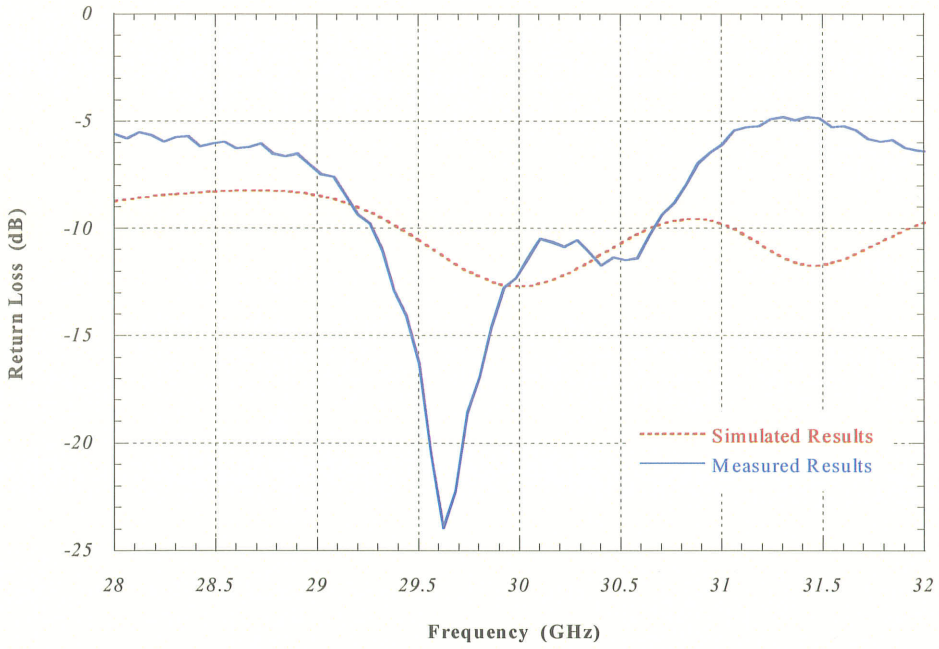

Figure 3.17: Measured and Simulated Return Loss Results of an LTSA with a 15^{o} Taper Angle

loss in the slotline. Therefore, given a more efficient feed to excite a shorter slotline, the gain of the LTSA can be improved.

3.6 Conclusion

The tapered slotline antenna is a low profile antenna which radiates in an end-fire direction while producing symmetrical radiation patterns in the E and H planes. Single element gain between *12* and *20 dBi* has been achieved with a large operational bandwidth. This slow wave structure may be fed by a microstrip line which couples energy into the slot-

line. Published literature provides guidelines to design both the TSA and feedlines. A first order approximation of the radiated far field pattern demonstrates controllable beam-widths achieved by varying the taper angle of the structure.

Two linear tapered slotline antennas were designed using Ansoft HFSS and tested to determine the accuracy of the software and the potential of the LTSA as a holographic antenna feed. The software proved dependable as the simulated and measured results were analogous. The radiation pattern displayed high sidelobes and rippling. This is attributed to spurious radiation from the feedline and scattering from the antenna edges. In addition, the substrate chosen to accommodate the holographic antenna is outside the practicable thickness range, leading to undesirable substrate modes which can degrade the gain of the LTSA and cause pattern rippling. The feedline and slotline are also a source of gain loss at the operating frequency.

The planar profile of the linear tapered slotline antenna complemented by its controllable beamwidths promotes this antenna as a viable holographic antenna feed. The hologram may be etched onto the same substrate as the LTSA providing for a single unit antenna while eliminating alignment errors. As such, the hologram could be situated at the phase center of the LTSA allowing its spherical wave to illuminate the hologram.

In order to generate optimal holographic antenna performance, the feed pattern must be properly selected. An efficient feed would illuminate the hologram uniformly, and generate minimal spillover losses. To ascertain the most efficient feed option, a formulation of

the holographic antenna's efficiency has been derived to serve as a design aid when determining feed patterns.

Chapter 4: Holographic Antenna Efficiency

4.1 Introduction

The efficiency of an antenna is determined to assess the losses impacting the overall performance of an antenna. By quantifying the various losses incurred in the system, insight is given into the potential of the design and the influence of particular antenna parameters on its capabilities. This efficiency formulation facilitates the design process by providing a direct correlation between antenna parameters and antenna performance. As such, a systematic approach may be taken to optimize the performance of the antenna.

A holographic antenna consists of a feed which illuminates a secondary aperture, similar to reflector and lens antennas. For a holographic antenna, the secondary aperture is a hologram which performs a beam forming function. When the feed and the hologram are non-coplanar, the approach for feed efficiency determination, as given by Silver, may be applied [33]. However, for the coplanar case, investigated in this thesis, the direct application is not possible, as the equivalent aperture dimension which intercepts the feed power is not evident.

In this chapter, the technique to overcome this difficulty is presented. The holographic antenna's efficiency is then formulated to determine the holographic antenna dimensions

and feed selection that generate optimal antenna performance. The total efficiency comprises the three main sources of loss, namely, the spillover, amplitude taper of aperture distribution, and termination efficiencies.

4.2 Antenna Efficiency

The efficiency of an antenna can be calculated from the general equation for the gain of the antenna, shown in equation (4.1) [12]. It displays the directional capabilities of the antenna as well as its efficiency,

$$G = \frac{4\pi U_{max}}{P_{in}} = \frac{4\pi U_{max}}{P_{rad}} \cdot \frac{P_{rad}}{P_{in}} \tag{4.1}$$

where G is the gain, U_{max} is the maximum radiation intensity, P_{rad} is the antenna radiated power, and P_{in} is the total input power to the antenna. By factoring out the directivity, D, from equation (4.1), we are left with the antenna efficiency, η,

$$G = \eta \times D \tag{4.2}$$

In general, antenna efficiency is dependent on mismatch, conduction, and dielectric losses [12]. However, other sources of loss may also be present which are specific for each type

of antenna under investigation. The main sources of loss in a holographic antenna can be identified by examining the antenna configuration shown in Figure 4.1.

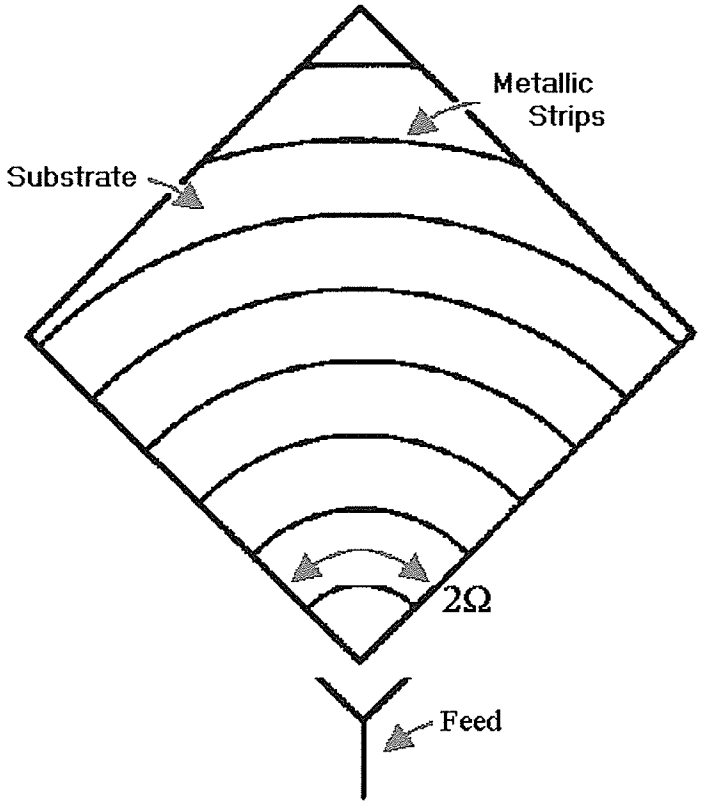

Figure 4.1: Holographic Antenna with Feed

Firstly, loss is incurred if the total feed radiated power is not completely confined to the hologram. Feed energy that is radiated outside of the subtended angle, 2Ω, of the holographic antenna cannot contribute to exciting the antenna and therefore represents loss in the system. This results in loss as the energy transmitted through to the hologram is only a portion of the total power emitted by the feed. This efficiency is termed the spillover efficiency and is denoted as η_{spill}.

Secondly, in order to achieve the maximum directivity from a given aperture antenna, it is necessary that the antenna is illuminated uniformly by the feed. Any tapering of the amplitude along the holographic aperture will result in a reduction in antenna gain which is reflected by a decrease of antenna efficiency. This loss, due to tapering of the feed beam pattern, is termed the taper efficiency and is denoted as η_{taper}.

Lastly, any residual power at the terminal length of a holographic antenna represents loss, since it indicates the power that has not been scattered by the hologram. This efficiency is dependent mainly on the rate of radiation of the hologram. It is termed the termination efficiency and is denoted as η_{term}.

The total efficiency of the holographic antenna is a product of these efficiencies, as shown below. Various efficiencies affecting the gain of a holographic antenna can be readily identified by rewriting equation (4.1) as,

$$G = \left(4\pi \frac{U_{max,\,uniform}}{P_{rad}}\right)\left(\frac{P_{intercepted}}{P_{feed}}\right)\left(\frac{U_{max}}{U_{max,\,uniform}}\right)\left(\frac{P_{rad}}{P_{intercepted}}\right)\left(\frac{P_{feed}}{P_{input}}\right) \quad (4.3)$$

where,

$U_{max,\,uniform} \equiv$ *maximum radiation intensity from a uniform aperture distribution as determined under the condition of equal* P_{rad}

$P_{intercepted} \equiv$ *feed power intercepted by the aperture*

$P_{feed} \equiv$ *total power radiated by the feed*

$U_{max} \equiv$ *maximum radiation intensity from the actual aperture distribution*

$P_{rad} \equiv$ *power radiated by the holographic antenna*

$P_{input} \equiv$ *total input power to the feed*

It is clear that the first term is the maximum directivity, D, from the given aperture $\left(D = 4\pi\frac{A}{\lambda^2};\ A \equiv aperture\ \ area\right)$. All other terms are related to efficiencies, hence equation (4.3) can be written in the following form,

$$G = D \times \eta_{spill} \times \eta_{taper} \times \eta_{termination} \times \eta_{feed} \tag{4.4}$$

The total efficiency, η, can be written as,

$$\eta = \eta_{spill} \times \eta_{taper} \times \eta_{termination} \times \eta_{feed} \tag{4.5}$$

It should be noted that the feed efficiency, η_{feed}, is included to represent any losses in the feed. For an open waveguide or a horn feed η_{feed} is very close to *100%* [34]. For other

types of feeds, such as the printed type, as considered here, η_{feed} can noticeably degrade the achievable efficiency.

In the following section the problem is outlined and detailed derivations of these efficiencies are presented.

4.3 Efficiency Derivation

4.3.1 Problem Formulation

For a holographic antenna, where the feed and the hologram are coplanar, it is necessary to first identify the intercepting area of the hologram with respect to the feed. By postulating that the holographic antenna occupies a cone, as displayed in Figure 4.2, the total power radiated by a holographic antenna is relative to the power of the feed over a spherical surface, A. This represents the feed power intercepted by the holographic antenna, which will be rescattered by the hologram.

The verification can be done by applying the Poynting theorem to the conic volume V_o, enclosed by the front spherical surface, *A,* the end spherical surface, *B*, and the conical surface, *C*. It should be noted that the dimension of the conic section is chosen sufficiently large enough to encompass the hologram.

It is known that in a source free region [35],

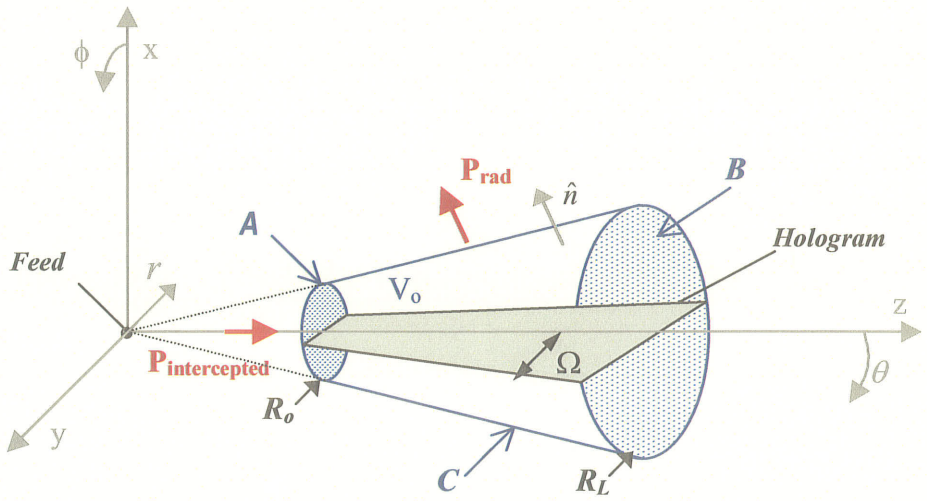

Figure 4.2: Configuration of a Holographic Antenna Occupying a Cone

$$Re \oint_{A+B+C} (\bar{E}_t \times \bar{H}_t^*) \cdot \hat{n} ds = 0 \tag{4.6}$$

where, $Re(\ )$ represents the real component, and,

$$\bar{E}_t = \bar{E}_{feed} + \bar{E}_{hol} \tag{4.7a}$$

$$\bar{H}_t = \bar{H}_{feed} + \bar{H}_{hol} \tag{4.7b}$$

the subscripts *feed* and *hol* denote the fields emanating from the feed or holographic antenna, and $\hat{n}$ represents the orthogonal unit vector pointing outward from the volume V_o.

Simplifying equation (4.6) gives,

$$Re \oint_{A+B+C} (\bar{E}_{feed} \times \bar{H}_{feed}^{*}) \cdot \hat{n} ds + Re \oint_{A+B+C} (\bar{E}_{hol} \times \bar{H}_{hol}^{*}) \cdot \hat{n} ds + \ldots$$

$$Re \oint_{A+B+C} (\bar{E}_{feed} \times \bar{H}_{hol}^{*} + \bar{E}_{hol} \times \bar{H}_{feed}^{*}) \cdot \hat{n} ds = 0 \qquad (4.8)$$

and the last term of the left hand side will vanish, following the alternative form of the reciprocity theorem (Appendix A).

For a holographic antenna radiating in a direction significantly askance of endfire, the fields on the surfaces A and B are mainly from the feed, thus implying that $Re \int_A (\bar{E}_{hol} \times \bar{H}_{hol}^{*}) \cdot \hat{n} ds + Re \int_B (\bar{E}_{hol} \times \bar{H}_{hol}^{*}) \cdot \hat{n} ds$ is negligible with respect to $Re \int_A (\bar{E}_{feed} \times \bar{H}_{feed}^{*}) \cdot \hat{n} ds + Re \int_B (\bar{E}_{feed} \times \bar{H}_{feed}^{*}) \cdot \hat{n} ds$. Since the feed power does not traverse the surface C,

$$Re \int_C (\bar{E}_{feed} \times \bar{H}_{feed}^{*}) \cdot \hat{n} ds = 0 \qquad (4.9)$$

Hence, equation (4.8) can be reduced to,

$$Re\int_A(\bar{E}_{feed}\times\bar{H}_{feed}^{*})\cdot\hat{n}_{in}ds = Re\int_B(\bar{E}_{feed}\times\bar{H}_{feed}^{*})\cdot\hat{n}ds + Re\int_C(\bar{E}_{hol}\times\bar{H}_{hol}^{*})\cdot\hat{n}ds \tag{4.10}$$

where $\hat{n}_{in} = -\hat{n}$.

Equation (4.10) indicates that the feed power intercepted by A is equal to the power radiated by the holographic antenna plus the residual power of the feed at the terminal length, R_L, of the hologram. This derivation establishes that the area A represents the intercepting area of the hologram to the feed.

In the following analysis the subtended angle of the area A will be utilized. The analysis will be done by assuming an ideal feed with a circularly symmetric pattern as depicted by Silver, as shown in equation (4.11) [33].

$$\begin{aligned} G_{feed}(\theta) &= 2(n+1)(\cos\theta)^n && |\theta| \le \frac{\pi}{2} \\ G_{feed}(\theta) &= 0 && |\theta| > \frac{\pi}{2} \end{aligned} \tag{4.11}$$

Many actual feeds may be approximately represented by equation (4.11) over a significant portion of the main lobe.

The electric field expression for the field pattern, E_{feed}, is related to gain through the radiation intensity, U_{feed},

$$G_{feed} \propto U_{feed} \propto r^2 |E_{feed}|^2 \tag{4.12}$$

therefore, the electric field is,

$$|E_{feed}| \propto \sqrt{2(n+1)}(\cos\theta)^{n/2} \tag{4.13}$$

The normalized feed gain patterns for differing n values are shown in Figure 4.3.

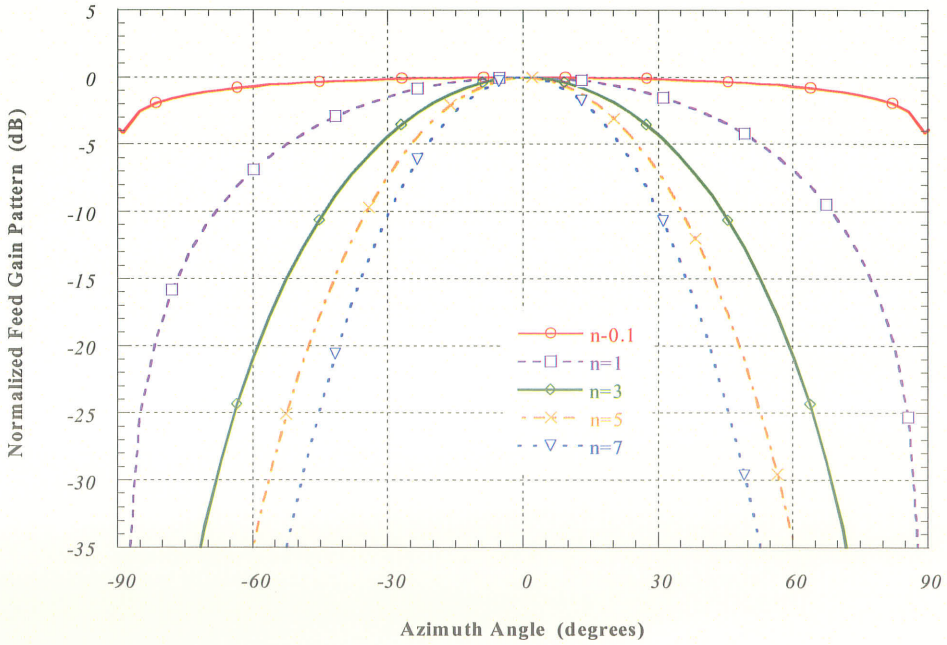

Figure 4.3: Normalized Feed Gain Patterns for Efficiency Derivation

The conal configuration and the expression representing the feed pattern, equation (4.11), are now used to derive expressions for the aforementioned efficiencies.

4.3.2 Spillover Efficiency

The spillover efficiency, η_{spill}, represents losses in feed power which 'spill over' the sides of the holographic antenna, therefore, not contributing to exciting the antenna. As derived in section 4.2, the spillover efficiency is a ratio of the feed power intercepted by a conical surface A, $P_{intercepted}$, to the total radiated feed power, P_{feed}. Mathematically, it is expressed as,

$$\eta_{spill} = \frac{P_{intercepted}}{P_{feed}} \tag{4.14}$$

Using the ideal feed as defined by equation (4.11), equation (4.14) can be reduced to,

$$\eta_{spill} = \frac{\int_0^{2\pi}\int_0^{\Omega} 2(n+1)(\cos\theta)^n \sin\theta d\theta d\phi}{\int_0^{2\pi}\int_0^{\pi/2} 2(n+1)(\cos\theta)^n \sin\theta d\theta d\phi} \tag{4.15}$$

By evaluating both of the integrals, the final expression for the spillover efficiency is,

$$\eta_{spill} = 1-(\cos\Omega)^{n+1} \tag{4.16}$$

4.3.3 Taper Efficiency

The taper efficiency, η_{taper}, is a measure of the uniformity of the amplitude distribution over the aperture of the antenna. As demonstrated in section 4.2, the taper efficiency is expressed as a ratio of the maximum radiation intensity, U_{max}, emitted by the antenna when it is illuminated by the feed, to the maximum possible radiation intensity, $U_{max,\,uniform}$, for the same antenna with a uniform aperture distribution.

$$\eta_{taper} = \frac{U_{max}}{U_{max,\,uniform}} \tag{4.17}$$

since $U(\theta, \phi) = \frac{r^2}{2\eta_o}|E(\theta, \phi)|^2$, and η_o is the intrinsic impedance of free space,

$$\eta_{taper} = \frac{U_{max}}{U_{max,\,uniform}} = \frac{|E_{max}|^2}{|E_{max,\,uniform}|^2} \tag{4.18}$$

The terms E_{max} and $E_{max,\,uniform}$ designate the maximum radiated electric fields of a hologram illuminated by an ideal feed as defined in equation (4.11), and of the same hologram with uniform aperture distribution, respectively. They can be determined from the fourier transform of the aperture electric field distributions.

By expressing the aperture electric fields, E_{ap}, and $E_{ap,\,uniform}$, in terms of their amplitudes as,

$$E_{ap}(\theta, r) = af(\theta, r) \tag{4.19a}$$

and,

$$E_{ap,\,uniform} = a_{uniform} \tag{4.19b}$$

η_{taper} in equation (4.18) is reduced to,

$$\eta_{taper} = \left|\frac{a}{a_{uniform}}\right|^2 \frac{\left|\int_{A_{ap}} f(\theta, r)dA\right|^2}{A_{ap}^2} \tag{4.20}$$

The ratio a to $a_{uniform}$ is evaluated from the condition that the fields E_{max} and $E_{max,\,uniform}$ are determined under the condition of equal power radiated from the aperture, which is given by,

$$P_{rad} = P_{max,\,uniform} \tag{4.21}$$

As the power radiated by an aperture is equal to the power flow across the aperture, it is found that,

$$\left|\frac{a}{a_{uniform}}\right|^2 = \frac{A_{ap}}{\int\limits_{A_{ap}} |f(\theta, r)|^2 dA} \tag{4.22}$$

The equation for taper efficiency, (4.17), then becomes,

$$\eta_{taper} = \frac{1}{A_{ap}} \frac{\left| \int\limits_{A_{ap}} f(\theta, r) \cos\theta dA \right|^2}{\int\limits_{A_{ap}} |f(\theta, r)|^2 dA} \tag{4.23}$$

The numerator represents the power as generated by the copolar components of the antenna, and the denominator represents the total power from both copolar and crosspolar components. The copolar and crosspolar field components are shown below in Figure 4.4,

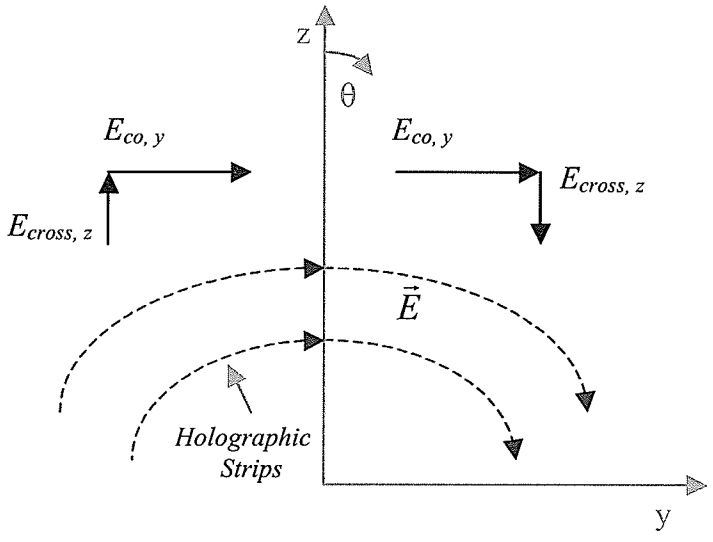

Figure 4.4: Copolar and Crosspolar Electric Field Components of Feed Pattern

where,

$$|E_{co,y}| = |E|\cos\theta \tag{4.24a}$$

and,

$$|E_{cross,z}| = |E|\sin\theta \tag{4.24b}$$

For a sectoraly shaped hologram, in Figure 4.5, it can be shown that $f(\theta, r)$ represents the hologram aperture distribution which is proportional to the field pattern of the feed. The expression $f(\theta, r)$ can be written as,

$$f(\theta, r) = k(\cos\theta)^{n/2} e^{-\alpha r} \tag{4.25}$$

where k is the proportionality constant. This constant does not have to be explicitly determined since it does not contribute to the η_{taper} calculation. The factor $e^{-\alpha r}$ is included to account for the attenuation due to radiation leakage along the hologram.

Substituting equation (4.25) into (4.23), the taper efficiency, can be further reduced.

$$\eta_{taper} = \frac{1}{\Omega(R_L^2 - R_o^2)} \frac{\left| \int_{-\Omega}^{\Omega} (\cos\theta)^{n/2+1} d\theta \right|^2 \cdot \left| \int_{R_o}^{R_L} e^{-\alpha(r-R_o)} r dr \right|^2}{\int_{-\Omega}^{\Omega} (\cos\theta)^n d\theta \cdot \int_{R_o}^{R_L} e^{-2\alpha(r-R_o)} r dr} \tag{4.26}$$

An integration by parts may be performed to further simplify this equation.

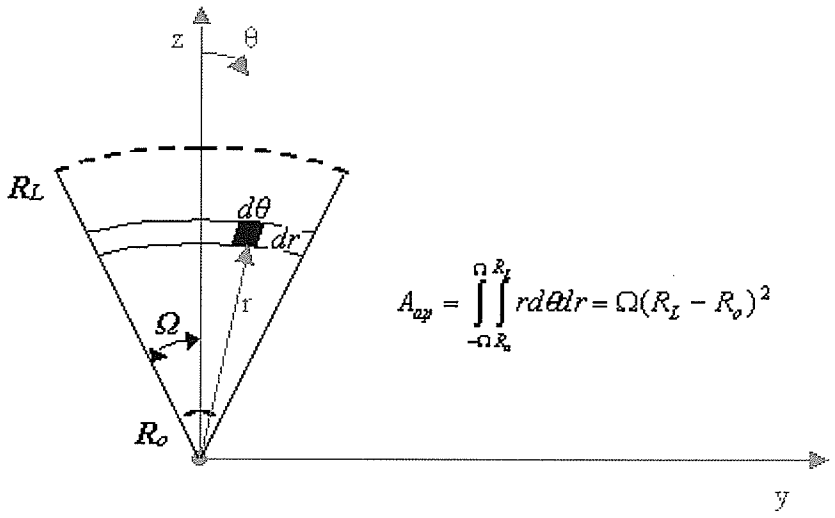

Figure 4.5: Sectoral Shaped Holographic Antenna Area

4.3.4 Termination Efficiency

The termination efficiency, η_{term}, accounts for loss incurred by the power which is not scattered by the hologram and is remnant at the length of the antenna, as given in section 4.2. It is expressed as a ratio of the power radiated by the holographic antenna, P_{rad}, to the power intercepted by the cone containing the hologram, $P_{intercepted}$, as shown in equation (4.27).

$$\eta_{term} = \frac{P_{rad}}{P_{intercepted}} \tag{4.27}$$

For a sectoral hologram, the determination of equation (4.27) is straight forward. However, the treatment of a diamond shaped hologram is more cumbersome and is presented here.

The termination efficiency is calculated in two parts. The diamond shaped antenna is divided into two sections, as demonstrated in Figure 4.6. The first section is the conical area between the conducting strips at R_o and R_1. This conical portion represents the area which is directly excited by the feed. The power delivered to this section is denoted as $P_{intercepted}$, and the power leaving this region is termed P_{out1}. The second portion of the antenna is defined between the conducting strips at R_1 and R_L. The power into this area is P_{out1} and the power exiting this division is P_{out2}.

An equation is now derived to calculate the ratio of power radiated by the holographic antenna, P_{rad}, to the power fed into the conal structure, P_{in}. This equation is then arranged to explicitly show the radiated powers in the two aforementioned sections of the antenna.

$$P_{rad} = P_{intercepted} - P_{out2} \tag{4.28}$$

Or, it can be written as,

$$P_{rad} = (P_{intercepted} - P_{out1}) + (P_{out1} - P_{out2}) \tag{4.29}$$

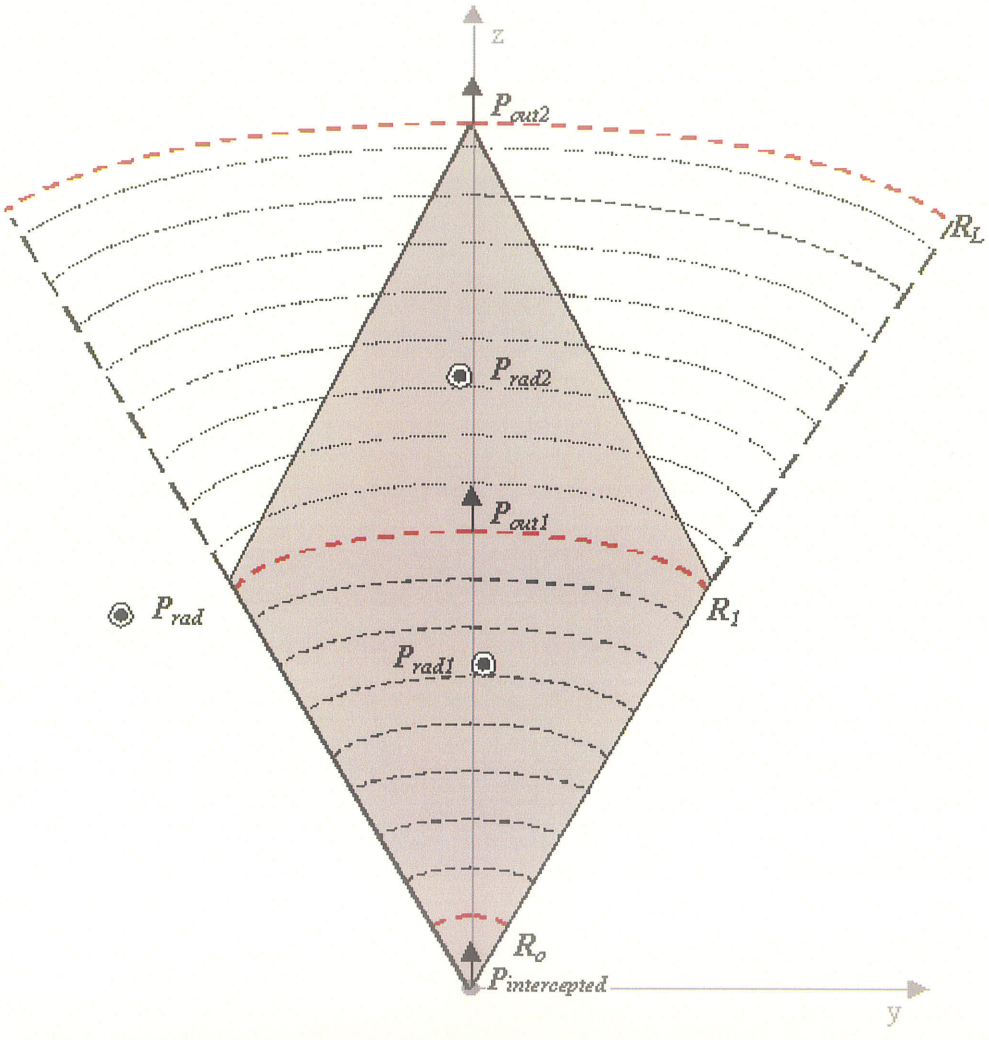

Figure 4.6: Holographic Antenna Geometry for Termination Efficiency Calculation

The two terms on the right side of equation (4.29) represent the power radiated by the two previously defined sections of the antenna; $P_{intercepted} - P_{out1} = P_{rad1}$ and $P_{out1} - P_{out2} = P_{rad2}$. Equation (4.29) can be rearranged as,

$$P_{rad} = P_{intercepted}\left(1 - \frac{P_{out1}}{P_{intercepted}}\right) + P_{out1}\left(1 - \frac{P_{out2}}{P_{out1}}\right) = P_{rad1} + P_{rad2} \quad (4.30)$$

which is reduced to,

$$\frac{P_{rad}}{P_{intercepted}} = \left(1 - \frac{P_{out1}}{P_{intercepted}}\right) + \frac{P_{out1}}{P_{intercepted}}\left(1 - \frac{P_{out2}}{P_{out1}}\right) = \frac{P_{rad1}}{P_{intercepted}} + \frac{P_{rad2}}{P_{intercepted}} \quad (4.31)$$

The first part of the calculation involves the first portion of the holographic antenna, and the term $\frac{P_{out1}}{P_{intercepted}}$ is determined. By including $e^{-2\alpha r}$ to account for radiation losses from the structure, it can be shown that,

$$P_{intercepted} = e^{-2\alpha R_o} 2\pi \int_{-\Omega}^{\Omega} (\cos\theta)^n d\cos\theta \quad (4.32)$$

$$P_{out1} = e^{-2\alpha R_1} 2\pi \int_{-\Omega}^{\Omega} (\cos\theta)^n d\cos\theta \quad (4.33)$$

which gives,

$$\frac{P_{out1}}{P_{intercepted}} = e^{-2\alpha(R_1 - R_o)} \tag{4.34}$$

Therefore,

$$\frac{P_{rad1}}{P_{intercepted}} = 1 - e^{-2\alpha(R_1 - R_o)} \tag{4.35}$$

For the second portion of the hologram, it is evident that the radiated power is a function of r. By determining the radiated power over an incremental length, Δr, the total radiated power can be expressed in integral form as,

$$\frac{P_{rad2}}{P_{intercepted}} = e^{-2\alpha(R_1 - R_o)_1} \frac{\int_{R_1}^{R_L} \int_{0}^{\theta(r)} e^{-2\alpha(r - R_1)} |f(\theta)|^2 d2\alpha r}{\int_{0}^{\Omega} |f(\theta)|^2 \sin\theta d\theta} \tag{4.36}$$

Further detail is provided in Appendix B. Returning to equation (4.31), the termination efficiency is written as, where the expression $f(\theta)$ is replaced by equation (4.11), and,

$$\frac{P_{rad}}{P_{intercepted}} = (1 - e^{-2\alpha(R_1 - R_o)}) + e^{-2\alpha(R_1 - R_o)} \cdot \frac{\int_{R_1}^{R_L} \left|1 - \cos(\theta(r))^{n+1}\right| e^{-2\alpha(r - R_1)} d2\alpha r}{(1 - \cos(\Omega)^{n+1})} \tag{4.37}$$

where $\theta(r) = \sin\left(\left(\frac{R_1}{r}\sin(2\Omega)\right) - \Omega\right)$.

4.4 Generation of Design Curves

The mathematical expressions that have been derived for the various efficiencies, η_{spill}, η_{taper}, and η_{term}, have been plotted to display their influence on the overall antenna efficiency. This provides a graphical relationship between holographic antenna size, feed pattern, and antenna efficiency, which may be used as a tool during the holographic antenna design process.

Matlab code was generated in order to plot the mathematical expressions for the efficiencies, given various feed patterns, versus the subtended angle of the holographic antenna [11]. Figure 4.7 displays these efficiencies for a diamond shaped *10 cm* by *10 cm* holographic antenna. In all cases, a predetermined holographic antenna rate radiation of $\alpha d = 0.01$, where d is the element spacing, was used to account for attenuation of the

wave propagating along the hologram. The varied n values denotes the value used in the expression for the feed pattern shown in equation (4.11) ($G_{feed}(\theta) = 2(n+1)(\cos\theta)^n$).

The spillover efficiency, Figure 4.7 a), is very low when the hologram is narrow and increases to a value of *100%* with a subtended holographic antenna angle of 180^o as the hologram completely intercepts the feed power. This efficiency is dependent on the sub-tended angle of the hologram and feed pattern, however, is independent of hologram size.

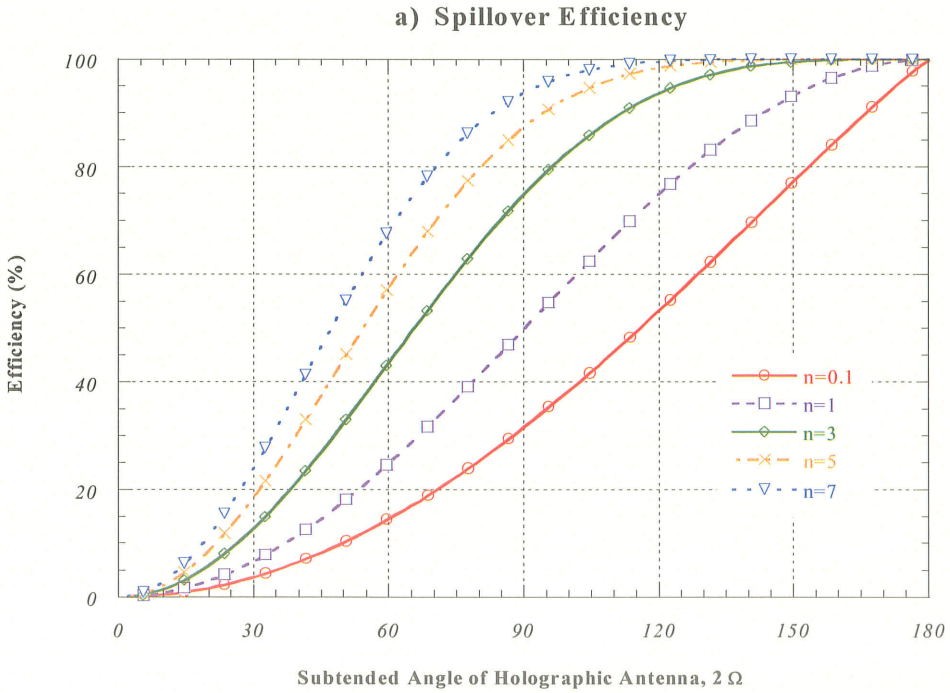

Figure 4.7: Efficiencies for a *10 cm* by *10 cm* Diamond Shaped Holographic Antenna a) Spillover Efficiency b) Taper Efficiency c) Termination Efficiency

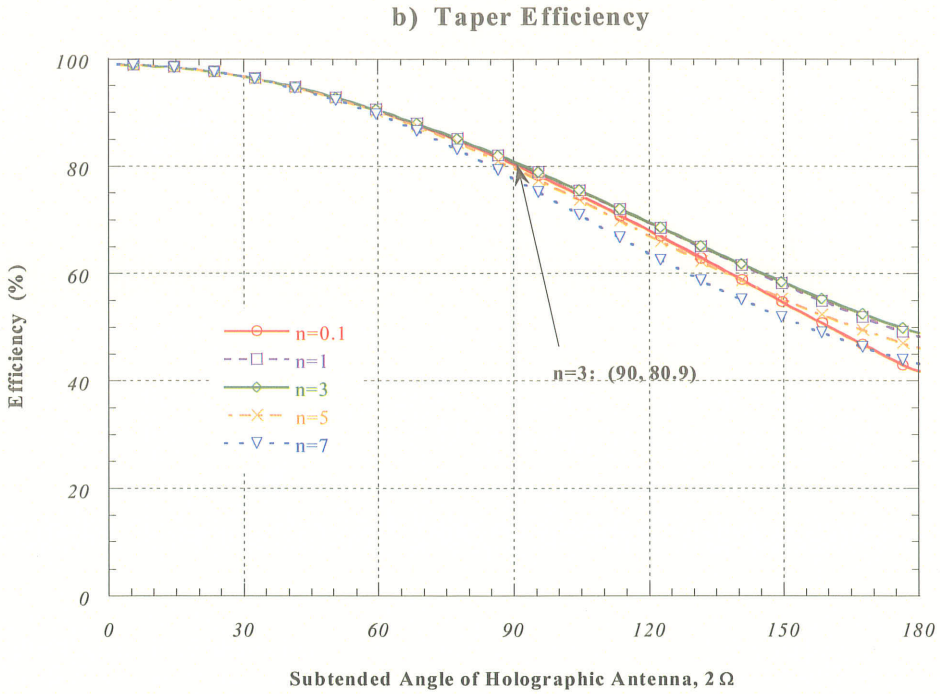

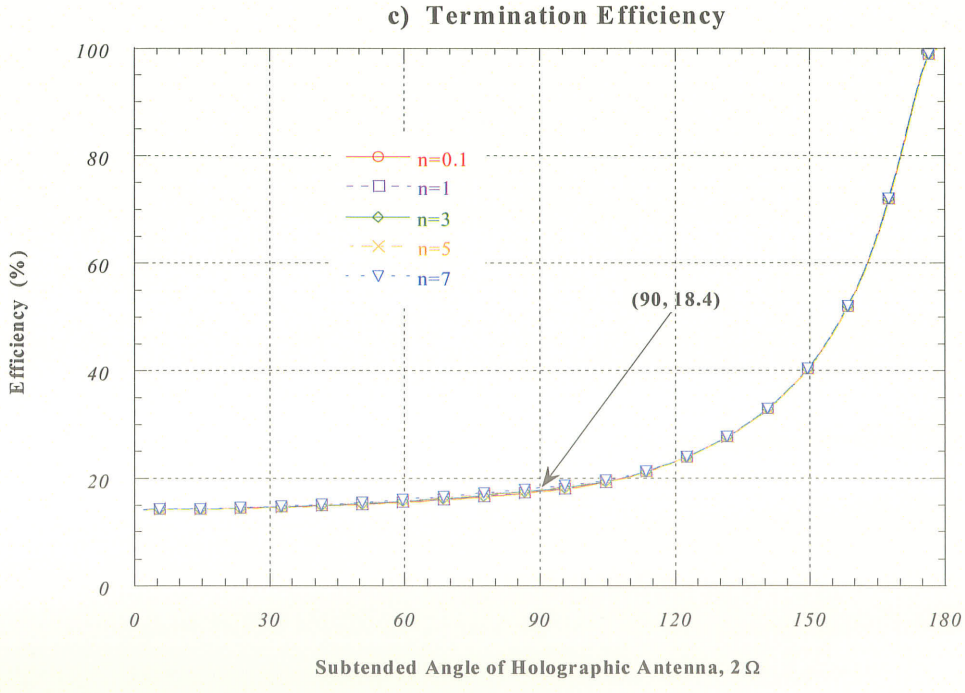

Figure 4.7 (continued): Efficiencies for a *10 cm* by *10 cm* Diamond Shaped Holographic Antenna a) Spillover Efficiency b) Taper Efficiency c) Termination Efficiency

The taper efficiency, Figure 4.7 b), approaches *100%* when the hologram is very narrow. This value does not reach *100%* as tapering of the amplitude exits along the length of antenna. Amplitude tapering becomes more significant, diminishing to an efficiency value of *45%*, as the subtended angle of the hologram extends to 180^o. This efficiency is also independent of hologram size.

The termination efficiency, Figure 4.7 c), increases, to a value of *100%*, as the subtended angle of the hologram increases. However, overall, this efficiency is very low, indicating that there is a significant amount of power remnant at the terminal length of the antenna which has not been scattered by the conducting strips. This efficiency improves for larger holograms, as shown in Figure 4.8. Efficiency values at $\theta = 90^o$, display an increase in this efficiency from *18.4%* to *34%*. This in not a significant increase, as this efficiency is highly dependent on the rate of radiation of the structure. Figure 4.9 displays the termination efficiency versus rate of radiation, αd, for a holographic subtended angle of 90^o. This efficiency improves to a value of *60%* as the hologram radiates more effectively.

The total efficiency, as a product of the spillover, taper, and termination efficiencies is shown in Figure 4.10 for both *10 cm* by *10 cm* and *20 cm* by *20 cm* holograms. It should be noted that this efficiency does not include the efficiency of the feed, η_{feed}. The total efficiency increases as the subtended angle of the holographic antenna is extended, reaching a maximum at $\theta = 176^o$ of *49%* for the *10 cm* by *10 cm* case.

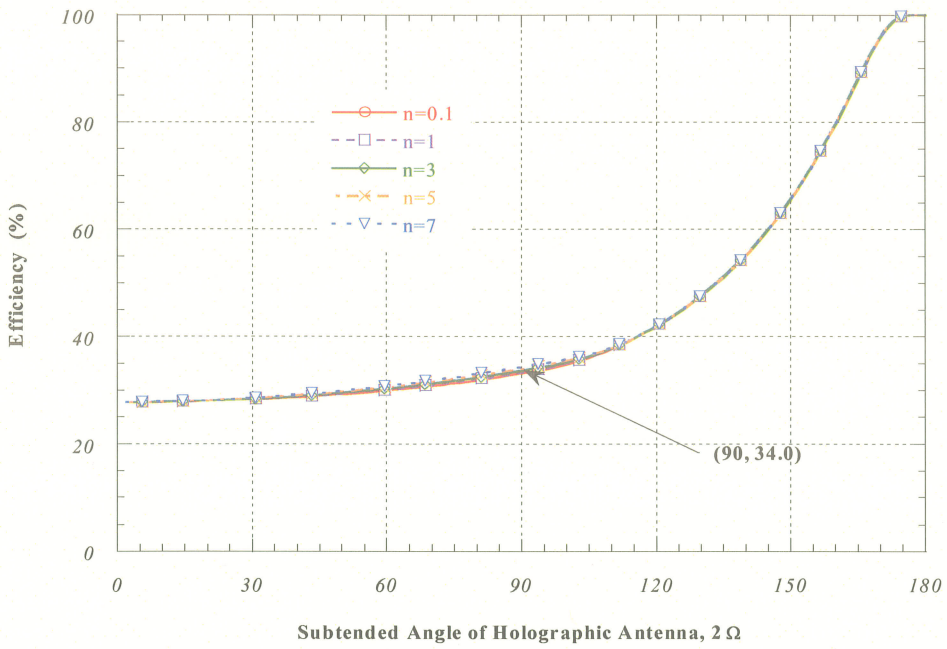

Figure 4.8: Termination Efficiency for a *20 cm* by *20 cm* Diamond Shaped Holographic Antenna

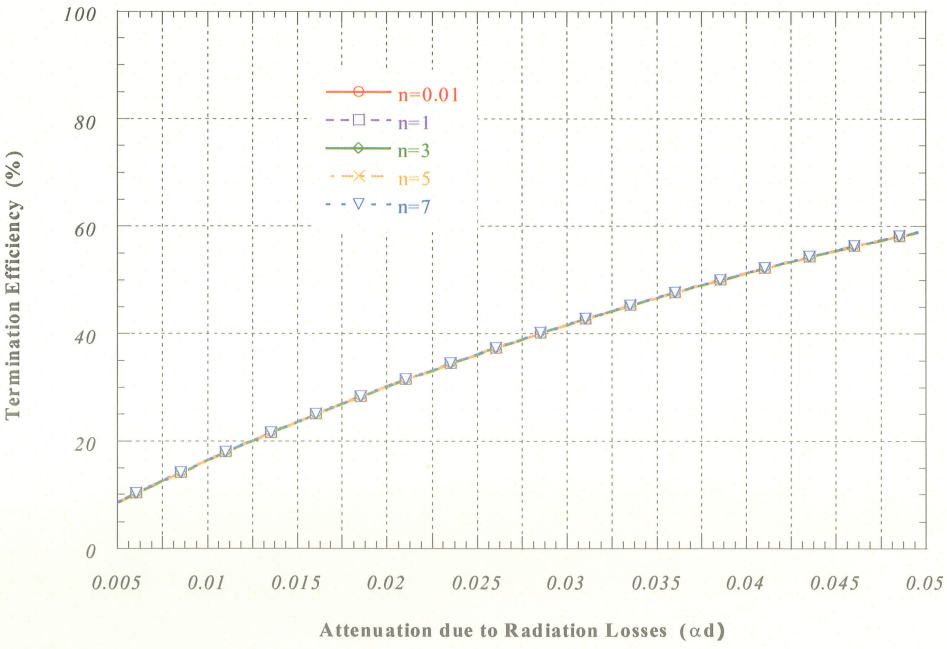

Figure 4.9: Termination Efficiency for a *10 cm* by *10 cm* Hologram versus Radiation Loss

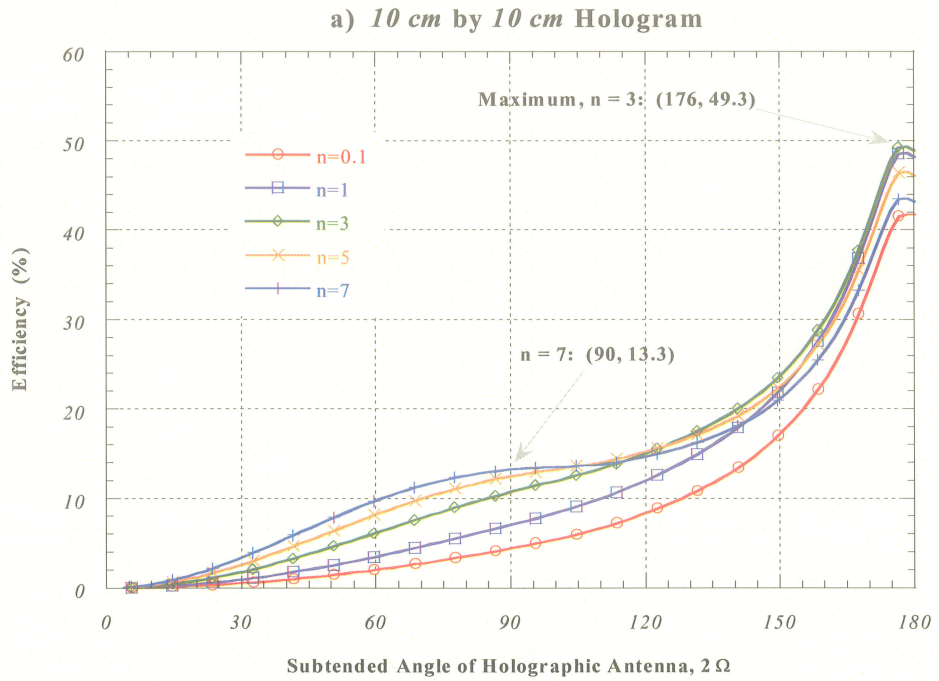

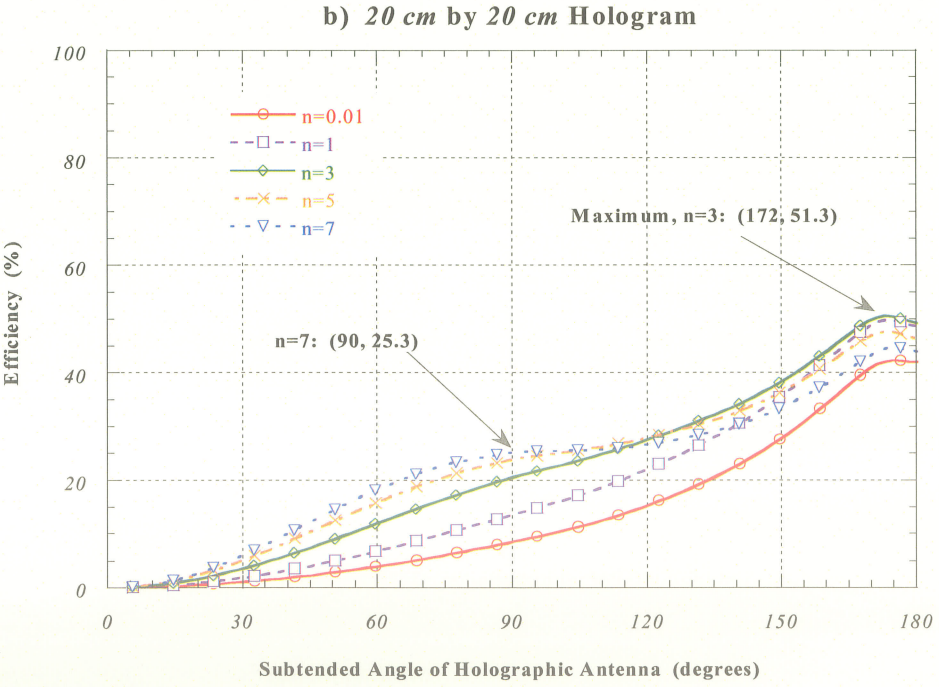

Figure 4.10: Total Efficiency for the Holographic Antenna
a) *10 cm* by *10 cm* Hologram b) *20 cm* by *20 cm* Hologram

The termination efficiency limits the overall efficiency for both cases to a maximum of approximately *50%* when $n = 3$. Due to the improvement of this termination efficiency for larger holographic apertures, the total efficiency improves from *13.3%* to *25.3%* at $\theta = 90^{o}$.

4.5 Efficiency Validation

The efficiency formulation was validated by comparing the measured efficiency values achieved from previous measurements with the efficiency predicted by the formulation. These measurements include the holographic antenna being fed by an open waveguide and a printed dipole antenna. The measured efficiencies are calculated from the equation for gain based on aperture size and is compared with the predicted efficiency which includes the efficiency of the individual feeds.

4.5.1 Open Waveguide Feed

Initially, K. Levis illuminated the hologram with an open waveguide feed, this pattern was shown previously in Figure 2.3, with a maximum gain of *16.15 dBi* at *30 GHz* [6]. The radiation pattern of the open waveguide is displayed below in Figure 4.10. This pattern may be approximated by the $n = 3$ gain curve which is overlaid on the graph. It should be noted that this radiation pattern is unusually ripply, which is uncharacteristic of the open

waveguide, indicating a possible problem with the measurement system or interference from test fixtures.

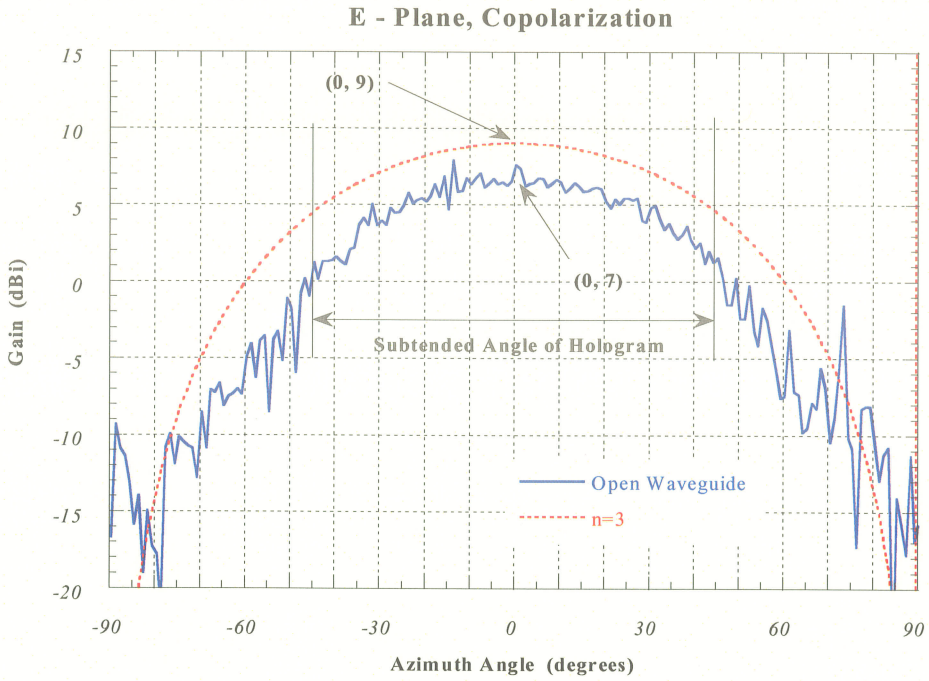

Figure 4.11: Radiation Pattern of an Open Waveguide

The total efficiency predicted for an $n = 3$ feed pattern is *10.8%* for a *10* by *10 cm* diamond shaped hologram with a 90^o subtended angle as demonstrated in Figure 4.12. This efficiency does not account for the feed efficiency which must be calculated separately depending of feed selection. This efficiency will account for any losses existing in the feed device, and its difference from the ideal feed as formulated, which detracts from the overall efficiency.

The feed efficiency, η_{feed}, for the open waveguide may be calculated where G_{actual} is the maximum gain of the open waveguide and G_{ideal} is the ideal feed gain.

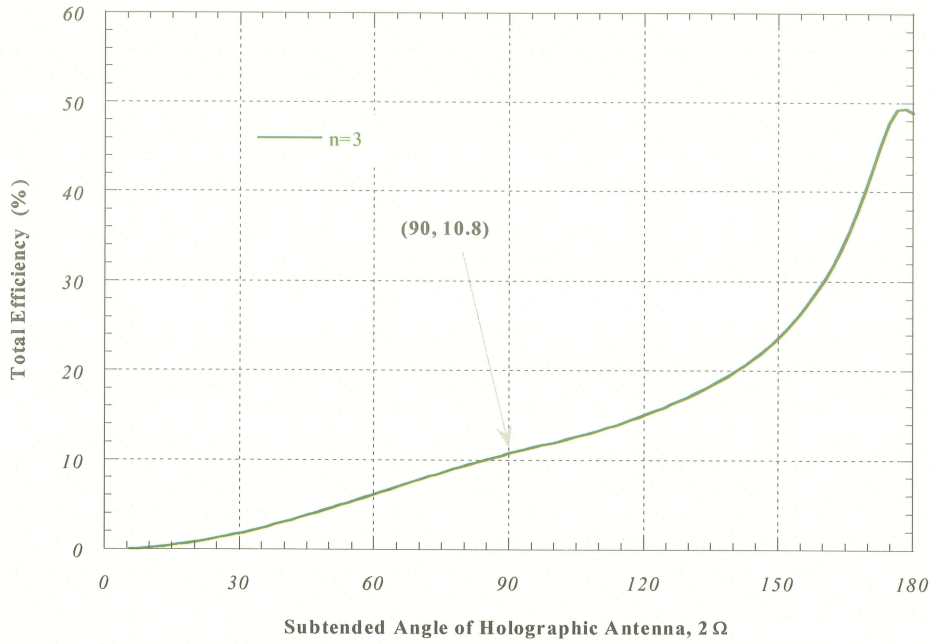

Figure 4.12: Total Efficiency for $n = 3$ Feed Pattern

Consequently,

$$\eta_{feed} = \frac{P_{feed}}{P_{input}} = \frac{G_{actual}}{G_{ideal}} = \frac{10^{0.7}}{10^{0.9}} = 0.63 \qquad (4.38)$$

By including this in our overall efficiency calculation, according to equation (4.4), the total predicted efficiency becomes *6.8%*.

The measured holographic antenna efficiency, η_{meas}, is calculated based on aperture size, A, and wavelength, λ, as shown in the equation for antenna gain, G, in equation (4.39).

$$G = \eta_{meas}\frac{4\pi A}{\lambda^2} \tag{4.39}$$

Given the measured holographic antenna gain of *16.15 dBi* and adding *3 dB* to account for the bidirectional radiation, totals a gain of *19.15 dBi*. The measured efficiency resulting from this gain is *6.5%,* given an aperture area of *100 cm^2* and a *1 cm* wavelength. This is slightly less than the predicted value of *6.8%*, however, is in good agreement with the formulation.

4.5.2 Printed Dipole Antenna Feed

This hologram was also illuminated by a printed dipole feed with the resulting radiation pattern shown in Figure 4.13, demonstrating a maximum measured gain of *14 dBi* [36]. The radiation pattern of the printed dipole antenna is shown in Figure 4.14, and can be approximated by the $n = 2$ curve.

The predicted efficiency for this feed pattern is *9.3%* and is included in Figure 4.15. The feed efficiency for the printed dipole is,

$$\eta_{feed} = \frac{P_{feed}}{P_{input}} = \frac{G_{actual}}{G_{ideal}} = \frac{10^{0.5}}{10^{0.77}} = 0.53 \tag{4.40}$$

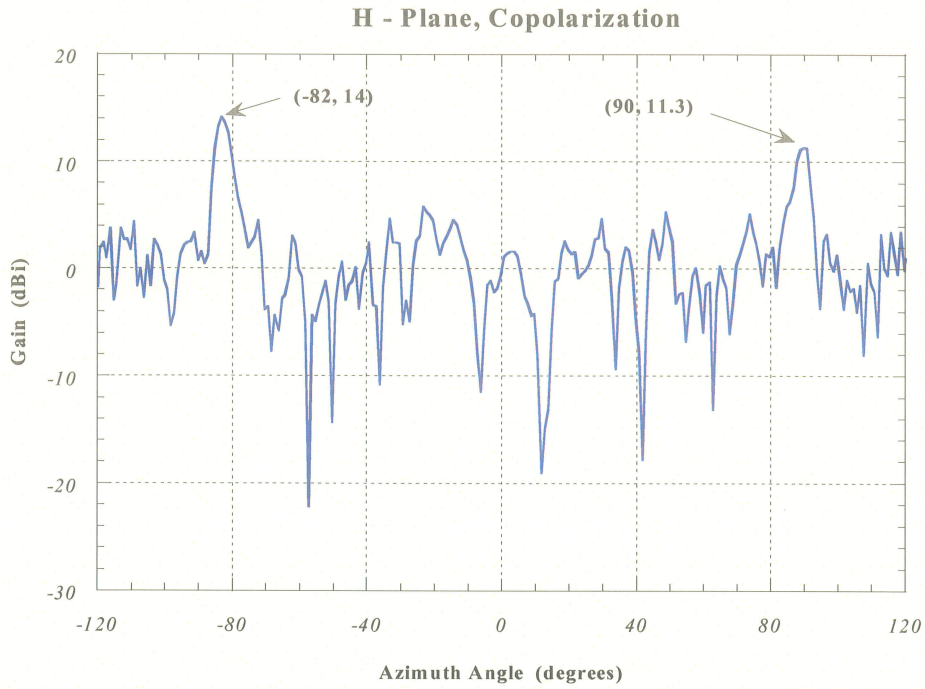

Figure 4.13: Radiation Pattern of the Holographic Antenna with a Printed Dipole Feed

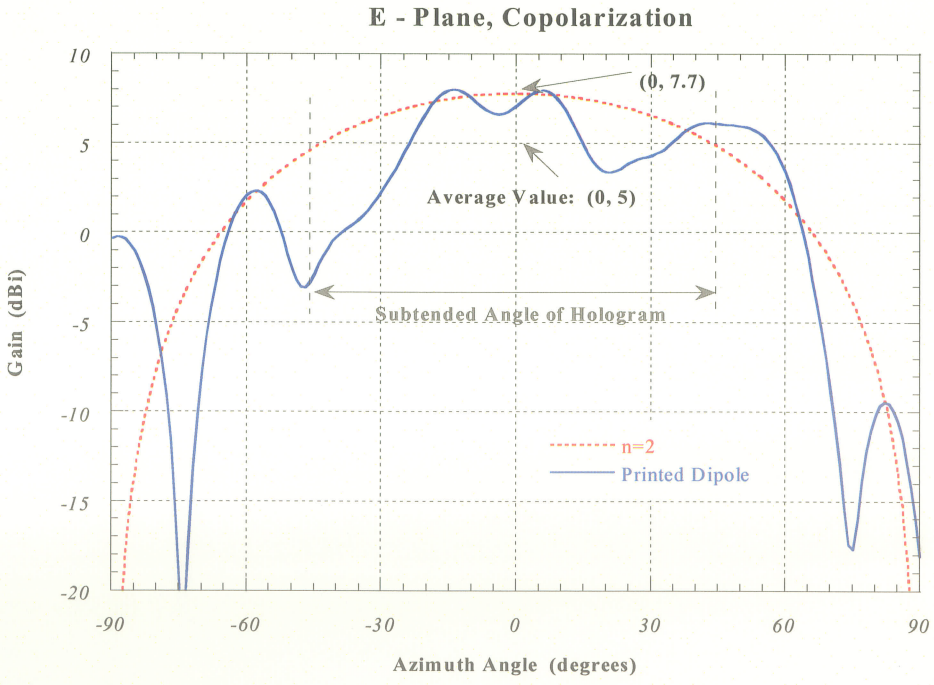

Figure 4.14: Radiation Pattern of the Printed Dipole Antenna

By accounting for this feed efficiency, the overall efficiency becomes *5%*.

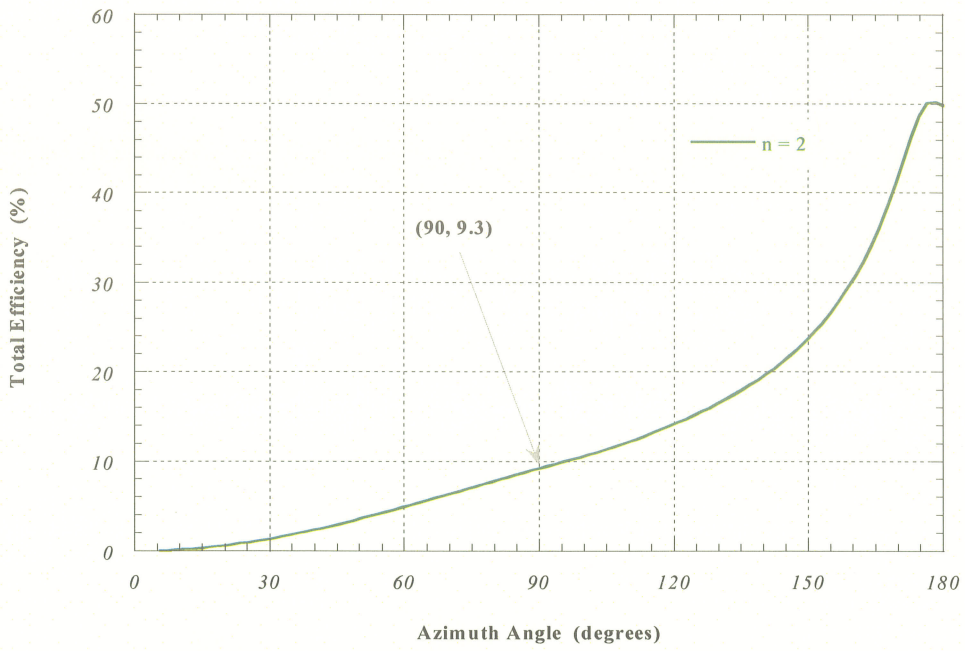

Figure 4.15: Total Efficiency for the *n = 2* Feed Pattern

The measured efficiency can once again be calculated by the equation for gain based on aperture size shown in equation (4.39). Given the holographic antenna gain of *14 dBi* and once again adding *3 dBi* due to the bidirectional radiation of the antenna, the measured efficiency is found to be *4%*.

The results of the efficiency validation are shown in tabular form in Table 4.1.

Table 4.1: Efficiency Validation Results

Feed	Predicted Efficiency	Feed Efficiency	Corrected Efficiency	Measured Gain	Measured Efficiency	Error
Open Waveguide	*10.8%*	*63%*	*6.8%*	*19.15 dBi*	*6.5%*	*0.3%*
Printed Dipole	*9.3%*	*53%*	*5%*	*17 dBi*	*4%*	*1%*

4.6 Conclusion

The efficiency of the holographic antenna has been theoretically determined given varying feed patterns and holographic antenna size. This efficiency comprises the three main sources of loss in the structure, they have been defined as the spillover, amplitude taper of aperture distribution, and termination efficiencies. To formulate the problem, it was postulated that the holographic antenna occupies a conal structure which facilitates determining the feed power which is intercepted by the hologram. Expressions were then derived for each of the efficiencies and plotted to display their dependency on antenna parameters and influence on overall antenna performance. Finally, the accuracy of the formulation was validated by good agreement with the measured results.

The graphical depictions of the efficiencies provided insight into the operation of the holographic antenna. The holographic antenna becomes more efficient as the subtended angle of the holographic antenna increases, and varies within a few percent given different feed

patterns. Larger holograms are more efficient due to the improvement of the termination efficiency. For this case, the overall efficiency of the holographic antenna reached a maximum of *50%* which is limited by the termination efficiency. This is due to the slow rate of radiation of the hologram. This formulation may now be employed as a design aid in future antenna fabrication.

Chapter 5: Holographic Antenna Feed Design

5.1 Introduction

The linear tapered slot antenna is a viable alternative to existing holographic antenna feed devices. This antenna has demonstrated variable beamwidths and a bandwidth large enough to accommodate the narrow bandwidth of the holographic antenna. In addition, this antenna may be etched onto the same substrate as the holographic antenna providing a single unit low profile device.

The formulation derived in Chapter 4 to assess the holographic antenna's efficiency may be used as a design aid to determine feed requirements and holographic antenna size. Once the efficiency criteria has been established, the LTSA may be designed to generate the desired feed pattern.

In this chapter, two prototypes were fabricated using the LTSA as a holographic antenna feed. The initial design was used to verify the efficiency formulation and finally an LTSA was designed to improve the performance of the hologram.

5.2 Holographic Antenna Feed Design

5.2.1 Initial Feed Design

The initial LTSA design was sought to illuminate a *10* by *10 cm* holographic antenna with a 90^o subtended angle operating at *30 GHz*. A visual estimate was used to determine the feed requirements for this design. This necessitated a feed which would illuminate the hologram uniformly with a spherical wave. In addition, a more compact design than the previously designed LTSAs in Chapter 3 was sought to reduce the surface area of the final structure, with elongated edges, *D*, to prevent scattering from these edges from interfering with the pattern (Figure 3.5).

The design guidelines outlined in Chapter 3 were implemented to construct this LTSA, and a microstrip line was once again used as the feed method. The LTSA dimensions are shown in Table 5.1.

Table 5.1: Dimensions of $2\gamma = 13.6^o$ LTSA at *30 GHz*

Substrate: Duroid 4003	$\varepsilon_r = 3.38$	$t = 20mils$	$\sigma = 0.001$
Aperture Angle: $2\gamma = 13.6^o$	$2W = 0.36cm$	$2D = 14.1cm$	$L = 2.9cm$
Microstrip Line:	$w = 0.124cm$	$\lambda_m = 0.61cm$	$\lambda_m/4 = 0.15cm$
Slotline:	$w = 0.110cm$	$\lambda_s = 0.7cm$	$\lambda_s/4 = 0.175cm$

The simulated E-plane and H-plane near field patterns, using Ansoft HFSS, are shown in Figure 5.1 a) and b), respectively [32]. The E-Plane demonstrates a *3 dB* beamwidth of 135^o which will illuminate the hologram uniformly and the H-plane has a narrower half-power beamwidth of 21^o. The spike located at -35^o in the H-plane pattern is due to scattering from the microstrip feedline.

For proper excitation, the phase center of the LTSA was located and placed at the focal point of the hologram. The phase center of the LTSA was found to be *0.1 cm* within its tapered edges. Figure 5.2 displays the phase distribution at the eventual location of the first conducting strip, *1 cm* from the LTSA's focal point, which is uniform with respect to the phase center. This indicates the successful launching of a spherical wave.

The measured holographic antenna results are included in Figure 5.4. The return loss, Figure 5.4 a), indicates a good match from *30 GHz* to *31.6 GHz*. The H - plane pattern demonstrates the hologram radiating as desired, with beam peaks at -85.5^o and 81^o. The gain reached a maximum of *13.63 dBi* at a frequency of *31.7 GHz,* which varied by *1 dBi* from *30* to *32 GHz*.

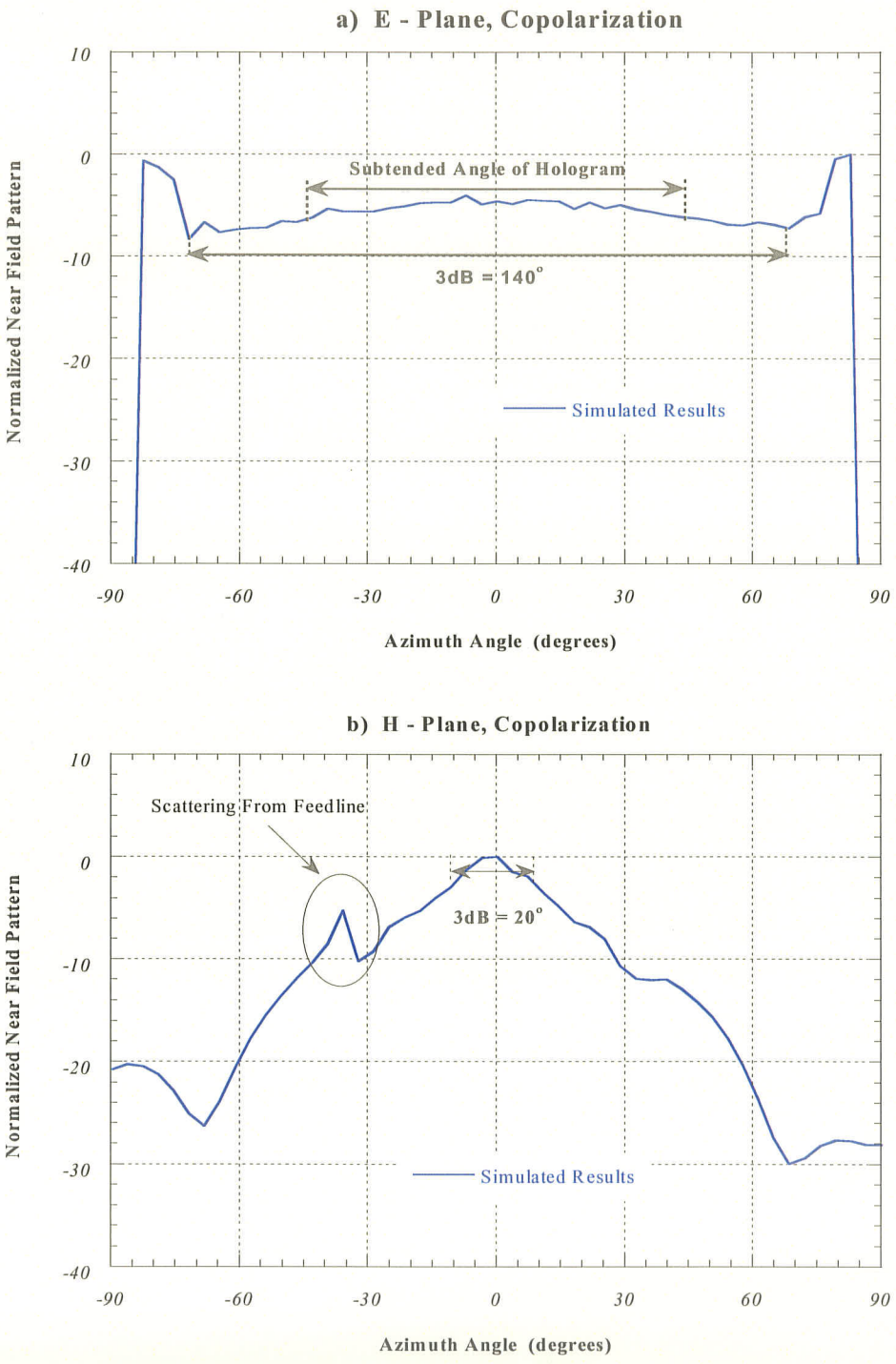

Figure 5.1: Normalized Simulated Near Field Radiation Pattern of a $2\gamma = 13.6^{o}$ LTSA a) E - Plane, Copolarization b) H - Plane, Copolarization

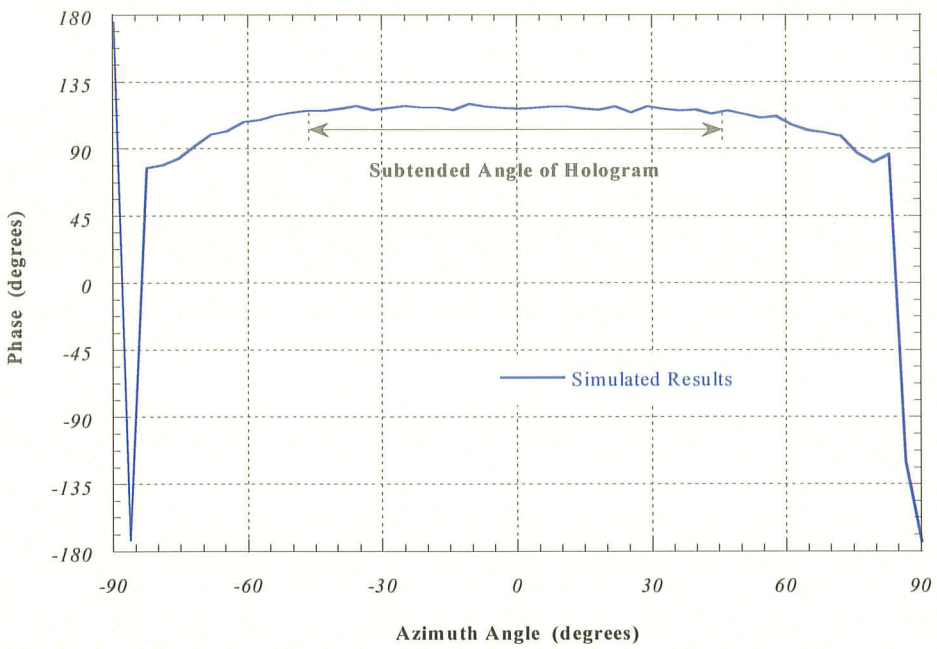

Figure 5.2: Phase Distribution @ *1 cm* from the $2\gamma = 13.6^{o}$ LTSA Phase Center

This LTSA was then etched onto the same substrate as the holographic antenna. An image of this final structure is shown in Figure 5.3.

To calculate the feed efficiency, the LTSA was tested individually and the far field measurements are included in Figure 5.5. This feed pattern can be approximated by the $n = 1.5$ curve shown overlaid on the graph. This pattern exhibits pronounced rippling which may be attributed to an inaccurate measurement system.

This information can be used to determine the feed efficiency and finally the predicted efficiency of the design, where G_{actual} is the gain of the LTSA and G_{ideal} is the gain of the ideal feed with the $n = 1.5$ curve.

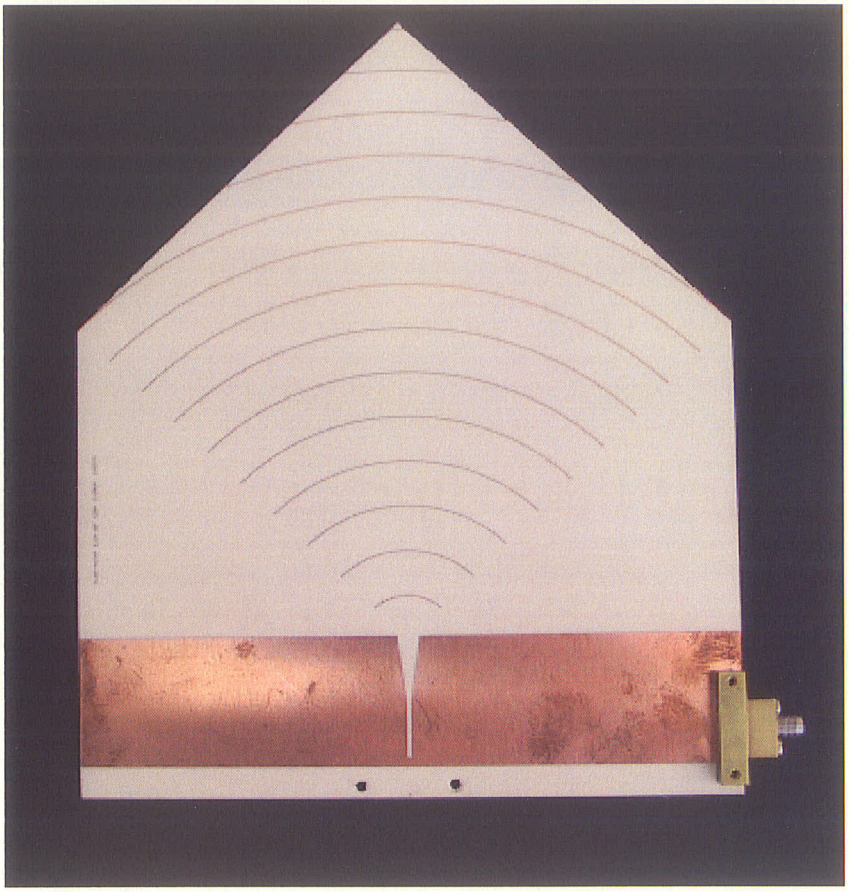

Figure 5.3: Photograph of the Holographic Antenna with an LTSA Feed

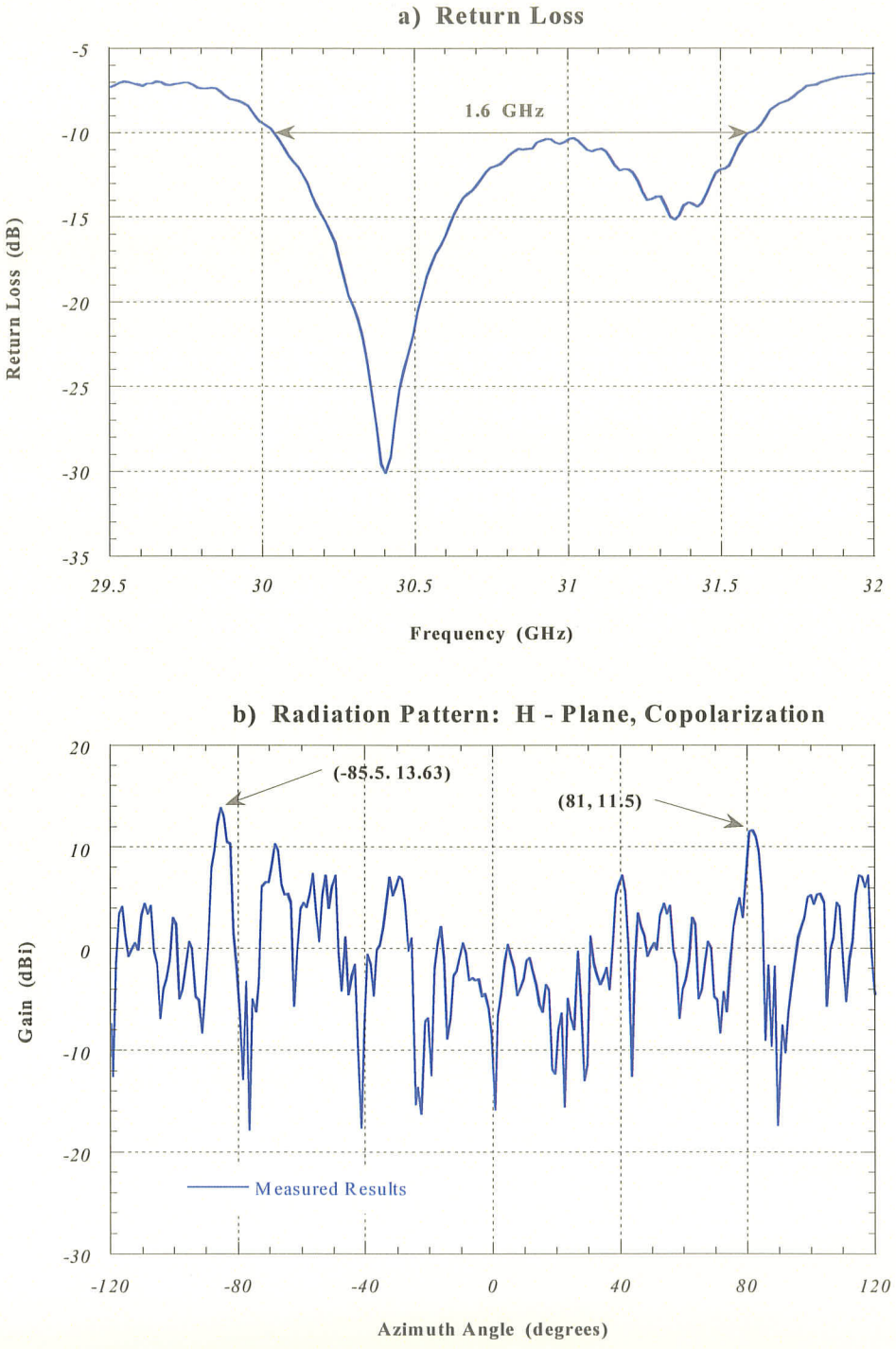

Figure 5.4: Measured Holographic Antenna Results with a $2\gamma = 13.6^{o}$ LTSA Feed a) Return Loss b) Far Field Radiation Pattern: H - Plane, Copolarization

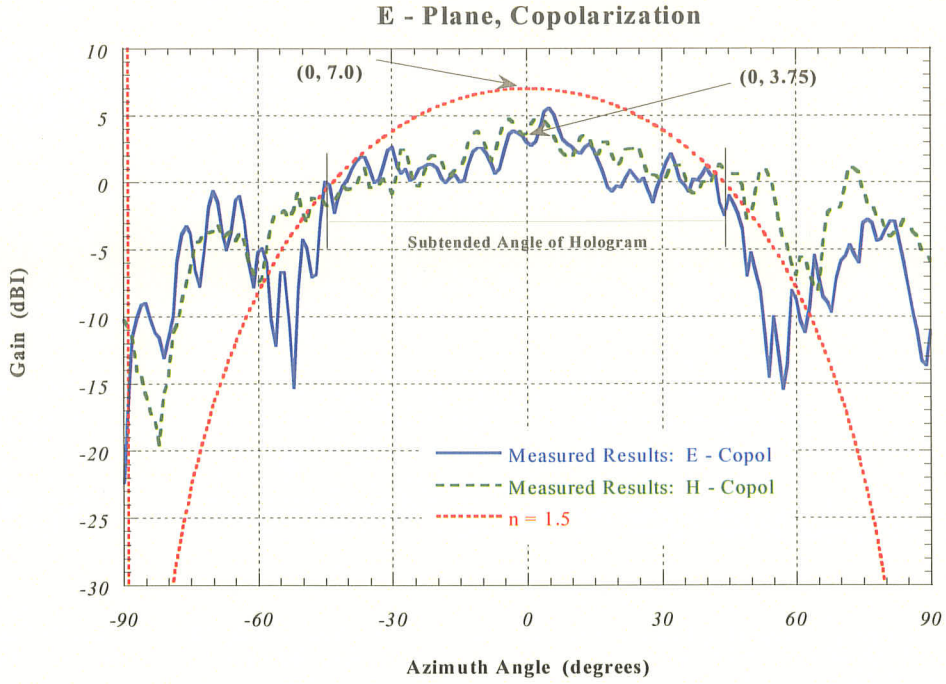

Figure 5.5: Radiation Pattern of $2\gamma = 13.6^{o}$ LTSA with *n = 1.5* Feed Pattern

$$\eta_{feed} = \frac{P_{feed}}{P_{input}} = \frac{G_{actual}}{G_{ideal}} = \frac{10^{0.375}}{10^{0.7}} = 0.43 \qquad (5.1)$$

The 3.25 *dBi* difference between the actual and ideal gain may be due to microstrip line and slotline losses as discussed in Chapter 3, and the pattern difference outside the main lobe. Based on previous measurements, the losses in the slotline were calculated to be 0.*59 dB* and *2.15 d*B of losses in the microstrip feed line for a total of *2.74 dB*.

The predicted efficiency for the $n = 1.5$ curve is shown in Figure 5.6, with a value of 8% for a *10* by *10 cm* holographic antenna with a 90^o subtended angle. The corrected value, including the feed efficiency of *43%*, is *3.4%*.

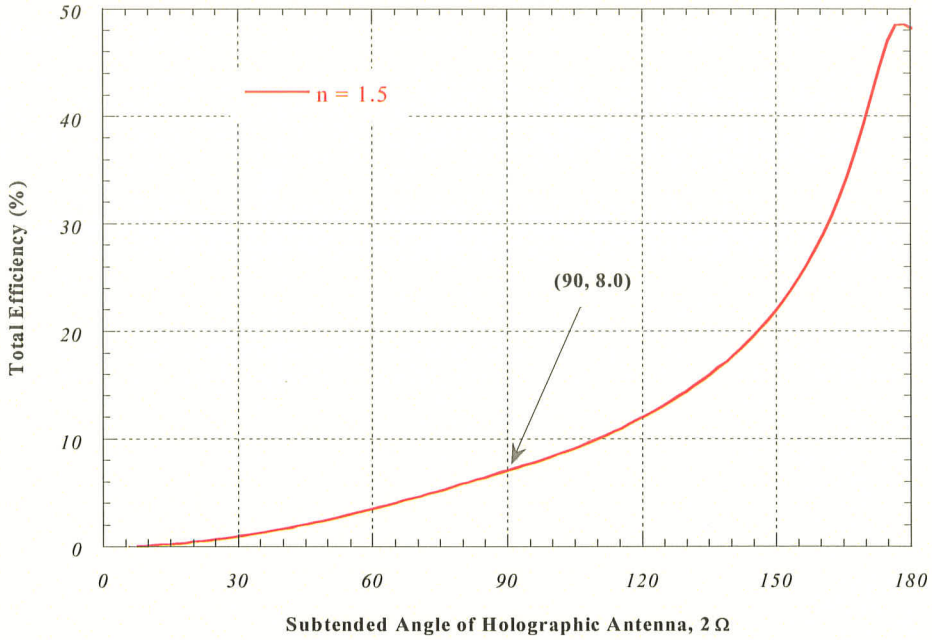

Figure 5.6: Total Efficiency for $n = 1$ Feed Pattern

The measured holographic antenna gain of *13.63 dBi* can be used to calculate the measured efficiency value of this structure, adding *3 dBi*, once again, to account for the bidirectional radiation of the antenna, for a total gain of *16.63 dBi*. Using the equation for gain based on aperture size, shown in equation (4.39), and given an aperture area of $100cm^2$ and a wavelength of $0.95cm$, the efficiency of this antenna was calculated to be *3.3%*. This value is slightly less than the predicted value of *3.4%*. These results are tabulated in Table 5.3.

The immediate improvement of the gain of the holographic antenna was observed by adding copper strips to confine the field launched from the LTSA to the hologram. These strips were triangular in shape and filled in the area between the LTSA and the two lower edges of the hologram. This far field radiation pattern is included in Figure 5.7. This successfully increased the gain of the antenna to *14.54 dBi* at a frequency of *31.5 GHz* by reducing spillover losses, resulting in an increased efficiency from *3.3%* to *4%*.

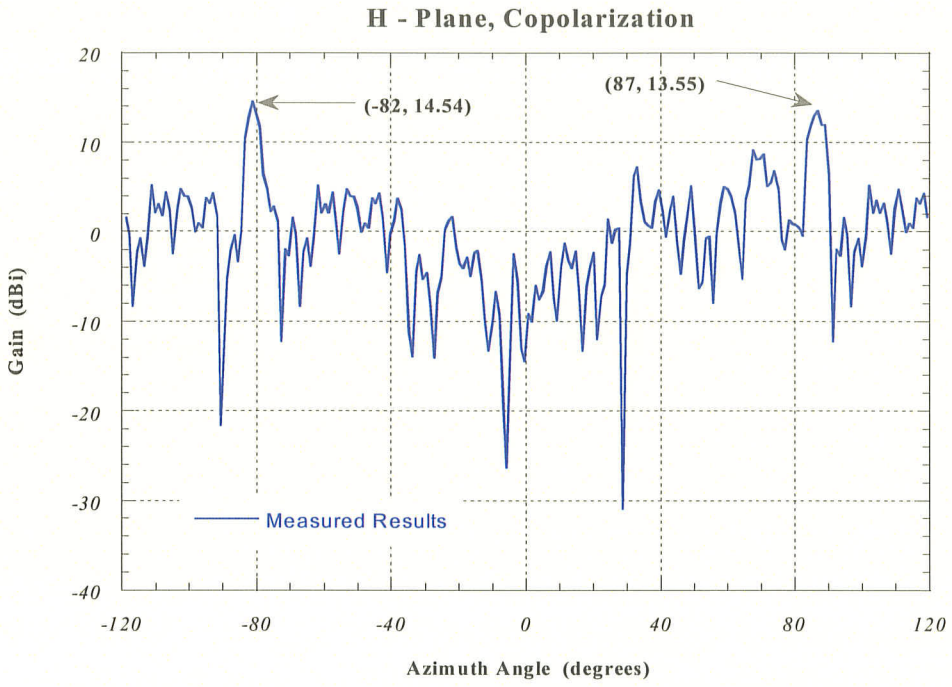

Figure 5.7: Radiation Pattern of Holographic Antenna with Copper Strips Reducing Spillover Loss

5.2.2 High Efficiency Feed Design

The second LTSA was designed to improve the efficiency of the holographic antenna according to the formulation established in Chapter 4. By extending the subtended angle of the hologram to 120^{o} and generating an $n = 5$ feed pattern, a potential holographic

antenna efficiency of *15.3%* is endeavored based on the efficiency curve shown in Figure 5.8, for a *10* by *10 cm* holographic antenna

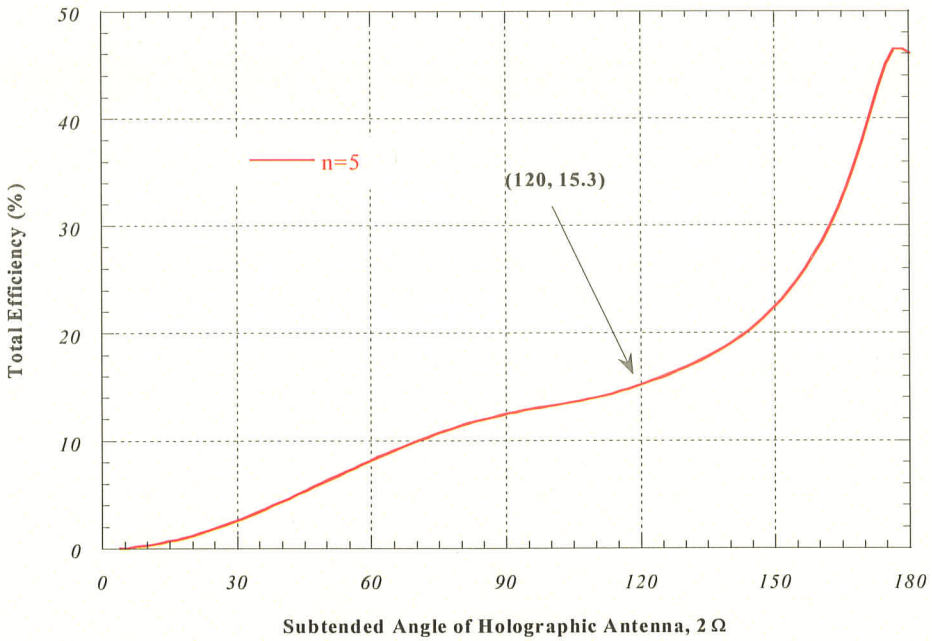

Figure 5.8: Total Efficiency for $n = 5$ Gain Curve

An LTSA with a subtended angle of $2\gamma = 16^{o}$ generated the $n = 5$ feed pattern. The final dimensions are included in Table 5.2. The normalized far field pattern is shown in Figure 5.9 a) comprising the $n = 5$ curve. The phase distribution measured at *10 cm* from the focal point of the LTSA is shown in Figure 5.9 b) denoting spherical wave generation with an acceptable 35^{o} phase taper over the subtended angle of the hologram.

Table 5.2: Dimensions of $2\gamma = 16^o$ LTSA at 30 GHz

Substrate: Duroid 4003	$\varepsilon_r = 3.38$	$t = 20mils$	$\sigma = 0.001$
Aperture Angle: $2\gamma = 16^o$	$2W = 0.86cm$	$2D = 8cm$	$L = 2.9cm$
Microstrip Line:	$w = 0.124cm$	$\lambda_m = 0.61cm$	$\lambda_m/4 = 0.15cm$
Slotline:	$w = 0.110cm$	$\lambda_s = 0.7cm$	$\lambda_s/4 = 0.175cm$

This LTSA was etched onto the same substrate as the hologram by positioning the focal point of the LTSA at the apex of the hologram. Return loss measurements, Figure 5.10 a), indicate successful matching of the structure from *29.5 GHz* to *32 GHz*. The far field measurements, Figure 5.10 b), demonstrate an achieved maximum gain of *12.17 dBi* at *31.8 GHz,* remaining within *2 dBi* from *30* to *32 GHz*. This is much lower than anticipated and an investigation was performed into the source of this loss.

The LTSA was then measured separately from the hologram. The far field measurements are included in Figure 5.11, and indicate that the LTSA is generating far less gain in comparison with the $n = 5$ feed pattern. Again, pattern rippling is significant indicating a potentially imprecise measurement setup which may also account for the low gain measured.

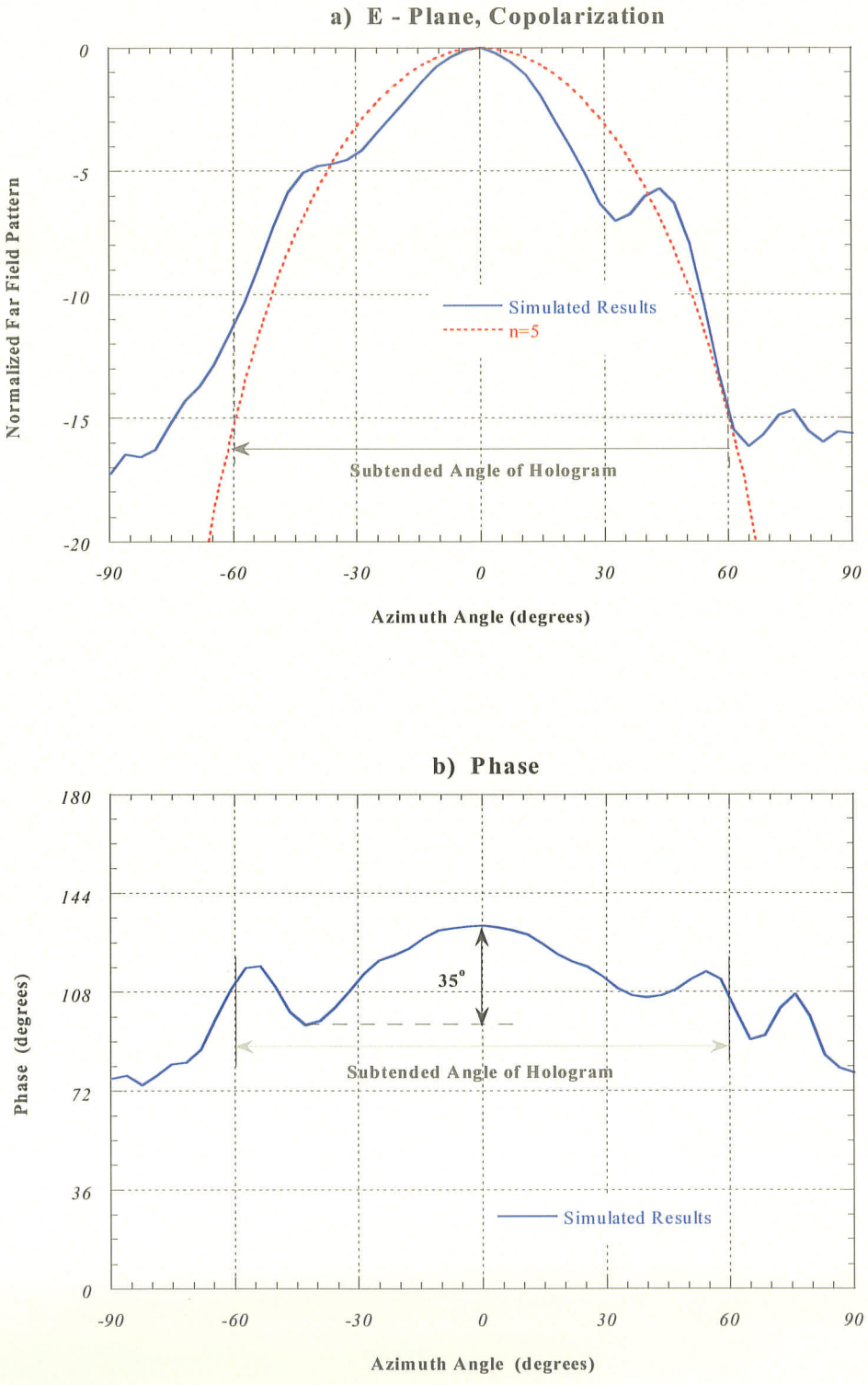

Figure 5.9: Simulated Far Field Results of a $2\gamma = 16^{o}$ LTSA
a) Far Field Radiation Pattern: E - Plane, Copolarization b) Phase Distribution

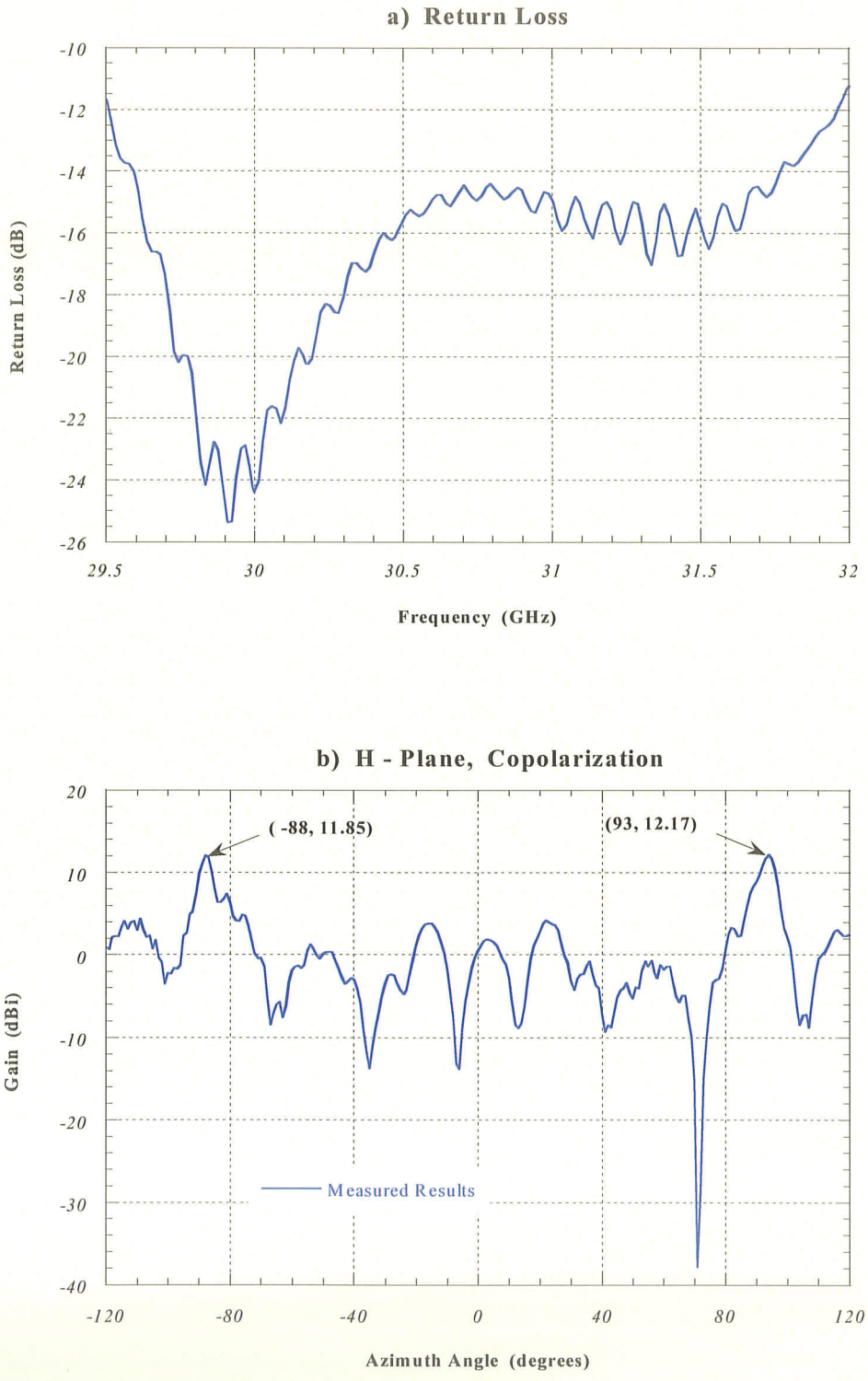

Figure 5.10: Measured Holographic Antenna Results with a $2\gamma = 16^{o}$ LTSA Feed
a) Return Loss b) H - Plane, Copolarization

This measurement evidences a very low feed efficiency which accounts for the fallen holographic antenna gain. This feed efficiency, equation (5.2), of *13%* reduces the potential achievable efficiency of this design to 2%.

$$\eta_{feed} = \frac{P_{feed}}{P_{input}} = \frac{G_{actual}}{G_{ideal}} = \frac{10^{0.2}}{10^{1.1}} = 0.13 \qquad (5.2)$$

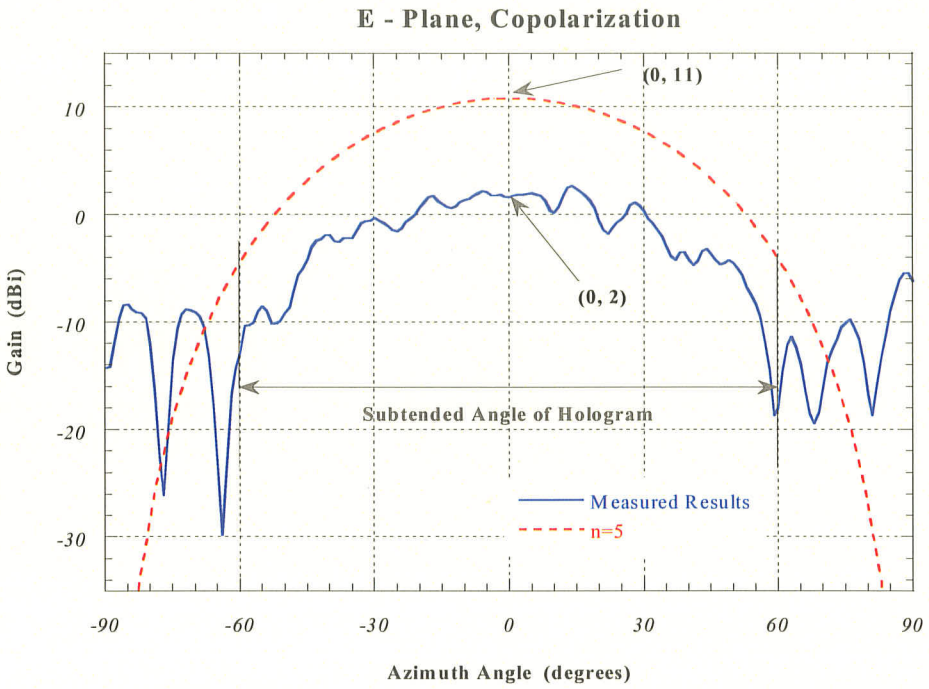

Figure 5.11: Radiation Pattern of $2\gamma = 16^{o}$ LTSA with *n = 5* Feed Pattern

The measured efficiency, based on a gain of *15.17 dBi*, including *3 dBi* for the bidirectional radiation is *2.4%*. This is slightly better than the predicted efficiency value of *2%*, and is summarized in Table 5.3. Figure 5.11 clearly indicates that significant loss occurs

in this LTSA. This is confirmed from the observation of the LTSA patterns which show significant crosspolarization and back lobe levels.

A comparison is included between the simulated gain of this LTSA and the observed gain of this same structure. A discrepancy of *8 dBi* is apparent between the two traces in Figure 5.12. It is not evident whether the source of this error lies with the software or the measurement setup, therefrom, an investigation will have to be performed into the nature of the loss.

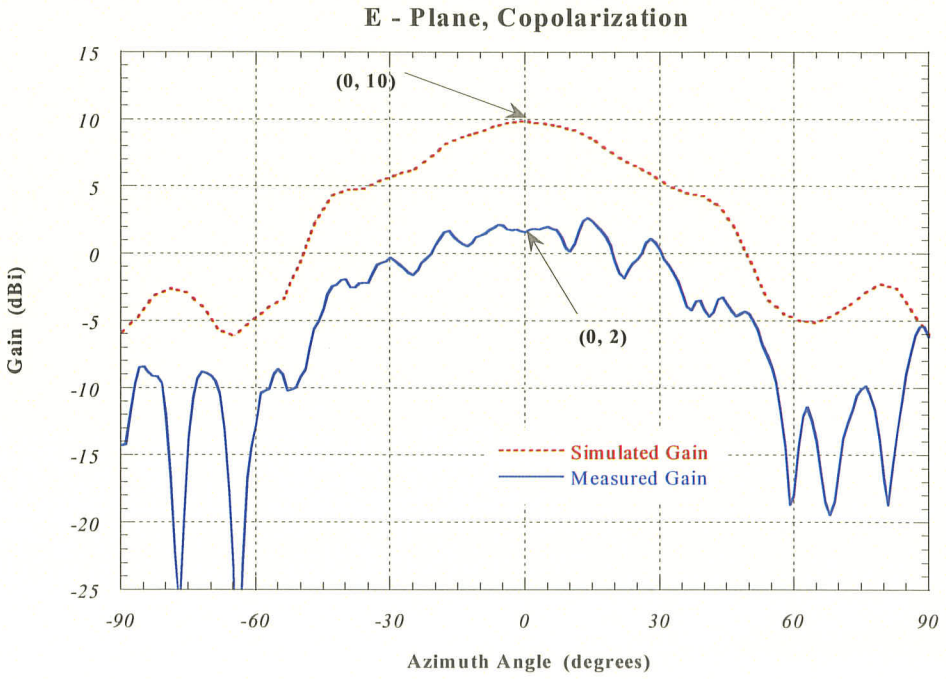

Figure 5.12: Simulated and Measured Gain of a $2\gamma = 16^{o}$ LTSA

Far field measurements were taken of this LTSA with elongated taper edges, *L*, achieved by applying copper tape (Figure 3.5). This generated higher gain, as shown in Figure 5.13,

suggesting that future LTSA designs with extended tapering could provide improved gain to illuminate the holographic antenna thus improving the efficiency of the entire structure.

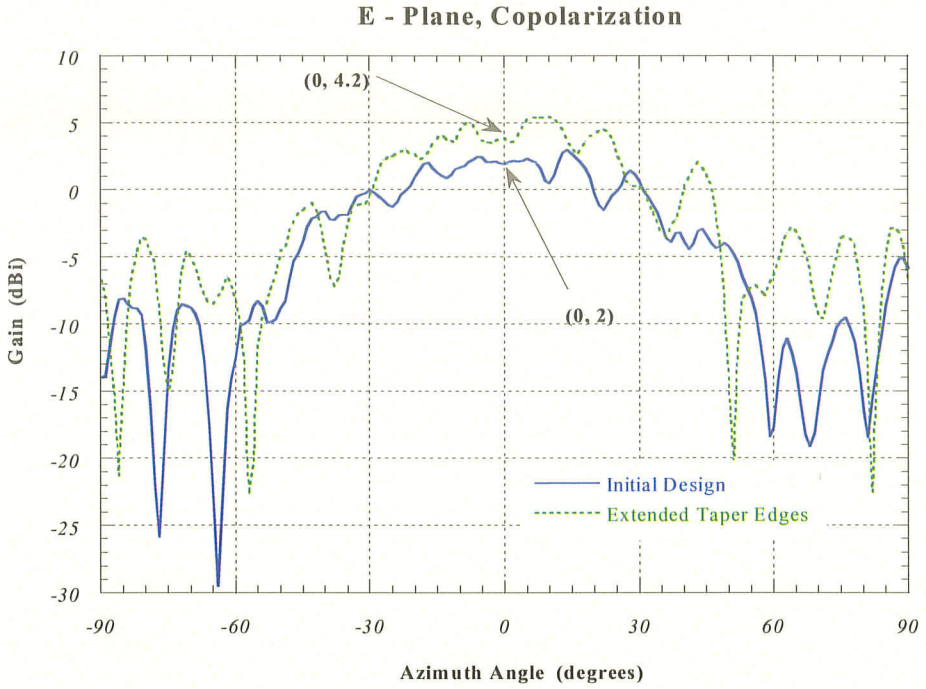

Figure 5.13: Measurements of an LTSA with and without Taper Extensions

An additional measurement was taken to ascertain the consistency of the LTSA radiation pattern along the holographic structure. To do so, far field measurements were taken of the LTSA with a substrate extension similar in shape to the hologram, however, devoid of the conducting strips. This normalized measurement is included in Figure 5.14 in comparison with the LTSA without the substrate extension. As demonstrated, the pattern does not change, save slight rippling, in the presence of the extended substrate.

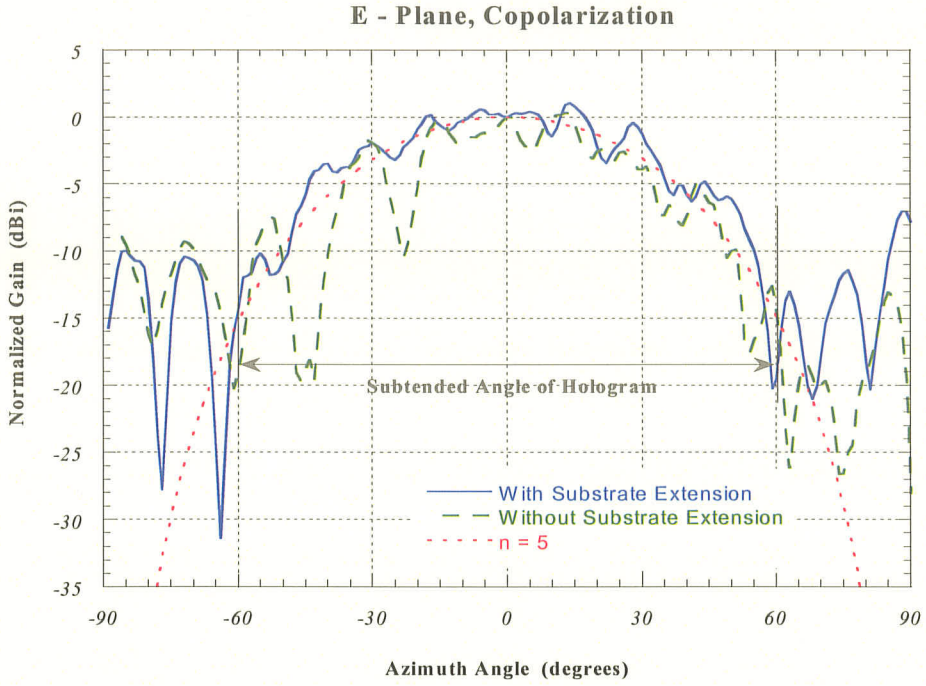

Figure 5.14: Measurements of the LTSA with and without Substrate Extensions

Table 5.3: Efficiency Results of Holograms with an LTSA Feed

Feed	Predicted Efficiency	Feed Efficiency	Corrected Efficiency	Measured Gain	Measured Efficiency	Error
LTSA $2\gamma = 13.6^o$ $n = 1.5$	8%	*43%*	*3.4%*	*16.63 dBi*	*3.3%*	*0.1%*
LTSA $2\gamma = 16^o$ $n = 5$	*15.3%*	*13%*	*2%*	*15.17 dBi*	*2.4%*	*0.4%*

5.4 Conclusion

The linear tapered slotline antenna has been implemented as a holographic antenna feed. Initial measurements confirm that the LTSA properly illuminates the hologram with a spherical wave while providing sufficient bandwidth.

The controllable beamwidths available with the LTSA allow the designer to generate varied feed patterns which will influence the efficiency of the hologram.

The efficiency formulation, derived in Chapter 4, was validated by the initial design and used as a guideline in the hopes of generating a more efficient holographic antenna. Although the design met the predicted efficiency value, it was hindered by the very low gain of the LTSA which significantly degraded the efficiency of the structure to *2%*. The gain of the LTSA can be improved by lengthening the tapered edges of the antenna thus functioning as a more efficient feed for the hologram.

Chapter 6: Conclusion

6.1 Conclusions

The holographic antenna has been validated as a high gain antenna in the Ka - band frequency range which may potentially replace existing technologies such as parabolic, lens, and phased array antennas where a low profile antenna is desired. However, current feed devices for this antenna, including open waveguides and horns, detract from the planar nature of the hologram and require manual alignment with the antenna which may introduce loss into the system given the strict accuracy requirements needed at high frequencies. In addition, given the early stages of research in this field, very little analysis has addressed the efficiency of this structure. This work has introduced the linear tapered slotline antenna as a potential holographic antenna feed and also discussed the efficiency of this structure to determine its dependency on feed illumination patterns and holographic antenna shape and size.

The single layer holographic antenna consisting of concentric conducting rings was used as the basis for this thesis. The efficiency formulation, and feed recommendations may also be applied to other holographic antennas such as the volume type hologram and

dipole hologram.

The linear tapered slotline antenna is a printed traveling wave antenna with a large bandwidth and controllable beamwidths. These features make it attractive as a holographic antenna feed as it will complement the planar nature of the primary structure while generating any desired illumination pattern. Two LTSA prototypes were constructed using the same substrate as the hologram. Although this substrate was outside of the recommended range, yielding high sidelobes and pattern rippling, the varying beamwidths and gain displayed the LTSA's potential as a holographic antenna feed.

The holographic antenna efficiency was addressed by postulating that the hologram occupies a conic section. By doing so, an intercepting area was provided for which to calculate the power delivered and later rescattered by the hologram. The three main efficiencies were defined as spillover, taper, and termination efficiencies. These account for losses incurred when feed power is radiated outside of the intercepting holographic area, amplitude tapering across the aperture of the hologram, and power that is residual at the length of the antenna, respectively. Equations were derived to represent each of these efficiencies, dependent on feed pattern, and holographic antenna shape and size. Graphical depictions of these efficiencies were then generated to view the impact of the varied parameters on overall antenna efficiency. The total efficiency is most dependent on the shape of the hologram and improves greatly as the holographic antenna subtended angle is increased. Variations in the illuminating patterns alters the total efficiency within a few percent.

The predicted efficiency values were then confirmed by comparing them with measured efficiency values. Both the open waveguide and printed dipole antenna feeds measured efficiency values complied with the predicted results.

An initial design using a linear tapered slotline antenna as an illuminating device also validated the efficiency formulation when measured results were compared with those predicted. Following this, the formulation was used as a design guideline to improve the efficiency of the overall structure. An LTSA was designed to generate the required feed pattern and the subtended angle of the hologram was widened to achieve this improved efficiency. The final results indicate a very low efficiency which was incurred by a very lossy LTSA. This resulted in a very poor feed efficiency which degraded the overall value, thus not attaining the more efficient holographic antenna as desired.

6.2 Future Work

Since the hologram is still in the early stages on development, more research needs to be done. However, in the immediate future, the following studies should be performed.

The linear tapered slotline antenna is a viable alternative to holographic antenna feeds, although the gain of this antenna must be high enough to efficiently illuminate the hologram. As the substrate used was outside of the recommended range for the LTSA, perhaps the hologram could be designed on a substrate which would accommodate the LTSA's requirements. Another option would be machining holes in the substrate underlying the LTSA to effectively reduce the permittivity, enabling the effective thickness of this antenna to lie within the established guidelines.

As the overall efficiency was limited by the termination efficiency, due to the slow radiation of the structure, an investigation should be performed into controlling the scattering characteristics of the hologram which would significantly improve the efficiency by reducing residual power at the length of the antenna and thus reducing sidelobe levels. This may be accomplished by varying the widths of the conducting strips or using an alternate substrate. For given hologram dimensions, the optimum rate of radiation can be established to generate the maximum achievable gain.

At present, a hologram is simply a set of conducting strips representing a discretization of the sinusoidal term in the interference pattern. Alternative hologram realization should be examined including different type of groove profiles on a substrate. The approach may offer a better controlled rate of radiation and polarization than the one based on concentric conducting strips. Ultimately, a more complete hologram representation should be explored for better operational efficiency.

In addition, other hologram modifications could be examined including generating a circularly polarized hologram from a single linearly polarized feed. This may be accomplished by proper alignment of the dipoles in the dipole type holographic antenna. Other potential holograms worthy of consideration include holograms with multi-beam capabilities or holograms which generate an off broadside beam.

Appendix A: Alternative Form of Reciprocity Theorem

Let $\bar{E}^a$; $\bar{H}^a$ and $\bar{E}^b$; $\overline{H}^b$ be two sets of source free Maxwell's equations with time dependency $e^{j\omega t}$, hence,

$$\nabla\times\bar{E}^a = -j\omega\mu\bar{H}^a \tag{A.1}$$

$$\nabla\times\bar{H}^{a*} = -j\omega\mu\bar{E}^{a*} \tag{A.2}$$

$$\nabla\times\bar{E}^b = -j\omega\mu\bar{H}^b \tag{A.3}$$

$$\nabla\times\bar{H}^{b*} = -j\omega\mu\bar{E}^{b*} \tag{A.4}$$

The asterix, $*$, represents the complex conjugate. From (A.1) to (A.4), performing the following operations gives,

$$\bar{H}^{b*}\cdot\nabla\times\bar{E}^a = -j\omega\mu\bar{H}^{b*}\cdot\bar{H}^a \tag{A.5}$$

$$\bar{E}^{b*}\cdot\nabla\times\bar{H}^a = -j\omega\varepsilon\bar{E}^b\cdot\bar{E}^{a*} \tag{A.6}$$

$$\bar{H}^{a*}\cdot\nabla\times\bar{E}^b = -j\omega\mu\bar{H}^{a*}\cdot\bar{H}^b \tag{A.7}$$

$$\bar{E}^a \cdot \nabla \times \bar{H}^{b*} = -j\omega\varepsilon \bar{E}^a \cdot \bar{E}^{b*} \tag{A.8}$$

Equations (A.5) and (A.8) become, after applying the vector identity,

$$\nabla \cdot (\bar{E}^a \times \bar{H}^{b*}) = -j\omega\mu(\bar{H}^{b*} \cdot \bar{H}^a) + j\omega\varepsilon(\bar{E}^a \cdot \bar{E}^{b*}) \tag{A.9}$$

Performing a similar operation to equation (A.7) and (A.6),

$$\nabla \cdot (\bar{E}^b \times \bar{H}^{a*}) = -j\omega\mu(\bar{H}^{a*} \cdot \bar{H}^b) + j\omega\varepsilon(\bar{E}^{a*} \cdot \bar{E}^b) \tag{A.10}$$

By summing equations (A.9) and (A.10),

$$\nabla \cdot [\bar{E}^a \times \bar{H}^{b*} + \bar{E}^b \times \bar{H}^{a*}] = -2j\omega\mu Re(\bar{H}^a \cdot \bar{H}^{b*}) + 2j\omega\varepsilon Re(\bar{E}^a \cdot \bar{E}^{b*}) \tag{A.11}$$

Where $Re(\ )$ designates the real part of a complex value.

It is clear that the right hand side of equation (A.11) is always imaginary, consequently,

$$Re[\nabla \cdot (\bar{E}^a \times \bar{H}^{b*} + \bar{E}^b \times \bar{H}^{a*})] = 0 \tag{A.12}$$

or, in the integral form as shown in equation (A.13),

$$Re\oint_S (\bar{E}^a \times \bar{H}^{b*} + \bar{E}^b \times \bar{H}^{a*}) \cdot \hat{n} ds = 0 \qquad \text{(A.13)}$$

Equation (A.13) can be regarded as an alternative form of the reciprocity theorem. It shows another relation between two sets of fields, *a* and *b*, which is a variation of the Lorentz reciprocity theorem [34].

Appendix B: Termination Efficiency Details

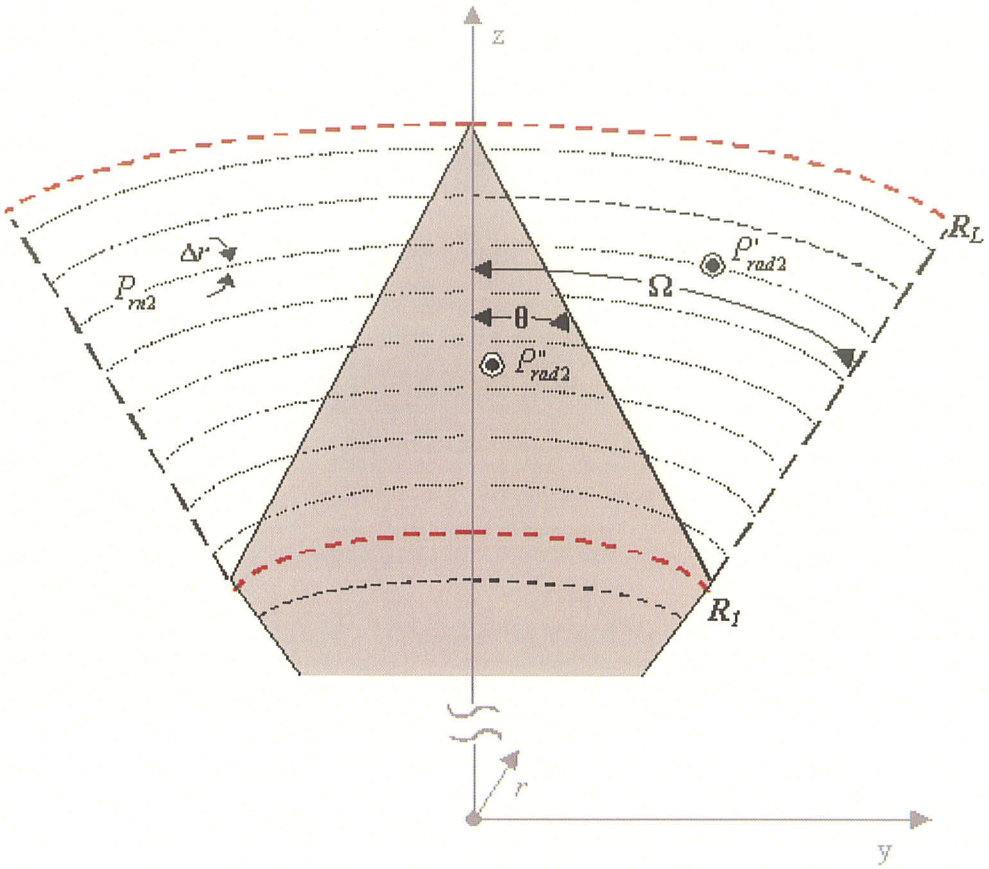

Figure B.1: Holographic Antenna Conducting Strips

For a full arc, where Ω represents the subtended angle, the power radiated, P'_{rad2}, is proportional to the incident power, where K_o is the proportionality constant,

$$P'_{rad2} = K_o \int_0^{2\pi} \int_0^{\Omega} |f(\phi, \theta)|^2 \sin\theta d\theta d\phi \tag{B.1}$$

Similarly, the power radiated from a portion of the arc, subtended by θ, P''_{rad2}, is proportional to the incident power,

$$P''_{rad2} = K_o \int_0^{2\pi} \int_0^{\theta} |f(\phi, \theta)|^2 \sin\theta d\theta d\phi \tag{B.2}$$

The ratio of these two powers is,

$$\frac{P''_{rad2}}{P'_{rad2}} = \frac{\int_0^{2\pi} \int_0^{\theta} |f(\phi, \theta)|^2 \sin\theta d\theta d\phi}{\int_0^{2\pi} \int_0^{\Omega} |f(\phi, \theta)|^2 \sin\theta d\theta d\phi} \tag{B.3}$$

or,

$$P''_{rad2} = P'_{rad2} \frac{\int_0^{2\pi} \int_0^{\theta} |f(\phi, \theta)|^2 \sin\theta d\theta d\phi}{\int_0^{2\pi} \int_0^{\Omega} |f(\phi, \theta)|^2 \sin\theta d\theta d\phi} \tag{B.4}$$

The power radiated from one of the full arcs can alternatively be expressed as the difference in power levels before and after encountering the strip, Δr, as shown in equation (B.5).

$$P'_{rad2} = P_r - P_{r+\Delta r} \tag{B.5}$$

The power radiated from each strip, 1, 2, . . . n, can be written,

$$P'_{rad2_1} = P_{r1}\left(1 - \frac{P_{r+\Delta r}}{P_{r1}}\right) \tag{B.6}$$

$$P'_{rad2_2} = P_{r2}\left(1 - \frac{P_{r+2\Delta r}}{P_{r2}}\right) \quad \ldots \tag{B.7}$$

$$P'_{rad2_n} = P_{rn}\left(1 - \frac{P_{r+n\Delta r}}{P_{rn}}\right) \tag{B.8}$$

where P_{rn} is the incident power at $rn = r + (n-1)\Delta r$,

$$P_{rn} = e^{-2\alpha(r+(n-1)\Delta r)} \int_0^{2\pi} \int_0^{\Omega} |f(\phi, \theta)|^2 \sin\theta \, d\theta \, d\phi \tag{B.9}$$

Substituting this into equation (B.8) gives,

$$P'_{rad2n} = e^{-2\alpha(r+(n-1)\Delta r)}(1-e^{-2\alpha\Delta r})\int_0^{2\pi}\int_0^{\Omega}|f(\phi,\theta)|^2\sin\theta\, d\theta\, d\phi \qquad \text{(B.10)}$$

Substituting equation (B.10) into equation (B.4), P''_{rad} can be written as,

$$P''_{rad2n} = e^{-2\alpha rn}(1-e^{-2\alpha\Delta r})\int_0^{2\pi}\int_0^{\theta}|f(\phi,\theta)|^2\sin\theta\, d\theta\, d\phi \qquad \text{(B.11)}$$

The total radiation, P_{rad2}, is found from the sum of the radiation from the individual strips,

$$P_{rad2} = \sum_{n=1}^{N} P''_{rad2n} \qquad \text{(B.12)}$$

$$P_{rad2} = \sum_{n=1}^{N} P''_{rad2n} = e^{-2\alpha r_1}(1-e^{-2\alpha\Delta r})\left(\int_0^{2\pi}\int_0^{\theta(r+\Delta r)}|f(\phi,\theta)|^2\sin\theta\, d\theta\, d\phi \ldots\right.$$

$$\left. e^{-2\alpha\Delta r}\int_0^{2\pi}\int_0^{\theta(r+2\Delta r)}|f(\phi,\theta)|^2\sin\theta\, d\theta\, d\phi + \ldots + e^{-2\alpha N\Delta r}\int_0^{2\pi}\int_0^{\theta(r+N\Delta r)}|f(\phi,\theta)|^2\sin\theta\, d\theta\, d\phi\right)$$

(B.13)

For a fixed spacing $(R_L - R_1)$ in the limit as $\Delta r \to 0$, $N \to \infty$ and the summation becomes an integration,

$$P_{rad2} = 2\alpha e^{-2\alpha R_1} \int_{R_1}^{R_L} \int_{0}^{2\pi\theta(r)} \int_{0}^{} e^{-2\alpha(r-R_1)} |f(\phi,\theta)|^2 \sin\theta d\theta d\phi dr \qquad \text{(B.14)}$$

This equation is now multiplied by $\frac{\int_0^{2\pi\Omega}\int_0^{}|f(\phi,\theta)|^2\sin\theta d\theta d\phi}{\int_0^{2\pi\Omega}\int_0^{}|f(\phi,\theta)|^2\sin\theta d\theta d\phi}$, therefore,

$$P_{rad2} = 2\alpha e^{-2\alpha R_1} \int_0^{2\pi\Omega}\int_0^{}|f(\phi,\theta)|^2\sin\theta d\theta d\phi \frac{\int_{R_1}^{R_L}\int_0^{2\pi\theta(r)}\int_0^{} e^{-2\alpha(r-R_1)}|f(\phi,\theta)|^2\sin\theta d\theta d\phi dr}{\int_0^{2\pi\Omega}\int_0^{}|f(\phi,\theta)|^2\sin\theta d\theta d\phi}$$

(B.15)

Knowing that $P_{out1} = e^{-2\alpha R_1}\int_0^{2\pi\Omega}\int_0^{}|f(\phi,\theta)|^2\sin\theta d\theta d\phi$, equation (B.15) is divided by $P_{intercepted}$, and $\frac{P_{out1}}{P_{intercepted}}$ may be replaced by $e^{-2\alpha(R_1-R_o)}$. For a circular symmetric case, the ratio $\frac{P_{rad2}}{P_{intercepted}}$ can be reduced to equation (B.16).

$$\frac{P_{rad2}}{P_{intercepted}} = e^{-2\alpha(R_1 - R_o)_1} \frac{\int_{R_1}^{R_L} \int_{0}^{\theta(r)} e^{-2\alpha(r-R_1)} |f(\theta)|^2 d2\alpha r}{\int_{0}^{\Omega} |f(\theta)|^2 \sin\theta d\theta} \qquad \text{(B.16)}$$

REFERENCES

[1] J. Goodman, "An Introduction to the Principles and Applications of Holography", *Proceedings of the IEEE*, **59**, 1292-1301 (1971).

[2] H. Arthur Klein, *Holography*. New York, NY: J. B. Lippincott Company, 1970.

[3] P.F. Checcacci, V. Russo, and A.M. Scheggi, "Holographic Antennas", *IEEE Transactions of Antennas and Propagation*, November, 811 - 813 (1979).

[4] P. F. Checcacci, G. Papi, and V. Russo, "A Holographic VHF Antenna", *IEEE Transactions on Antennas and Propagation*, March, 278 - 279 (1971).

[5] Keigo Iizuka, Motoo Mizusawa, Shuji Urasaki, and Hiroshi Ushigome, "Volume-Type Holographic Antenna", *IEEE Transactions on Antennas and Propagation*, November, 807 - 810 (1973).

[6] K. Levis, "Ka-band Holographic Antennas", M. Sc. Thesis, University of Ottawa (1999).

[7] B. E. A. Saleh and M. C. Teich, Chapter 4 in *Fundamentals of Photonics*. New York, NY: John Wiley & Sons. Inc., 1991.

[8] Winston, E. Kock, "Microwave Holography", *Microwaves*, November, 46 - 54 (1968).

[9] David J. Rochblatt and Boris L. Seidel, "Microwave Antenna Holography", *IEEE Transactions on Microwave Theory and Techniques*, **40**, 1294-1300 (1992).

[10] Taavi Hirvonen, Juha P. S. Ala-Laurinaho, and Jussi Tuovinen, "A Compact Antenna Test Range Based on a Hologram", *IEEE Transactions of Antennas and Propagation*, **45**, 1270 - 1276 (1997).

[11] Matlab, The Mathworks, http://www.mathworks.com, 2002.

[12] Constantine A. Balanis, *Antenna Theory*, New York, NY: John Wiley & Sons Inc., 1997.

[13] A. Ittipiboon, D. Roscoe, and M. Cuhaci, "A General Radiation Field Computation of Dielectric Resonator Antennas", in *IEEE Antennas and Propagation Society International Symposium,* 760 - 763, Seattle, Washington, 1994.

[14] P.J. Gibson, "The Vivaldi Aerial", in *Proceedings of the European Microwave Conference,* 101 - 104, Brighton, U.K., 1979.

[15] K. Sigfrid Yngvesson, Daniel H. Schaubert, Thomas L. Korzeniowski, Erik L. Kollberg, Thomas Thungren, and Joakim F. Johansson, "Endfire Tapered Slot Antenna on Dielectric Substrates", *IEEE Transaction on Antennas and Propagation*, December, 1392-1400 (1985).

[16] Young-Sik Kim, and K. Sigfrid Yngvesson, "Characterization of Tapered Slot Antenna Feeds and Feed Arrays", *IEEE Transactions of Antennas and Propagation*, **38**, 1559 - 1564 (1990).

[17] K. Sigfrid Yngvesson, T.L. Korzeniowski, Young-Sik Kim, and Erik L. Kollberg, "The Tapered Slot Antenna - A New Integrated Millimeter-Wave Applications", *IEEE Transactions on Microwave Theory and Techniques*, **37**, 365-374 (1989).

[18] Robert E. Collin, and Francis J. Zucker, Chapter 19 in *Antenna Theory*. New York, NY: McGraw-Hill Book Company, 1969.

[19] Rainee N. Simons, and Richard Q. Lee, "Linearly Tapered Slot Antenna Radiation Characteristics at Millimeter-Wave Frequencies", *Communication Technology*, 4-5: http://gltrs.grc.nasa.gov/reports/1998/TM-1998-207413.pdf

[20] Ehud Gazit, "Improved Design of the Vivaldi Antenna", *IEE Proceedings*, **135**, 89 - 92 (1988).

[21] Kai Fong Lee, and Wei Chen, *Advances in Microstrip and Printed Antennas.* New York, NY: John Wiley and Sons Ltd., 1997.

[22] I. Linardou, C. Migliaccio, J.M. Laheurte and A. Papiernik, "Twin Vivaldi antenna Fed by Coplanar Waveguide", *Electronics Letters*, **33,** 1835 - 1837 (1997).

[23] Pranay R. Acharya, Hans Ekstrom, Steven S. Gearhart, Stellan Jacobsson, Joakim F. Johansson, Erik L. Kollberg, and Gabriel M. Rebeiz, "Tapered Slotline Antennas at 802GHz", *IEEE Transactions of Microwave Theory and Techniques,* **41**, 1715 - 1719 (1993).

[24] Ramakrishna Janaswamy, D. H. Schaubert, and David M. Pozar, "Analysis of the Tranverse Electromagnetic Mode Linearly Tapered Slot Antenna", *Radio Science*, **21**, 797 - 804 (1986).

[25] Thomas J. Ellis and Gabriel M. Rebeiz, "MM-Wave Tapered Slot Antennas on Micromachined Photonic Bandgap Dielectrics", *IEEE MTT - S Digest*, June, 1157 - 1160 (1996).

[26] Jeremy B. Muldavin and Gabriel M Rebeiz, "MM-Wave Tapered Slot Antennas on Low Permittivity Substrates", *IEEE Transactions of Antenna and Propagation*, **47**, 1279 - 1280 (1999).

[27] K.C. Gupta, Ramesh Garg, and I,J. Bahl, *Microstrip Lines and Slotlines*, Boston, MA: Artech, 1979.

[28] Seymour B. Cohn, "Slot Line on a Dielectric Substrate", *IEEE Transaction on Microwave Theory and Techniques*, **47**, 768-778 (1969).

[29] Youn H. Choung, and William C. Wong, "Microwave and Millimeter-Wave Slotline Transition Design", *Microwave Journal*, March, 77 - 89 (1994).

[30] Linecalc, Agilent Technologies, http://eesof.tm.agilent.com/docs/adsdoc2002/linecalc/index.html, 2002.

[31] Mathematica, Wolfram Research, http://www.wolfram.com, 2002.

[32] High Frequency Electromagnetic Simulator, Ansoft Corporation. www.ansoft.com, 2002.

[33] Samuel Silver, ed. Chapter 6 in *Microwave Antenna Theory and Design*. New York, NY: Dover Publications, Inc., 1965.

[34] Roger F. Harrington, *Time-Harmonic Electromagnetic Fields*. New York, NY: McGraw-Hill Book Company, 1961.

[35] Demetrius T. Paris and F. Kenneth Hurd, *Basic Electromagnetic Theory,* New York, NY: McGraw-Hill Book Company, 1969.

[36] S. Thirakoune, A. Petosa, A. Ittipiboon, and K. Levis, "Broadband Printed Dipole Antennas", in *IEEE Antennas and Propagation Society International Symposium,* 52-55, San Antonio, Texas, 2002.